

Computational Studies of Low Dimensional Functional Materials

by

KANIKA GUPTA

A thesis submitted to
The University of Birmingham
for the degree of
DOCTOR OF PHILOSOPHY

School of Chemistry
College of Engineering and Physical Sciences
University of Birmingham
November 2020

**UNIVERSITY OF
BIRMINGHAM**

University of Birmingham Research Archive

e-theses repository

This unpublished thesis/dissertation is copyright of the author and/or third parties. The intellectual property rights of the author or third parties in respect of this work are as defined by The Copyright Designs and Patents Act 1988 or as modified by any successor legislation.

Any use made of information contained in this thesis/dissertation must be in accordance with that legislation and must be properly acknowledged. Further distribution or reproduction in any format is prohibited without the permission of the copyright holder.

Table of Contents

Abstract	6
Declaration	7
Copyright Statement	8
Dedication	9
Acknowledgement	10
Chapter 1: Introduction	12
1.1 General Background.....	13
1.2 Schafarzikite- FeSb ₂ O ₄	16
1.2.1 Lone pair interaction in Schafarzikite	18
1.2.2 The MX ₂ O ₄ Family	19
1.2.2.1 Mixed X site structures	20
1.2.2.2 Mixed M site structure.....	21
1.2.3 Oxygen and Fluorine insertion.....	22
1.2.4 Magnetic properties.....	27
1.2.5 Computational literature	29
1.2.6 Project Aim	30
1.3 Ca ₅ Ir ₃ O ₁₂	31
1.3.1 Structural and Chemical considerations	32
1.3.2 Electronic and Magnetic Properties	34
1.3.4 Project Aim	35

Chapter 2: Computation Simulation Methodology.....	36
2.1 Introduction	37
2.2 Potential Model.....	38
2.2.1 Long range interactions	39
2.2.2 Short Range Interactions.....	39
2.2.3 Polarizability	41
2.3 Perfect lattice simulation.....	42
2.3.1 Energy Minimisation.....	42
2.3.2 Physical Properties	44
Elastic Constants	45
Dielectric Constants	45
2.4 Defect Calculations	46
2.5 Mean Field and Supercell Approach.....	48
Chapter 3: Derivation of Pair Potentials	49
3.1 Introduction	50
3.2 Basic Fitting Methodology	50
3.3 FeSb ₂ O ₄ Potentials	51
3.3.1 Modelling the Lone Pair of Electrons	51
3.3.2 Sb ₂ O ₃ potentials	55
3.3.2 Anion-Anion potentials	61
3.3.3 Cation-Anion, Cation-Cation potentials	64

3.3.4 Potential Validation.....	68
3.4 Ca ₅ Ir ₃ O ₁₂ Potentials.....	72
3.5 Summary.....	77
3.6 Future Work.....	78
Chapter 4: Defect Chemistry, Dopant Substitution and Anion insertion in FeSb ₂ O ₄	79
4.1 Introduction	80
4.2 Intrinsic Defects	83
4.2.1 Schottky and Frenkel Defects	85
4.3 Dopant Substitution.....	88
4.4 Oxygen insertion.....	93
4.4.1 Initialising the defect cluster computationally	95
4.4.2 Results and analysis.....	96
4.4.1 Discussion	102
4.5 Fluorine Insertion.....	104
4.5.1 Initialising the fluorine excess phase FeSb ₂ O ₄ F _x computationally	104
4.5.2 Results and Analysis	108
4.5.3 Discussion	113
4.6 Summary.....	115
4.7 Future Work.....	116
Chapter 5: Defect Chemistry and Sodium Substitution on Ca ₅ Ir ₃ O ₁₂	117
5.1 Introduction	118

5.2 Intrinsic Defects	120
5.3 Sodium Substitution	125
5.3.1 Simulating sodium insertion in $\text{Ca}_5\text{Ir}_3\text{O}_{12}$ to form $\text{Ca}_4\text{Na}\text{Ir}_3\text{O}_{12}$	125
5.3.2 Simulating the Na excess phase: $\text{Ca}_3\text{Na}_2\text{Ir}_3\text{O}_{12}$	130
5.4 Summary.....	135
5.5 Future Work.....	136
Chapter 6: Conclusion.....	137
6.1 General Remarks.....	138
6.2 Derivation of interatomic potentials	138
6.3 FeSb_2O_4	139
6.4 $\text{Ca}_5\text{Ir}_3\text{O}_{12}$	140
Reference.....	142

Abstract

This thesis describes the application of advanced atomistic simulation techniques to study the defect properties, dopant substitution and ion insertion reactions in two novel materials FeSb_2O_4 and $\text{Ca}_5\text{Ir}_3\text{O}_{12}$. New pair potentials were empirically derived to fit both the parent phases and a series of related phases. The crystal structures predicted using these potentials were in good agreement with the observed values. These potentials were then used to investigate the defect behaviour (both intrinsic and extrinsic) in FeSb_2O_4 and $\text{Ca}_5\text{Ir}_3\text{O}_{12}$. For FeSb_2O_4 , the calculations predict that the preferred mode of intrinsic disorder in the system would be through the creation of oxygen Frenkel defects. The dopant substitution calculations predict that among the species that were examined, the most favourable dopant species at Fe site is Mg^{2+} and at Sb site is, Pb^{2+} . The preferred charge compensation mechanism for this substitution was predicted to be through the oxidation of Fe^{2+} to Fe^{3+} in the chains of linked octahedra. For oxygen and fluorine insertion, the calculations predict that the oxygen insertion reactions are energetically more favourable. In the case of oxygen insertion reaction, the simulations predict that the interstitial oxygen ions occupy sites in the one-dimensional channels bonding to Sb ions in the channel walls. The extra oxygen intake is balanced by the oxidation of Fe^{2+} to Fe^{3+} in the chains of octahedra and Sb^{3+} to Sb^{5+} in the channel walls. The calculations predict the formation of a defect cluster comprising of three 4-coordinate Sb^{3+} ions, two O^{2-} interstitials and one 6-coordinate Sb^{5+} ion. Similarly, for fluorine insertion, the calculations predict that the interstitial ions occupy the central position in the channels and are bonded to two 4-coordinate Sb^{3+} ions in the channel walls. For $\text{Ca}_5\text{Ir}_3\text{O}_{12}$, the defect calculations suggest that the preferred mode of the intrinsic disorder will be through the creation of calcium Frenkel defects. The energetics of Na insertion in $\text{Ca}_5\text{Ir}_3\text{O}_{12}$ that the Na goes to Ca site 1 to form $\text{Ca}_4\text{Na}\text{Ir}_3\text{O}_{12}$ and goes to Ca2 site in $\text{Ca}_3\text{Na}_2\text{Ir}_3\text{O}_{12}$.

Declaration

No portion of the work referred to in this thesis has been submitted in support of an application for another degree or qualification of this or any other university or other institutes of learning.

Copyright Statement

The author of this thesis (including any appendices and/or schedules to this thesis) owns certain copyright or related rights in it (the “Copyright”) and he has given the University of Birmingham certain rights to use such Copyright, including for administrative purposes.

Copies of this thesis, either in full or in extracts and whether in hard or electronic copy, maybe made only in accordance with the Copyright, Designs and Patents Act 1988 (as amended) and regulations issued under it or, where appropriate, in accordance with licensing agreements which the University has from time to time. This page must form part of any such copies.

The ownership of certain copyright, patents, designs, trademarks and other intellectual property (the “Intellectual Property”) and any reproductions of copyright works in the thesis, for example graphs and tables (“Reproductions”), which may be described in the thesis, may not be owned by the author and may be owned by third parties. Such Intellectual Property and Reproductions cannot and must not be made available for use without prior written permission of the owner(s) of the relevant Intellectual Property and/or Reproductions. Further information on the conditions under which disclosure, publication and commercialisation of this thesis, the Copyright and any Intellectual Property and/or Reproductions described in it may take place is available in the University IP Policy, in any relevant Thesis restriction declarations deposited in the University Library, the University Library’s regulations and in the University Policy on Presentation of Theses.

Dedication

I dedicate this thesis to my Gurus and my whole family for their invaluable support throughout this research.

Acknowledgement

I am grateful to God Almighty and my Preceptors- Anandmayi Maa, Sri Guru Babaji, Sri Ramakrishna Paramhamsa Thakur, Sri Ramchandra Swami, Neem Karoli Baba, Sri Maheshwarnath Babaji and Sri M for giving me the ability, courage, and strength to complete this research.

I would like to express my heartfelt gratitude to my supervisors Dr Mark Read and Professor Colin Greaves for their valuable guidance and unstinting support throughout this research. The constructive, encouraging and yet critical nature of the guidance they provided helped me immensely to face the challenges of this remarkable academic journey. They constantly encouraged me to expand the confines of my thinking and helped me to further explore and discover my abilities as a researcher. I feel very privileged and blessed to have been guided by them. I thank them both from the bottom of my heart for their valuable contributions, advice and patience.

I am grateful to EPSRC and the School of Chemistry for their financial support without which I would not have been able to carry out this research at the University.

I am grateful to Professor Martin Freer for his wonderful references that helped me secure this research opportunity.

A heartfelt and special thanks to Caroline Fox, the postgraduate administrator at the School of Physics and Astronomy, for her kindness and her tireless efforts in helping me.

Professor Rustam Stolkin has been kind enough to guide me through my postgraduate studies here.

I am very grateful to Professor Richard Batley from IDD, who has been a really good and kind friend through my trying times during the PhD.

I thank Professor Peter Slater, Dr Joseph Hriljac, Dr Sarah Horswell and Dr John Wilkie for their unstinting support.

I am grateful to Yogesh Sovanie for helping me selflessly with the python coding.

I genuinely thank my good friend Nathan Palmer, Rebecca Bird, Ivan Trussov, John Hay and all friends from Floor Five and Floor Two and the Read Group. I would not have been able to complete this research without their support.

I offer the deepest gratitude to my parents, Mr Pramod Kumar Gupta and Mrs Preeti Gupta, my grandparents, Late Mr Radhaballabh Gupta and Mrs Susheela Gupta, Mr Nirmal Daruka and Mrs Uma Daruka, my brothers, Shantanu and Uttkarsh Gupta and my dearest friends, Sabarinath, Sunil, Karabi, Ati, Renuka, Mudita, Harsha, Emma, Jennifer, Arho, Anmol, Kamal and Shalu, who stood by me through all the smooth and rough times and have been a constant source of strength and gave me much needed moral and emotional support.

Chapter 1: Introduction

1.1 General Background

Functional materials are those materials that have inherent unique features or physical properties which allow them to perform specific useful functions. For example, thermal properties, optical properties, electrical and magnetic properties. Functional materials form the basis of most modern technological advancements ranging from computing, communication, storage and display in the Information and Technology (IT) sector to clean production and storage in the energy sector. These materials encompass all material types such as organic, inorganic, hybrid materials, nanomaterials and interfaces. Among these, the mixed metal oxides form a large part of functional materials and have been used for important applications such as anode, cathode and catalyst materials from lithium-ion batteries and fuel cells.

Much ongoing research in this area is concerned primarily with enhancing the existing properties of these materials and in developing new functional materials using known mineral structures as a template. Perovskite (general formula ABO_3 , the structure is given in *figure 1.1 a*) is a prime example of one such mineral. It is one of the most extensively researched structure types which has been used to develop a range of technologically useful functional material e.g. BaTiO_3^1 which displays ferroelectric behaviour, $\text{La}_x\text{Sr}_{1-x}\text{MnO}_3^2$ which displays colossal magnetoresistance (CMR) behaviour and $\text{YBa}_2\text{Cu}_3\text{O}_7^3$ which is a structurally related high-temperature superconductor. The interesting electrical and magnetic properties of perovskites are primarily due to their structure, which consists of corner-linked octahedra made of metal cations (MO_6) and a second 12-coordinate cation with a larger ionic radius situated between the octahedra. This unique framework allows the introduction and control of mixed oxidation states of the cations within the octahedra. Spinel (MgAl_2O_4 , or general formula AB_2X_4) is another structure type that had served as a starting point for developing new functional materials such as LiMn_2O_4 which acts as an alternative cathode material for Li-ion batteries.⁴ Rutile (TiO_2 , the structure is given in *figure 1.1 b*) is another structure type, which

has an interesting framework consisting of edge-shared chains of MO_6 octahedra, along the c-axis, which are joined together by corner linking. A number of materials with this structure type demonstrate interesting properties such as VO_2 ⁵ exhibits metal-insulator transitions, MgF_2 ⁶ displays transparent optical properties and SnO_2 ⁷, shows catalytic properties used in gas sensing.

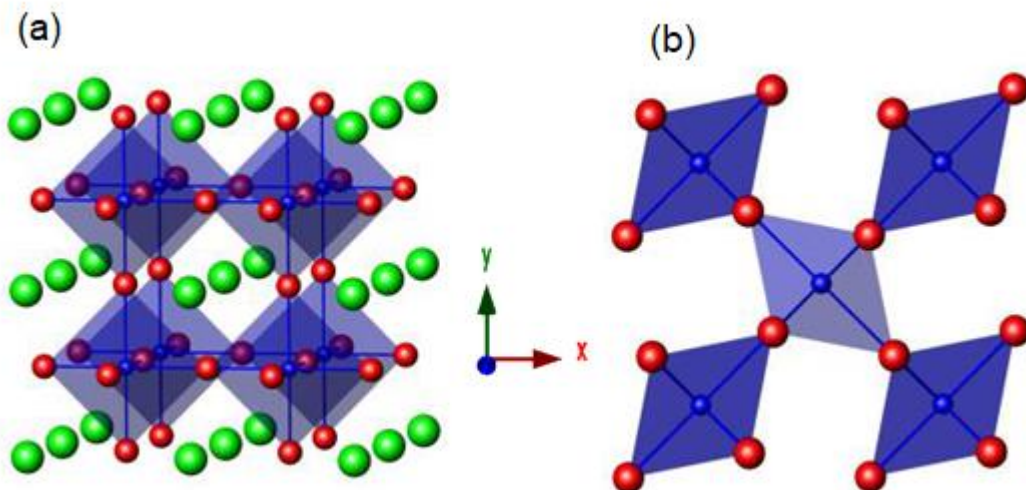


Figure 1.0.1 (a) Crystal structure of a Perovskite mineral along xy-plane; (b) Crystal structure of a rutile mineral along the xy-plane

Therefore, it has become increasingly clear that significant and important research in solid-state inorganic chemistry has focused on the development of novel functional materials from known mineral structure or the improvement of existing materials by cation substitutions or aliovalent doping. This thesis is also concerned with two such interesting, inorganic material types derived from naturally occurring structures:

- i. FeSb_2O_4 – A naturally occurring mineral known as Schafarzikite has recently gained academic interest due to its interesting structure comprising of chains of linked octahedra, similar to those seen in rutile. However, there are now two unique cation sites that increase the functionality and empty channels that can be used for anion insertion.^{8–10}

ii. $\text{Ca}_5\text{Ir}_3\text{O}_{12}$ – A ternary metal oxide containing iridium. IrO_2 is one of the best-known catalyst material used in electrochemical oxygen evolution reaction. It also has an interesting structure of linked octahedra and two distinct cation sites to allow oxidation control of one site through aliovalent substitution on the other site.¹¹

Both the compounds have similar chains of edge-linked octahedral. They also have two crystallographically different cation sites which offer the potential for aliovalent substitution to fine-tune the electrical and magnetic properties of these materials. They also display one-dimensional behaviour due to the presence of the chains of octahedra. However, there are quite a few dissimilarities between them as well.

1. As discussed later, FeSb_2O_4 has channels occupied by the electron lone pairs on the Sb^{3+} site, which could be used as the site for anion insertion; similar sites in $\text{Ca}_5\text{Ir}_3\text{O}_{12}$ are occupied by Ca^{2+} ions and hence, the possibility of anion insertion is absent.
2. The preferred conduction mechanism in FeSb_2O_4 is through anion interstitials in the channels and electron migration in the chains of linked octahedra; conductivity in $\text{Ca}_5\text{Ir}_3\text{O}_{12}$ is electronic through either holes or electrons as it exhibits semiconducting behaviour.¹²

The principal aim of this work is to apply modern computational methods to present a detailed study of the defect chemistry of the $\text{Ca}_5\text{Ir}_3\text{O}_{12}$ and FeSb_2O_4 in a way that is complementary to the experimental investigations. For this study, atomistic simulations techniques are considered to be invaluable in providing in-depth knowledge of the mode of operations of these complex and novel materials. These techniques are best suited in terms of the scale and numerical efficiency needed to further the fundamental understanding of the synthetic strategies.

Over the past decade, computer modelling has proved to be a useful tool in calculating and probing the structure, properties and defect behaviour of complex systems. It links fundamental theory with experiments and hence, has been employed to act alongside experimental techniques to develop

a better understanding of the mode of operation of complex materials. These techniques have been successfully used to study the ion migration in anion conductors and have been adapted to describe the same in fluorites, perovskites and brownmillerite type oxide structures which also demonstrate similar conduction properties.^{13–15}

1.2 Schafarzikite- FeSb₂O₄

Schafarzikite (FeSb₂O₄) is a naturally occurring rare mineral which belongs to a family of compounds that are isostructural with Pb₃O₄ or Minium.¹⁶ It was first discovered in 1921 in the Slovak Republic by Professor Ferenc Schafarzik¹⁷. It can be found largely within antimony-rich deposits in a small number of locations around the world.^{18,19} It is a tetragonal mineral with the space group *P4₂/mbc* and the lattice parameters $a = 8.61574 \text{ \AA}$ and $c = 5.92069 \text{ \AA}$.⁹ The atomic position in the structure is summarised in *table 1.1*. FeSb₂O₄ consists of two crystallographically unique cation sites namely, Fe²⁺ and Sb³⁺, having octahedral and trigonal pyramidal geometry, respectively.

Table 0-1.1 Fractional Coordinates of Schafarzikite⁹

<i>Species</i>	<i>Oxidation State</i>	<i>Wykoff Position</i>	<i>x</i>	<i>y</i>	<i>z</i>
<i>Fe</i>	2+	4d	0	½	¼
<i>Sb</i>	3+	8h	0.1772(2)	0.1648(2)	0
<i>O1*</i>	2-	8h	0.6794(1)	0.1794(1)	¼
<i>O2**</i>	2-	8h	0.0999(2)	0.6419(2)	0

*O1 is the apical oxygen; ** O2 is the equatorial oxygen

As shown in *Figure 1.1*, the structure consists of rutile-like edge-shared chains of FeO_6 octahedra running along the *c-axis*. Every unit cell consists of two such chains, which are linked together by Sb^{3+} ions. This potentially provides a means to functionalise the material and fine-tuning the electrical and magnetic properties by allowing electronic control of the cations within the chains.

Each Sb^{3+} ion is bonded to three oxygen atoms and has an unbonded electron lone pair, assuming a trigonal pyramidal geometry, SbO_3 . Chains of trigonal pyramidal SbO_3 run parallel to the chains of FeO_6 octahedra and the lone pair of electrons are directed into the channel along the *ab*-plane in alternating direction. The Fe-Fe separation (2.96 Å) within the chains is smaller than the separation between two neighbouring Fe-Fe (6.07 Å) within the same *ab* plane, providing some one-dimensional character to Schafarzikite. All the compounds belonging to the Schafarzikite family have the general structure formula MX_2O_4 .

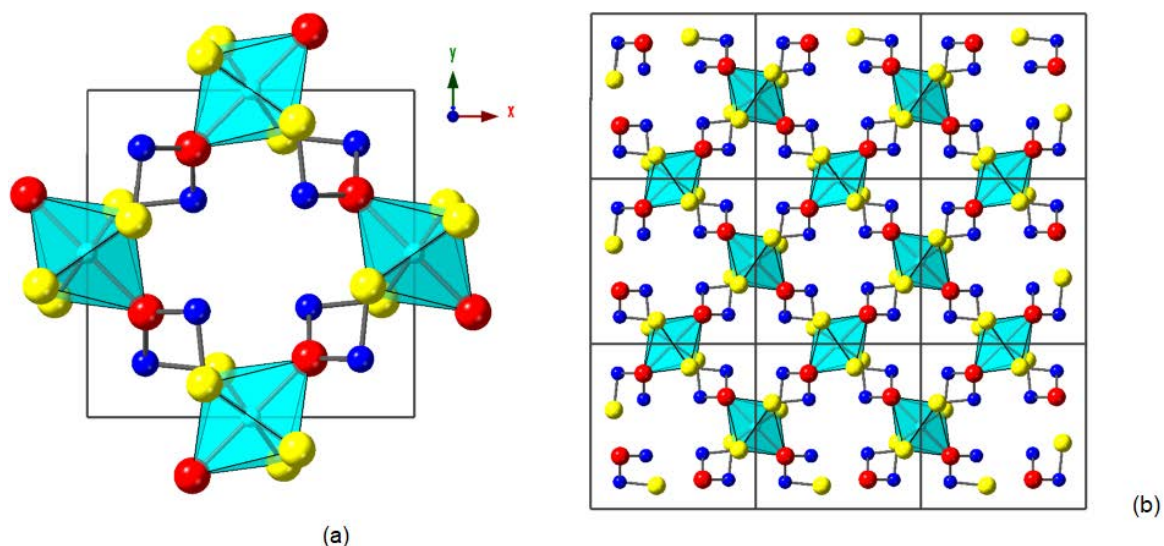


Figure 1.2 (a) A crystallographic representation of the unit cell of Schafarzikite along *xy*-plane; The blue octahedra represent the FeO_6 octahedra; the dark blue spheres represent Sb^{3+} ions, the red spheres represent the apical oxygen O1 and the yellow spheres represent the equatorial oxygen O2. The empty space in the middle is the channel. **(b)** Interconnectivity of multiple units along the *xy*-plane.

1.2.1 Lone pair interaction in Schafarzikite

As mentioned in the earlier section, the structure of Schafarzikite consists of unbonded electron lone pair pointing out into the unoccupied channel along the *xy-plane*. Due to high electron repulsion, the lone pair pushes the other ligands on the central atom Sb^{3+} , towards one side, giving rise to a distorted polyhedron equivalent to SbO_3e , where e denotes two lone pairs per formula mass. The steric effects of the electron lone are clearly visible when considering the bond angle of the O-Sb-O bonds, which are less than 109.5° ; the ideal bond angle for a tetrahedron. This indicates the strong repulsive force of the lone pair over the single bonds in accordance with Valence Shell Electron Pair Repulsion (VSEPR) theory. A schematic representation of the structure with lone pairs is given in *Figure 1.2*.

Andersson *et al.*²⁰ proposed that the volume of space occupied by a lone pair similar to that of an O^{2-} or a F^- anion whereas the lone pair-cation distance is far less than the cation-anion distance. This theory provides a route to chemically modify the system, by inserting extra oxygen or fluorine anions into the channel with an appropriate charge balance on the cations on sites M and X. This approach has been successfully adopted experimentally and will be described later in the chapter. Compounds with electron lone pairs containing cations continue to attract interest, due to the presence of an asymmetric coordination environment around the lone pair cation, which can possibly result in interesting physical properties such magnetic properties.^{21,22}

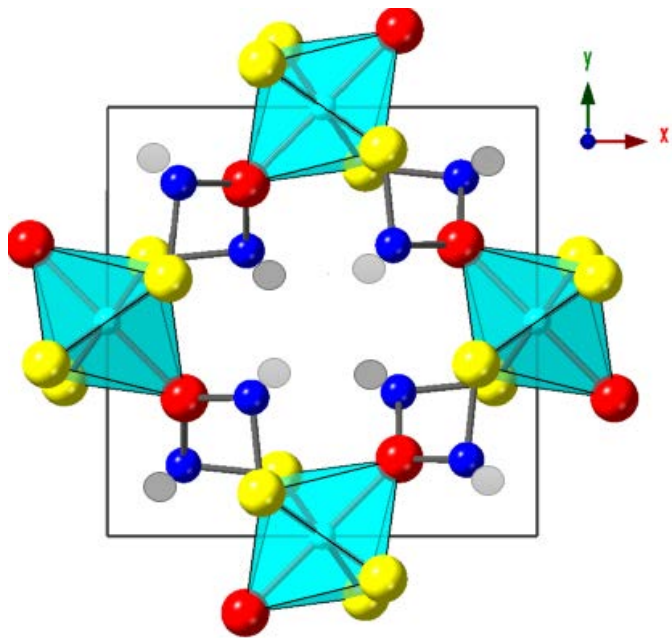


Figure 1.3 An illustration of the Schafarzikite unit cell with the lone pairs represented by the grey coloured sphere

1.2.2 The MX_2O_4 Family

Many variants of structures related to MSb_2O_4 have been synthetically created where site M is largely but not exclusively occupied by the first-row transition metals (TM) (MSb_2O_4 ; M= Mn, Ni, Co, Zn and Mg; refer to *table 1.2*). Several other systems with doping on both M and X sites have been reported. Additionally, mixed cation systems have also been reported where a single site is occupied by two cations. Among these systems, a few phases have demonstrated oxidation of site M when site X was substituted by a suitable element. In all these cases, the phases retained the original FeSb_2O_4 structure (the $P4_2/mbc$ symmetry): B = Sn^{2+} , A = Ti^{4+} ; B = As^{3+} , A = Cu^{2+} , Ni^{2+} ¹ and B = Pb^{2+} , A = Pb^{4+} , Pt^{4+} ² (*refer to Table 1.2*)

¹ No structural details were given; previous failed attempts to synthesise the arsenites have been reported⁵³
² Has $Pbam$ symmetry but contains similar structural features to Schafarzikite³³

Table 1.2 Reports of different compounds belonging to the MX_2O_4 family adopting the Schafarzikite Structure

<i>M cation</i>	<i>X cation</i>			
	<i>As</i>³⁺	<i>Sn</i>²⁺	<i>Sb</i>³⁺	<i>Pb</i>²⁺
<i>Mg</i>	-	-	23	-
<i>Ti</i>	-	24	-	-
<i>Mn</i>	-	-	25	*
<i>Fe</i>	-	-	26	-
<i>Co</i>	-	-	27	-
<i>Ni</i>	28	-	29	-
<i>Cu</i>	30	-	31	-
<i>Zn</i>	**	-	32	-
<i>Sn</i>	-	-	-	16
<i>Pt</i>	-	-	-	33***
<i>Pb</i>	-	-	-	34

* Forms a 'different 'zig-zag' low dimensional structure.³⁵

**Adopts a layered NaAsO_2 -like structure; has a high-temperature Schafarzikite structure polymorph.³⁶

*** Adopts an orthorhombic Schafarzikite-like structure, like Pb_3O_4 at low temperature.

1.2.2.1 Mixed X site structures

The availability of a chemical route to oxidise the cation within octahedra chains in Schafarzikites (MX_2O_4) has attracted considerable interest to functionalise these materials. In some materials this was achieved by creating an $\text{M}^{2+}/\text{M}^{3+}$ mixed-phase by primarily the substitution of Sb^{3+} by Pb^{2+} at site X.⁹ However, the literature on these types of systems is scarce. Initial attempts to synthesise a pure phase $\text{MSb}_{2-x}\text{Pb}_x\text{O}_4$ for $\text{M} = \text{Mn}$ by Abakumov *et al.*³⁷ was unsuccessful. The high

stability of the oxidation reaction of Mn²⁺ to Mn³⁺ resulted in selective oxidation of Sb³⁺ to Sb⁵⁺ which further substituted Mn²⁺ in the octahedral chains. The findings of a similar study performed by Whitaker *et al.*⁹ with the iron variant were in contrast with those of Mn variants. The study demonstrated the successful synthesis of a mixed-phase at site X: FeSb_{2-x}Pb_xO₄ with varying levels of Pb²⁺ up to x=0.75 which in turn resulted in the preferential oxidation of a significant amount of Fe²⁺ to Fe³⁺ ions as a charge compensation mechanism. This system was found to retain the P4₂/mbc symmetry. It was observed that with the increase in the level of lead content in the system there was an expansion in the chains of the edge linked octahedra along the *c* axis. The expansion was a response to the increased repulsion between the Fe-Fe ions within the chains, owing to the oxidation of Fe²⁺ to Fe³⁺. A similar experiment was also conducted with the cobalt variants- CoSb_{1.5}Pb_{0.5}O₄³⁸ that resulted in mixed Co²⁺/Co³⁺ cations within octahedral chains.

Another study performed by De Laune *et al.*³⁹ was successful in synthesising a new and interesting system where Sb³⁺ ion was replaced by a combination of Pb²⁺ and Bi³⁺ ions. It was the first-ever example of a phase of Schafarzikite containing purely the trivalent Fe³⁺ ions within the octahedra chains and Bi³⁺, Pb²⁺ ions forming the channel walls and the link between the octahedra. The structure of this material was related closely to the parent phase FeSb₂O₄. The unit cell had expanded along the lattice constant *a* and contracted along *c* to accommodate the difference in size and charge of Pb²⁺ and Bi³⁺ ions and the increased interionic repulsion between the Fe³⁺ within the octahedra chains. The magnetic considerations of these phases have been discussed later in this chapter.

1.2.2.2 Mixed M site structure

The literature on phases containing a mixture of transition metal ions for site M is even scarcer. The systems reported so far include Fe/Co^{38,40-42}, Mn/Co⁴¹, Mg/Ni⁴³ Fe/Mg⁴⁴ and Mn/V⁴⁵. The Mn/V system was reported in a brief by Abe *et al.*,⁴⁵ wherein a high purity phase- (Mn_{1-x}V_x) Sb₂O₄ (where x = 0-0.6) with P4₂/mbc symmetry was reported. However, the method used for calculating the lattice

parameters was unclear. These findings contrasted with those reported by Brach *et al*⁴³ where a similar system Mg_{1-x}Ni_xSb₂O₄ (where 0.01 ≤ x ≤ 0.20) was reported to have rhombic distortion.

The Fe/Co, and Mn/Co phases were synthesised in a detailed study of the structure and magnetic properties of a series of compounds containing mixed M²⁺ cations for iron and manganese variants: Fe_xCo_{1-x}Sb₂O₄ (x= 0.0, 0.25, 0.50, 0.75, 1.0) and Mn_xCo_{1-x}Sb₂O₄ (x=0.0, 0.2, 0.4, 0.5, 0.6, 0.8, 1.0). The unit cell size was seen to increase with the increase in the amount of x. However, this increase was not as rapid as in the Mn containing series. The variations observed in the unit cell size was in accordance with the difference in the atomic radii of the cations (Mn²⁺ > Fe²⁺ > Co²⁺). A small decrease along lattice constant *c* was also observed with the increase in levels of x.⁴¹

The synthesis of mixed Fe/Mg phases was recently performed in an experiment aimed at studying the structure and magnetic properties of these materials and their oxygen and fluorine rich phases.⁴⁴ The new phases with the mixed Fe/Mg composition: Fe_{1-x}Mg_xSb₂O₄ (where x= 0.25, 0.50, 0.75), were observed to retain the Schafarzikite (FeSb₂O₄) structure. The unit cell parameters were seen to decrease with the increase in the amount of Mg owing to the decrease in the ionic radius of Mg (0.72 Å)⁴⁶ as compared to Fe (0.78 Å)⁴⁶. A detailed description of the oxygen and fluorine rich phases is given in the next section.^{44,47}

1.2.3 Oxygen and Fluorine insertion

Schafarzikites have a unique structure containing one-dimensional channel with Sb³⁺ cations in the channel walls. These channels are occupied by lone pair of electrons and are separated by FeO₆ octahedra chains that run parallel to the channel walls. It has been observed that for most oxide materials that have empty channels, the walls consist of O²⁻ ions and these channels act as sites for cation insertions. This unusual structure along with the material's high compositional flexibility could be used to explore the possibility of anion insertion within the channel walls. Though the structure has

received much attention due to the magnetic and electrical properties associated with the octahedra chains, the possible chemistry that could occur within channels have largely been unexplored.

Oxygen ion insertion in a one-dimensional channel

A recent study by de Laune *et al.*^{44,47} investigated the possibility of inserting oxygen interstitials into the unique one-dimensional channels in compounds belonging to the Schafarzikite family. Several compounds with the structure of Schafarzikite were synthesized by heating them in an oxygen-rich environment at 600–750 °C for 6 hours. These oxidised products displayed an increase in their respective masses. Among these, the compounds with high Fe²⁺ content displayed the highest mass increase resulting from high oxygen intake, which resulted in broadened diffraction peaks. To overcome this difficulty the amount of the Fe²⁺ per formula unit (pfu) was controlled by substituting isovalent cations, Co²⁺ and Mg²⁺, at site M and aliovalent cations, Pb²⁺ at site X. The resulting phases and the amount of Fe²⁺ pfu corresponding to each phase is summarised in *table 1.3*.

Table 1.3 Summary of the composition used to insert excess oxygen ions⁴⁷

<i>Composition</i>	<i>Amount of Fe²⁺ pfu</i>
<i>Co_{0.75}Fe_{0.25}Sb₂O₄</i>	0.25
<i>Mg_{0.75}Fe_{0.25}Sb₂O₄</i>	0.25
<i>FeSb_{1.25}Pb_{0.75}O₄</i>	0.25 Fe ²⁺ and 0.75 Fe ³⁺
<i>Co_{0.25}Fe_{0.75}Sb_{1.75}Pb_{0.25}O₄</i>	0.50 Fe ²⁺ and 0.25 Fe ³⁺

The masses of these oxidised phases were then investigated using Thermogravimetric Analysis (TGA) to study the mass changes as a function of the rise in temperature. All samples containing Fe^{2+} ions displayed an increase in their masses around 350°C . At first, this mass increase was associated solely with the amount of Fe^{2+} ions in the sample. It was considered, that for every O^{2-} ion that gets absorbed in the system, two Fe^{2+} ions are oxidised to two Fe^{3+} ions. However, the amount of O^{2-} absorbed (upto 0.50 pfu) was observed to be twice as much as that expected (0.24 pfu) from the oxidation of 2Fe^{2+} to 2Fe^{3+} . A few hypotheses were proposed to explain this difference in mass increase: 1) the oxygen entering the channels could be in the form of peroxide ions, 2), the presence of Fe^{4+} ions and 3), the oxidation an additional cation, Sb^{3+} to Sb^{5+} . Further investigations were performed using Raman and Mossbauer Spectroscopy techniques. The results from each technique pointed towards the presence of a Sb^{5+} ion in the oxidised samples and no traces of either peroxide ions or Fe ions in a higher oxidation state, were found.⁴⁷

Neutron Powder Diffraction (NPD) data was collected on $\text{FeSb}_{2-x}\text{Pb}_x\text{O}_{4+y}$ samples to determine the atomic position of all the ions within the system, including the O^{2-} interstitials. Based on the NPD data, it was observed that interstitial O^{2-} were found at sites within the one-dimensional channels. The atomic positions of all the ions in the oxidised sample was determined using NPD technique. All the positions are summarised in *table 1.4*; the observed lattice parameters for this phase are, $a=8.4063\text{\AA}$, $c=6.0443\text{\AA}$.⁴⁷

Table 1.4 Summary of the atomic positions of $\text{FeSb}_{0.25}\text{Pb}_{0.25}\text{O}_{4+y}$ ⁴⁷

<i>Atom</i>	<i>Position</i>	<i>x</i>	<i>y</i>	<i>z</i>	<i>Occupancy</i>
Fe	<i>4d</i>	0.0	0.5	0.25	1.0
Sb/Pb	<i>8h</i>	0.1542	0.1557	0.0	0.625/0.375
O1	<i>8d</i>	0.6701	0.1701	0.0	1.0
O2	<i>8h</i>	0.0981(3)	0.6278	0.25	1.0
O3	<i>16i</i>	0.540	0.417	0.254	0.059

In table 1.4, O1 refers to oxygen ions present at the apical site, O2 refers to oxygen ions present at the equatorial site and O3 refers to the oxygen interstitial in the lattice.

Based on the average atomic positions, the average Sb-O bond distances as well as the bond valence sum (BVS) values, the formation of defect cluster comprising of two 4-coordinate Sb^{3+} ions, two O^{2-} interstitials and one 5-coordinate Sb^{5+} ion, was proposed.⁴⁷

This low-temperature oxidation mechanism is unique to this phase and it suggests the possibility of high oxide ion mobility within the channels. These partially filled oxide ion channels could provide an interstitial oxide ion migration as compared to the normal migration mechanism that occurs through vacancies. The above redox reaction coupled with a variety of cation substitutions at site M could result in a range of catalytic and electrocatalytic applications.

Fluorine ion insertion

Fluorine insertion in some low dimensional oxide materials in the past has led to changes in the structural and electronic properties resulting from the oxidation of the transition metals in the materials.^{48,49}. La₂CuO₄ is a prime example of this phenomenon where the material transitions from semiconducting behaviour to superconducting behaviour when fluorine is inserted in the structure:



Another investigation by de Laune *et al.*,⁵¹ extended the oxygen insertion study to examine the possibility of fluorine insertion reactions. Various samples of compounds Schafarzikite were fluorinated by heating them in flowing F₂ at 230 °C at varying time intervals. Phases Mg_{0.50}Fe_{0.50}Sb₂O₄ and Co_{0.50}Fe_{0.50}Sb₂O₄, were selected for determining the amount and atomic position of F⁻ ions absorbed by the system. These samples had a fixed amount of Fe²⁺ ions at site M, hence the problem associated with broadened diffraction peaks was avoided. Cations such as Co²⁺ and Mg²⁺ that were found to be stable at the temperature at which the reaction occurs were doped onto site M to avoid any further oxidisation during the fluorination process. The structure of both the fluorine excess phases was determined by X-ray Diffraction (XRD) technique. NPD data from the investigation of the oxygen-excess phases, along-with XRD data was used to locate the absorbed F⁻ ions. It was observed that the sites that occupied interstitial F⁻ ions were closely related to those occupied by O²⁻ interstitials in the oxygen-excess phases.⁴⁷ The charge compensation mechanism responsible for the uptake of extra fluorine was the oxidation of Fe²⁺ to Fe³⁺. Based on the average atomic position values and average Sb-O and Sb-F bond distances, it was proposed that the absorbed F⁻ ions occupied sites close to the centre of the channels and were bond two 4-coordinate Sb³⁺ ions in channel walls in a bridge-like manner. This structure was proposed on the assumption that there was no exchange between the oxygen and fluorine ions. Simple Madelung Energy calculations were performed to verify this assumption.⁵¹ The reported atomic positions of Mg_{0.50}Fe_{0.50}Sb₂O₄ are summarised in *Table 1.5*

Table 1.5 A summary of the atomic positions of $Mg_0Fe_{0.5}Sb_2O_4F_c$ ⁵¹

<i>Atom</i>	<i>Position</i>	<i>x</i>	<i>y</i>	<i>z</i>	<i>Occupancy</i>
<i>Fe/Co</i>	<i>4d</i>	<i>0.0</i>	<i>0.5</i>	<i>0.25</i>	<i>0.5/0.5</i>
<i>Sb</i>	<i>8h</i>	<i>0.1660</i>	<i>0.1634</i>	<i>0.0</i>	<i>1.0</i>
<i>O1</i>	<i>8d</i>	<i>0.6747</i>	<i>0.1747</i>	<i>0.0</i>	<i>1.0</i>
<i>O2</i>	<i>8h</i>	<i>0.1</i>	<i>0.6348</i>	<i>0.25</i>	<i>1.0</i>
<i>F</i>	<i>16i</i>	<i>0.560</i>	<i>0.474</i>	<i>0.265</i>	<i>0.120</i>

In both anion insertion reactions described above and the localised structure around the anion interstitials, the individual bond distances or the possibility of fluorine and oxygen ions exchange were not determined. The reason for this is that a) crystallographic data gives average values of all the bonds and atomic positions and b) O^{2-} and F^- have coherent X-ray diffraction lengths and hence experimentally, it is impossible to differentiate between the two species.

1.2.4 Magnetic properties

All the compounds with the MX_2O_4 structure show antiferromagnetic (AFM) ordering at Neel temperature for the range 40-60 K with the exception of $CuAs_2O_4$ which is ferromagnetic at low temperatures.⁵² The two principal types of antiferromagnetic order observed for MX_2O_4 compounds are A-type magnetic order and C-type magnetic order with the moments aligned parallel to [001] and perpendicular to [001] direction, respectively (refer to *figure 1.4*). $FeSb_2O_4$ is observed to display A-type order below the Neel temperature 45K resulting from a strong magnetic exchange between Fe^{2+}

ions within the octahedral chains (the small separation within the octahedra chains causes the Fe^{2+} orbitals to overlap and hence interaction).⁵³

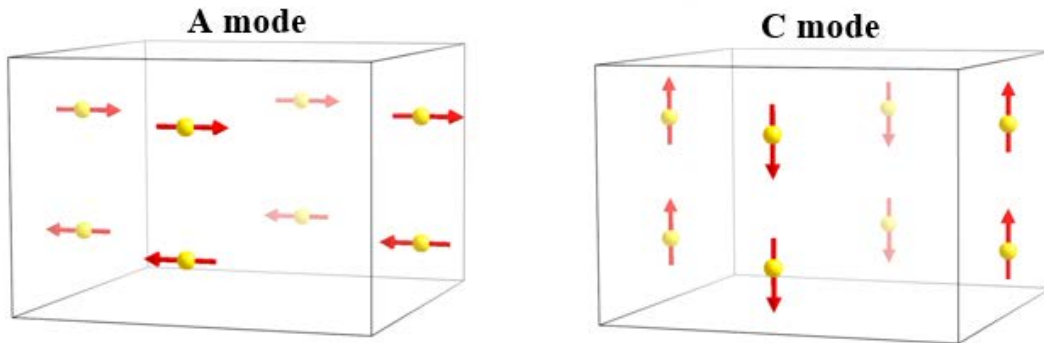


Figure 1.4 A pictorial representation of the A and C type magnetic ordering

A change in magnetic ordering is observed as moves across the first row of transition metals from Mn to Ni; compounds with M=Mn, Fe show A-type antiferromagnetic order whereas compounds with M= Co, Ni display C-type magnetic ordering. To investigate this unique magnetic behaviour, Greaves *et al.*,^{10,41} investigated magnetic properties of compounds with mixed compositions for site M, $\text{Mn}_x\text{Co}_{1-x}\text{Sb}_2\text{O}_4$ and $\text{Fe}_x\text{Co}_{1-x}\text{Sb}_2\text{O}_4$ for different doping levels of x between zero and one. Mossbauer spectroscopy revealed interesting magnetic properties wherein both the structures show canted antiferromagnetic behaviour which changes from type C to type A when x is varied from 0 to 1, respectively. An interesting shift of magnetic order from A-type to C-type was observed in $\text{FeSb}_{2-x}\text{Pb}_x\text{O}_4$ and oxygen excess $\text{M}_{0.50}\text{Fe}_{0.50}\text{Sb}_{2}\text{O}_{4+y}$ ^{44,47} due to partial oxidation of Fe^{2+} to Fe^{3+} resulting from cation substitutions at site X. Pure Fe^{3+} ion containing compound FePbBiO_4 , display A-type magnetic ordering highlighting the delicate balance that exists between the interchain-interchain magnetic exchange.³⁹

The electronic conductivity studies related to these compounds suggests semiconducting behaviour for compounds that contain Fe^{2+} ions and phases with a mixed composition of $\text{Fe}^{2+}/\text{Fe}^{3+}$ ions show the highest levels of conductivity.^{47,51}

1.2.5 Computational literature

The need for computational modelling arises when many processes taking place at the atomistic level cannot be completely understood through characterisation and crystal refinement techniques. At times it is not easy to distinguish between similar species of ions like F⁻ and O²⁻ with characterisation techniques like XRD and NPD; for instance, when fluorine ions are inserted in Schafarzikite, it is impossible to determine whether fluorine ions occupy sites within the channels or if they prefer to substitute the oxygen ions in the FeO₆ chains. As the above reaction is charge neutral and both oxygen and fluorine similar neutron scattering lengths, it is very difficult to differentiate between the two reactions. Hence, atomistic simulation can be employed to gain a fundamental understanding of the energetics of such reaction, the crystal structure, the mode of operation of defects and the properties associated with the defect behaviour for such compounds.

The main challenge in describing the structure of FeSb₂O₄ using computational techniques is the accurate simulation of the lone pairs on the Sb³⁺ ion. These lone pairs occupy what seem to be empty spaces in the crystal along the *ab*-plane and distort an otherwise regular pyramidal geometry of the Sb³⁺. Few attempts have been made to simulate the Schafarzikite-related structures computationally and all these studies involve using the *ab-initio*, Density Functional Theory (DFT) calculations.^{54 55} No investigation or study has yet been conducted to model these structures using the atomistic approach.

Gordon *et al.*,⁵⁴ investigated the effect of pressure on the magnetic properties in CuSb₂O₄ using DFT calculations. Cumby .J⁵⁵ also performed DFT calculations on a number of compounds belonging to the MX₂O₄ group to study the structural behaviour and effect of pressure on structural and magnetic behaviour. Catlow *et al.*,⁵⁶ have also used DFT calculation to study the oxidation-reduction processes taking place at the (100) surface of FeSbO₄. In the same study, the group has also presented the effect of introducing oxygen vacancies on the (100) surface wherein the oxygen vacancies result in Sb³⁺

formation such that the lone pairs on the Sb³⁺ ions point towards the vacancy sites. Other groups that have worked with compounds having similar structural complexity of the inert pair of electrons have used atomistic simulation techniques. Islam *et al.*,^{13–15} is an example of one such group which has studied the structural properties and defect behaviour of the various phases that contain the Bi³⁺ cation lone pair. The study presented a unique technique of using Cation-Cation short-range interaction similar to an oxygen-oxygen interaction (used to model all oxide materials) to accurately model the effects of the electron lone pair on the crystal structure. The study also used the shell model proposed by Dick and Overhauser⁵⁷ to describe the polarization effect of the Sb³⁺ due to the lone pair of electrons. Lebellac *et al.*,⁵⁸ is another group that investigated the electrostatic effect of electron lone pairs systems on pure systems like alpha-PbO, Pb₃O₄, SnO and system with impurities.

1.2.6 Project Aim

The aim of this study is to present atomistic techniques for the development of novel pair potential values for FeSb₂O₄ and compounds with a similar general formula (MX₂O₄). These pair potential values would describe the steric effect of electron lone pairs on FeSb₂O₄ and will be used to reproduce the crystal structure of with high level of accuracy. These parameters will also be used to predict defect chemistry and energetically favourable dopant species for insertion on M and X cation sites. The study also aims to model the insertion of anions O and F into the empty channels, which are unique to this structure and predict the most energetically favourable positions for the anions, the appropriate charge compensation mechanism and the coordination environment of the surrounding lattice ions. These techniques will act as a tool for studying the known structure and work alongside with experimental techniques. Majority of modelling will be performed using the software General Utility Lattice Program (GULP).

1.3 Ca₅Ir₃O₁₂

Iridates

Electrochemical and photochemical splitting of water to produce hydrogen gas and oxygen gas requires a highly active catalyst for the oxygen evolution reaction (OER) at the anodic surface. Catalysts for oxygen evolution reaction (OER) and oxygen reduction reaction (ORR) in both acidic and basic solutions are highly sorted after for clean energy production and storage through batteries, electrolyzers and fuel cells. The performance and application of RuO₂ and IrO₂ as most active electrocatalysts are well known.^{59,60} Currently, IrO₂ is the only known 5d transition metal oxide which exhibits an admirable OER activity and stability even in acidic conditions and hence has been used as a state-of-the-art catalyst.^{61–63}

Iridium oxide belongs to the family of transition metal dioxides with rutile like structure which consists of arrays of edge shared IrO₆ octahedra cross-linked by corner-sharing. This structure leads to the formation of vacant channels which could act as tunnels to transport intercalated ions.⁶⁴ Owing to the interesting physical properties, there has been an increase in the research on oxides of iridium or iridates: Kitaev spin liquid in A₂IrO₃, spontaneous Hall effect at zero field in Pr₂Ir₂O₇, metal-insulator transitions with all-in all-out ordering in Ln₂Ir₂O₇ and spin orbit interaction (SOI) induced Mott insulating state in Sr₂IrO₄.^{65–72} Iridates like BaIrO₃^{66–68} Sr₃Ir₂O₇⁶⁹, Ca₄IrO₆⁷³, CaIrO₃⁷⁴, etc, where IrO₂ retains its formal charge are also being investigated as many of them have exotic electronic and magnetic properties. Iridium is a rare and precious metal and therefore, a considerable amount of research has been conducted to explore the advancements in OER activity to reduce iridium consumption. The research concerns mostly with irradiates such as binary or ternary oxides of iridium, doped with other metals: Co⁷⁵, Ni⁷⁶, Cu⁷⁷, Ru⁷⁸ and Sn⁷⁹ and new structure types like hollandite⁸⁰ and pyrochlores.⁸¹

As outlined in *Section 1.1*, the presence of two cation sites in perovskites, ABO_3 , provides the ability to control the oxidation state of cation at site B , by dopant substitutions on cation site A . This unique structural property of the perovskite has been responsible for most of the functional materials that have been derived from this framework. This ability to control the oxidation state of iridium ions is absent IrO_2 as a second cation site is missing. However, the calcium containing ternary oxide of iridium, $\text{Ca}_5\text{Ir}_3\text{O}_{12}$, has two cation sites and hence shows potential for electronic control in IrO_6 chains. Moreover, unlike most iridates, the iridium ions assume a mixed oxidation state of +4.67 in $\text{Ca}_5\text{Ir}_3\text{O}_{12}$.

1.3.1 Structural and Chemical considerations

$\text{Ca}_5\text{Ir}_3\text{O}_{12}$ is a ternary oxide of iridium which has a hexagonal structure. It was initially identified as Ca_2IrO_4 .⁸² It belongs to the $P-62m$ space group and has the lattice parameters a and c equal to 9.4208 and 3.1941 \AA , respectively. There are two unique cation sites namely, Ca and Ir. The structure consists of one-dimensional (1D) IrO_6 octahedra which form triangular lattices. The presence of these infinite chains of one dimensional IrO_6 could give rise to unique electronic and magnetic properties. There is no cross linking between neighbouring octahedra chains and the inter-chain Ir-Ir distance is 5.32 \AA . The calcium atoms are arranged in between chains of IrO_6 octahedra with one calcium being 7-coordinate and the other being 9-coordinate. There are three crystallographically equivalent Ir ions: one Ir^{4+} ($5d^5$) and two Ir^{5+} ($5d^4$) ions in each formula unit and they exist in a 1:2 ratio.^{11,82} The averaged formal charge of Iridium ions is +4.67. A detailed structure is given in *Figure 1.3* and the atomic positions are given in *Table 1.6*.

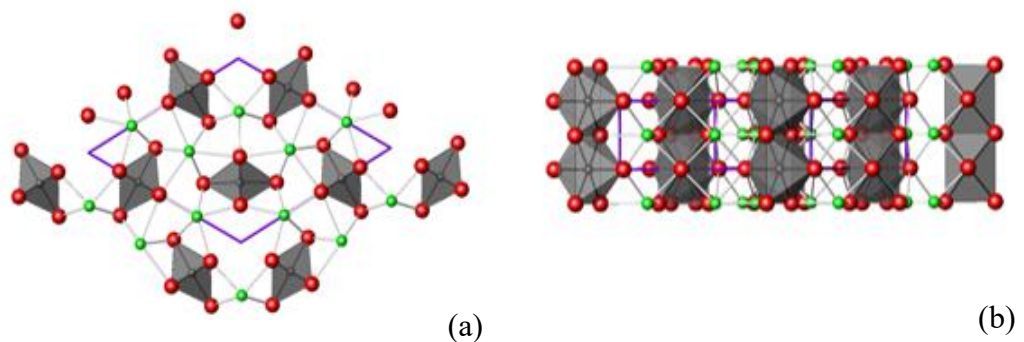


Figure 1.3 $\text{Ca}_5\text{Ir}_3\text{O}_{12}$ viewed along the (a) z-axis and (b) x-axis; The grey sphere represent the IrO_6 chains, the green spheres represent the calcium ions and the red spheres represent oxygen ions.

Table 1.6 Summary of the atomic positions of $\text{Ca}_5\text{Ir}_3\text{O}_{12}$.⁸³

<i>Atom</i>	<i>x</i>	<i>y</i>	<i>z</i>	<i>Mult</i>
<i>Ca1</i>	0.3333	0.6667	0.5	2
<i>Ca2</i>	0.7124	0.0	0.5	3
<i>Ir</i>	0.3324	0	0	3
<i>O1</i>	0.201	0	0.5	3
<i>O2</i>	0.462	0	0.5	3
<i>O3</i>	0.446	0.242	0	6

Though the structure of this compound is unique and has two distinct cation sites which could act as sites for aliovalent substitution to fine-tune the electronic and magnetic properties, studies reporting the effect of cation substitution on either of the sites are scarce. Xiang *et al.*⁸⁴ reported the production of $\text{Ca}_5\text{Ir}_3\text{O}_{12}$ in a study that investigated the effect of an isoelectronic substitution within single crystals of $(\text{Sr}_{1-x}\text{Ca}_x)_{2-y}\text{IrO}_{4+z}$ for varying levels of x . The structure evolved from the nominal

$n=1$ Ruddlesen-Popper phase (for $x=0$ to 0.11) to the quasi one-dimensional $\text{Ca}_5\text{Ir}_3\text{O}_{12}$ structure for higher concentrations of Ca ion (beyond $x=0.75$). An intermediate phase consisting of a three-dimensional network of corner shared octahedra- $\text{Sr}_3\text{CaIr}_2\text{O}_9$ was also reported. The study also reported an antiferromagnetic phase transition in $\text{Ca}_5\text{Ir}_3\text{O}_{12}$ phase when Sr ions were substituted (upto 11 %) onto the Ca site $(\text{Sr}_{1-x}\text{Ca}_x)_5\text{Ir}_3\text{O}_{12}$ (for $x=0.89$). Other calcium iridate variants with substitution onto the calcium and iridium site include $\text{Ca}_3\text{CuIrO}_6$, $\text{Ca}_{3.75}\text{Ni}_{0.25}\text{IrO}_6$.⁸⁵ and $\text{Ca}_3\text{NaIrO}_6$, $\text{Ca}_3\text{NaRuO}_6$.⁸⁶ The study by Zur Loye *et al.*⁸⁶ reported the incorporation of smaller alkali metals in perovskite-related oxides that contains a structure with alternating face share octahedra and trigonal prisms. They reported two isostructural Calcium iridate and ruthenate phase where it was possible to insert smaller cations onto the Calcium site ($\text{Na}^+ < \text{Sr}^{2+} < \text{Ba}^{2+} < \text{K}^+$); however, the insertion of the larger potassium cation lead to the formation of an incommensurate phase. There have not been any reports on the cation substitution on Iridium. The magnetic and electronic properties of this compound are summarised in the next section.

1.3.2 Electronic and Magnetic Properties

A recent study by Matsuhira *et al.*,⁸⁷ reported the display of semiconducting behaviour over a small bandgap (~ 0.2 eV) which resulted in non-linear conductivity in $\text{Ca}_5\text{Ir}_3\text{O}_{12}$ along the *c axis*. The main findings of the study reported a decrease in resistivity with a decrease in temperature. The *ab initio* calculations revealed a considerable change in the low energy electronic structure resulting from the spin-orbit interaction. The Fermi surface exhibited a sheet-like structure along the *c* axis* due to the presence of 1D chains of IrO_6 octahedra.⁸⁷

1.3.4 Project Aim

In an ongoing study, it was possible to obtain single phase materials with Na cations substituted with Ca, in $\text{Ca}_5\text{Ir}_3\text{O}_{12}$ to form $\text{Ca}_4\text{Na}\text{Ir}_3\text{O}_{12}$; the charge compensation was achieved by the oxidation of iridium ions from +4.67 to +5.00. The unit cell sizes obtained were slightly different compared with the parent phases. There are two crystallographic sites for calcium ion in the parent phase and with XRD, it is difficult to provide definitive answers in which Ca site the Na is located. Therefore, this study was undertaken to determine the energetically preferred site for Na and to determine the same for insertion of two Na ions in the parent phase to form $\text{Ca}_3\text{Na}\text{Ir}_2\text{O}_{12}$. The study also aims to investigate the defect behaviour of this material and determine the preferred modes of intrinsic defect chemistry. For this purpose, novel pair potentials were derived to fit $\text{Ca}_5\text{Ir}_3\text{O}_{12}$ and its Na doped variants. The results obtained from this study will be used if further study of electrocatalytic properties of $\text{Ca}_5\text{Ir}_3\text{O}_{12}$ and the related phases is undertaken.

Chapter 2: Computation Simulation

Methodology

2.1 Introduction

In theoretical solid-state chemistry, reproduction of the crystal structure is a crucial step to understanding and predicting the physical and chemical properties of a compound. Simple structures comprising of two to three atoms can be modelled using basic mathematical equations that enable the researcher to calculate the most energetically favourable arrangement for those atoms. However, this is not always the case and as the complexity of the structure under study increases, the need for a more powerful tool also increases. This problem can be overcome by the use of atomistic or computer simulation methods that enables the researchers to model diverse and complex systems with ease and efficiency.

Atomistic simulation techniques now enjoy being a popular choice for the modelling of complex structures as well as dynamic processes in solid-state chemistry. In the past, these techniques have served as powerful tools to validate and bolster experimental data. With the advancement in the area of computing, these methods can not only predict but also guide experiments to get the desired results.⁸⁸ It is possible to model pure crystal structures, amorphous structures, defects and their behaviour in solids and lattice vibrations and other dynamic processes. All the static lattice simulations in this project were performed using the General Utility Lattice Program (GULP). GULP, developed in the early 90s is a sophisticated code, which has a collection of algorithms that are useful for simulating inorganic as well as organic structures with high precision. The energy minimization calculations are based on the structure's inherent symmetry, which enables GULP to be more efficient by maximizing the use of space group of symmetry as compared to other existing codes.⁸⁸

2.2 Potential Model

All the atomistic simulation techniques rely on a potential model for the reproduction of the crystal structure with accuracy. A potential model is a mathematical description of the lattice energy of a crystal structure. This lattice energy (E_L) is the energy required to bring together ions from infinite separation to an equilibrium position within a crystal structure. For the computational calculation of E_L , it is assumed that the system consists of an infinite array of point charges and the energy of the system is a summation of all the interactions between ions present within the unit cell and their replication to infinity by symmetry. The mathematical representation of E_L is given in *equation 2.1*.

$$E_L = \sum_{i=1}^N E_i + \frac{1}{2} \sum_{i=1}^N \sum_{j=1}^N E_{ij} + \frac{1}{6} \sum_{i=1}^N \sum_{j=1}^N \sum_{k=1}^N E_{ijk} \dots \dots \quad (2.1)$$

The relative energies or energies from various atomic interactions are of primary use and concern. Hence, the first term E_i , representing the self-energy (which is constant) in *equation 2.1* is ignored. The remaining terms result from the interaction between the central i ion and its neighbouring ions j, k . All compounds simulated in this study are ionic and thus, the pairwise interaction is dominant, resulting in the truncation of *equation 2.1* to include only the E_{ij} term.⁸⁹ This energy is partitioned into the energy due to long and short-range interactions.⁹⁰

$$E_L = E_{LR} + E_{SR} \quad (2.2)$$

$$E_L = \sum_{ij} \frac{q_i q_j}{r_{ij}} + \sum_{ij} \Phi_{ij}(r_{ij}) \quad (2.3)$$

The first term E_{LR} in *equation 2.2* represents the long-range interactions resulting in Coulombic energy between ions i and j separated by distance r . The second term (the two-body term) E_{SR} represents the short-range energy resulting from electronic repulsion and Van der Waal's attraction between the ions in close proximity. The total lattice energy E_L represented by *Equation 2.3*, is a sum all the long and short-range interactions between the pairs of ions i and j .

2.2.1 Long range interactions

Long-range interactions are electrostatic in nature and account for almost 80% of the total lattice energy in most ionic compounds. The Coulomb's law for electrostatic interaction, given by *equation 2.4*, wherein, q_i and q_j are the formal charges of the atoms or ions defines these interactions, r_{ij} is the distance between ions and ϵ_0 is the permittivity of free space. Due to its inverse dependence on the interatomic distance, this potential is slow converging. Hence, it is computationally quite expensive, as one would have to model a large number of interactions even at large distances.

$$E_{LR}(r_{ij}) = \frac{1}{4\pi\epsilon_0} \left(\frac{q_i q_j}{r_{ij}} \right) \quad (2.4)$$

Ewald Summation is used to overcome this problem, wherein the Laplace transform of the interatomic distance is calculated and then it is split into two rapidly convergent series namely, the real space and the reciprocal space.⁹¹

2.2.2 Short Range Interactions

The short-range potentials or interactions describe the nonbonded interactions at short distances (1-2 Å). These interactions include electron cloud overlap, Pauli's repulsion and Van der Waals's attraction. Depending on the number of ions interacting within a given system, a suitable potential form can be employed to model the short-range potential energy. For most ionic systems, these interactions are limited to two-body interactions only; three-body interaction or multiple body interactions are used to describe the interactions that are covalent in nature or have an angular dependence. Potential forms such as the Morse potential⁹², the Lennard-Jones potential⁹³, the Buckingham⁹⁴ and Born-Mayer potential⁹⁵ are employed to model the forces acting between ion pairs. Among these, the Buckingham and Born-Mayer potentials are the most commonly used potential forms as they have an exponential term to describe Pauli's repulsion due to the electron cloud overlap and an

attractive term with an inverse r^6 dependence which describes the attraction between induced dipoles of charged electron cloud at small separations. (equation 2.5)⁹⁰

$$E_{SR}(r_{ij}) = A_{ij} \exp\left(\frac{-r_{ij}}{\rho_{ij}}\right) - \left(\frac{C_{ij}}{r_{ij}^6}\right) \quad (2.5)$$

Here A , ρ and C constant potential parameters for each ion-ion interaction; their values are obtained by empirical fitting. This is achieved by changing the values of these parameters until the predicted structure is in close agreement with the experimental one.

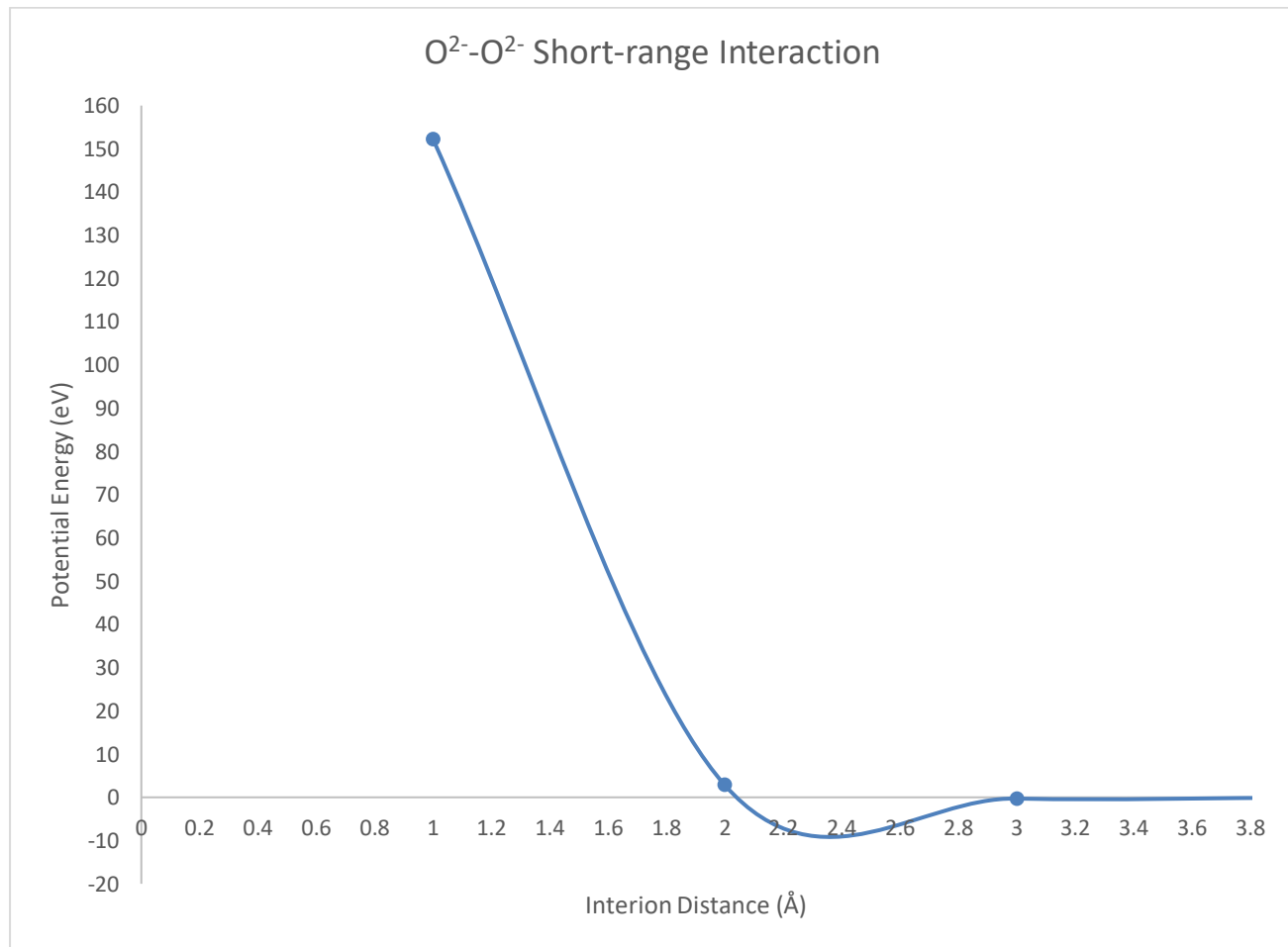


Figure 2.1 A plot illustrating the short-range O-O interaction for FeSb₂O₄

2.2.3 Polarizability

Ionic polarization arises due to the distortion of the distribution of the valence shell electrons due to the presence of charged ions or atoms in close proximity with each other. This phenomenon affects the accurate reproduction of the crystal structure, interionic bond distances and the mechanical properties such as the elastic constants and the dielectric constants. Hence, it is important to include this phenomenon in the fitting of parameters for the potential model.

A simple mechanical model called the Shell Model proposed by Dick and Overhauser⁵⁷ was employed to describe this phenomenon. In the application of this approach, the total charge of an ion was partitioned into a core (X) which was made up of the inner electrons and a massless shell (Y) which comprised the valence shell electrons. The core and the shell were connected with a harmonic spring. The value of the spring constant (k) of the spring allowed the core and shell to relax independently of each other during the energy minimisation process. Polarizability (α) of an ion with respect to the charge of the core and shell (Y) and the spring constant (k) of the harmonic spring can be calculated by the following equation.

$$\alpha = \frac{1}{4\pi\epsilon_0} \left(\frac{Y^2}{k} \right) \quad (2.6)$$

An illustration of the Shell Model is presented in *figure 2.2*. Here the black sphere represents the core and the outer grey sphere represents the shell. The degree of polarizability is governed by the stiffness or the spring constant of the spring. If the spring is very stiff then the electron shell will be stationary and polarisation would not happen, even under the presence of an external electric field (resulting from the ions in close proximity), if the spring is too loose then the electron shell could move far away from the core resulting in the structure to collapse. Hence, the core-shell charges and the spring constant need to be chosen carefully.

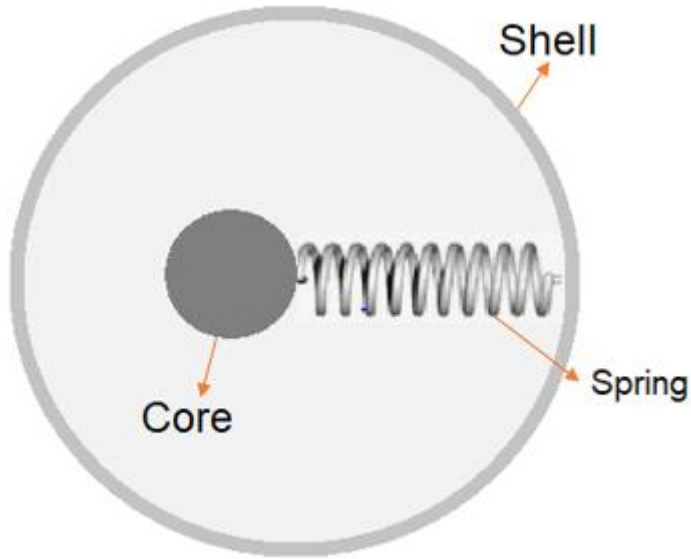


Figure 2.2 Representation of the Shell Model

2.3 Perfect lattice simulation

Once a set of pairwise potential parameters are able to accurately reproduce the crystal structure, it is then possible to study the physical properties and defect behaviour of that system. Hence, it is essential to select suitable parameters and to obtain an optimised crystal structure with respect to these parameters using a suitable energy minimisation or geometry optimisation process.

2.3.1 Energy Minimisation

Energy minimisation is essentially the systematic alteration of lattice parameters with respect to the selected potential model until the net force F on each ion due to its neighbouring ion is minimised (*equation 2.7*). The structure thus obtained may or may not be an exact reproduction of the experimental crystal structure with a 100% accuracy; it could be slightly different as the ions relax with respect to the interionic forces and the interatomic parameters. This structure corresponds to a thermodynamically low energy configuration.

$$F = \frac{\partial E}{\partial r} = 0 \quad (2.7)$$

The internal energy E of the system can be expressed as a Taylor series at any given configurational space (*Equation 2.8*), where the first derivative is termed as the gradient vector g and the second derivative is termed as the Hessian matrix H . However, the energy of a crystal is a multidirectional function based on the ionic coordinates with a complex energy surface. The minimum point on this surface refers to the most stable and low energy point. If one deviates even slightly from this position, then the next point will be less stable and of higher energy. This expansion is truncated at either the first or the second derivative depending on the energy minimisation technique being used.

$$E(x + \delta x) = E(x) + \frac{\partial E}{\partial x} \delta x + \frac{1}{2!} \frac{\partial^2 E}{\partial x^2} (\delta x)^2 + \dots \quad (2.8)$$

Most energy minimisation algorithms work on the principle of calculating the gradient or the first derivative of the internal energy of the system with respect to its lattice parameters. The gradient vector provides information about the direction of the search. Two of the commonly used algorithms that calculate the gradient are the *steepest descents* and the *conjugate gradients* method.

The *steepest descent* method looks for the direction with the highest gradient and then searches for a minimum along that direction. This is an iterative process and it is repeated till a minimum value is found. This method is limited to the data regarding the current step as the information regarding the energy hypersurface (information from all the previous steps) is ignored. This can be computationally exhaustive if the starting point is far away from the minimum value or if one is trapped in some local minima.⁹⁶

The *conjugate gradient* method is more efficient than the steepest descent, as it combines the information from the previous searches with the current search and thus ensures a rapid convergence. This is achieved by selecting a new search direction independent to the previous search directions and comparing the two before proceeding to the next step. For an N -variable system, the directionality is reduced by 1 every single time and hence a minimum is guaranteed at the end of N steps.⁹⁷

Another efficient yet more time-consuming method that relies on calculating both, the first and the second derivatives is the *Newton Raphson* method. Here the displacement vector Δx is determined from the current position to the minimum position by using *equation 2.9*.

$$\Delta x = -\alpha H^{-1} g \quad (2.9)$$

Here α is a scaling factor, which is determined by a repeated line search along the direction of the search vector to determine one-dimensional minima. This factor is useful as most initial configurations, or the starting points of the optimisation process are not close to the absolute minima and the system is not harmonic. The only advantage of using this process is that it stores the information from each Hessian Matrix H , calculated during the optimisation process. The number of atoms in the system determines the size of the matrix (core and shells both if using a core and shell model). This could result in very large matrices for systems containing a large number of atoms in their unit cell. Thus, a combination of conjugate gradient method and the Newton Raphson method is commonly used for locating a minimum in a time-efficient manner. The latter follows the conjugate gradient method when the search is closer to suitable local minima on the energy surface. All the methods described above aim to find a suitable local minima as opposed to global minimum.

2.3.2 Physical Properties

Once the crystal structure has been optimised, it is then possible to calculate various physical properties using the second derivatives of the energy function. Properties that can be calculated include the elastic constants, the bulk and the shear modulus, the dielectric constants etc. These properties play an important role in describing the behaviour of the lattice under different kinds of perturbations. Some of the most commonly calculated properties are explained below.

Elastic Constants

The elastic constants are calculated taking the second derivative of the energy density function with respect to the strain applied to the system. These elastic constants are used to determine the mechanical hardness of the system under study and the degree of deformation with respect to the external stress applied on to the system. There can be six different types of applied strain and hence the elastic constant tensor takes the form of a 6×6 matrix.⁹⁸ The elastic constants can be calculated by using equation 2.10.

$$c_{ijkl} = \frac{1}{V} (W_{SS} - W_{SC} W_{CC}^{-1} W_{CS}) \quad (2.10)$$

Here V is the volume of the unit cell, Wss is the strain-strain second derivative matrix Wsc & Wcs is the mixed Cartesian-strain second derivative matrix and Wcc is the Cartesian space coordinate second derivative matrix.

Dielectric Constants

The static dielectric constants are calculated at low and high-frequency limits and are given by a 3×3 matrix. The elements of the matrix are calculated using *equation 2.11*

$$\epsilon_{\alpha\beta} = \delta_{\alpha\beta} + \frac{4\pi}{V} q^T W_{CC}^{-1} q \quad (2.11)$$

Here q is the charge of each ionic species and α, β are the cartesian directions. The static dielectric constant matrix is summed over both the cores and shells of the ionic species, whereas the high frequency is summed only over the shells.

Other properties that can be calculated include phonon modes, the density of states and dispersion curves. These properties can be directly compared with the experimental data and hence can be used to validate the potential model. In the absence of experimental data, these properties can be used as predictive data.

2.4 Defect Calculations

Once the geometry of the lattice has been optimised with respect to an appropriate potential model, it is then possible to introduce defects in the lattice. The creation of defects causes the ions around the defect to be disturbed in order to accommodate the defect. The interaction between the defect and the lattice ions are Coulombic in nature and hence the effect is long-range. The degree of perturbation decreases with the increase in distance from the defect. Defects can be accurately modelled by using the Mott-Littleton method⁹⁹ wherein the material is divided into two regions namely- the inner region (region1) close to the defect and the outer region (region 2a and region 2b) which is further away from the defect. The schematic of this approach is given by *figure 2.3*.

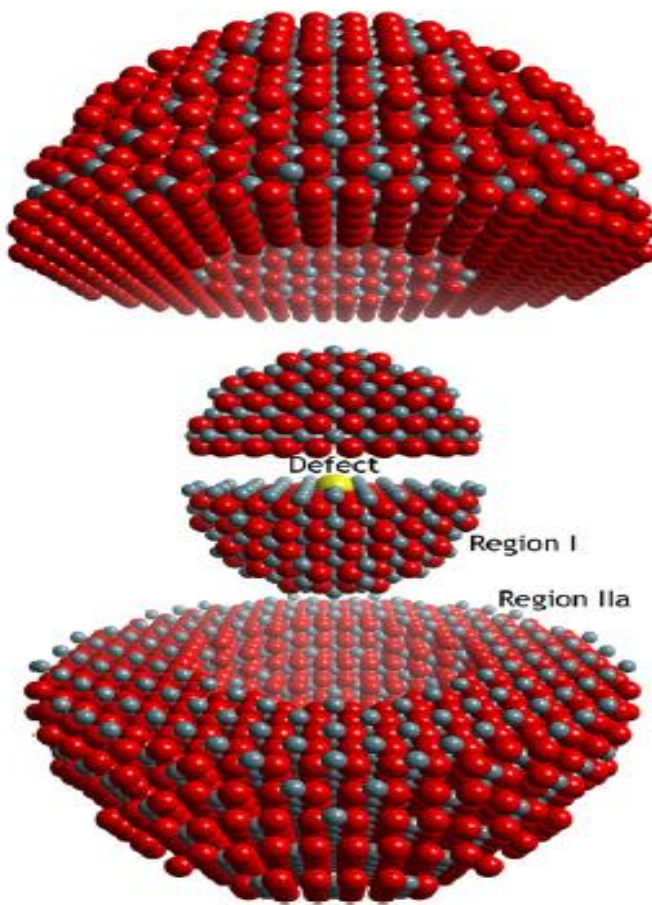


Figure 2.3 An illustration of the Mott-Littleton Model⁹⁰

The defect energies of the defective lattice are calculated by minimising the energy function of the lattice with respect to the displacement of ions that surround the defect. Difference between the minimum energy function of the pure and the defective lattice gives the corresponding defect energy.

Region I (consisting of more than 410 ions) consists of the ions which are in close proximity to the defect centre. The perturbation due to the force exerted by the defect in the region is maximum and hence ions in this region are allowed to relax explicitly using Newton-Raphson minimisation. Region II is further away from the defect centre and consists of all the ions outside the region I until infinity. This region is further subdivided into region IIa and region IIb. Region IIa acts as a buffer region between region I and region IIb and the ion relaxations here are also explicitly calculated as region I. Region IIb is considered as a dielectric continuum where the defect forces in this region are weaker than region IIa. The ion displacement in this region is considered to be a result of the polarisation due to the defect in region I. This effect has been summarised by *equation 2.12*.

$$P = \frac{V}{4\pi} \left(1 - \frac{1}{\varepsilon}\right) \frac{qr}{r^3} \quad (2.12)$$

Where P is the polarisation per unit cell at a point r from the defect centre, V is the volume of the unit cell; q is the effective charge of the defect and ε is the static dielectric constant. The total defect energy E_D is a summation of the energies of the two regions and can be calculated by using *equation 2.13*

$$E_D = E_I(x) + E_{IIa}(x, y) + E_{IIb}(y) \quad (2.13)$$

Here $E_I(x)$ is the energy of region I with respect to the Cartesian coordinates, $E_{IIb}(y)$ is the energy of region II as a function of the Cartesian displacements and $E_{IIa}(x, y)$ is the energy of interaction between the two regions. It is the energy associated with region IIa, which facilitates a smoother convergence during the minimisation process.

2.5 Mean Field and Supercell Approach

Materials with more symmetry degenerate sites as compared to the ions that can occupy them or mixture of ions sharing the same position are known as partially occupied sites. These sites present an added difficulty when it comes to simulating these materials. This problem can be overcome by the construction of a *supercell* with the same material composition and stoichiometry as the real system. This system is searched for the most thermodynamically stable structure in the configuration space. One of the problems with this approach is the number of possibilities that need to be individually located and examined to determine the most stable configuration is high and it increases significantly with the increase in the size of the supercell. The second is the simulations could also result in the loss of crystal symmetry. This method is useful for simulations where the structural knowledge of individual ions and their corresponding bond distances needs to be determined.

The alternate approach modelling systems partial occupancy is the mean field approach. This is an approximate approach, where all the atoms in the system are assigned an occupancy factor O_i between 0 and 1. Then the product of their corresponding occupancy factor scales the sum of all the interaction. The inclusion of partial occupancies is in-built in GULP through the creation of pseudo ions. This method works well for complex structures, as the experimental data is also based on average values.

Chapter 3: Derivation of Pair Potentials

3.1 Introduction

The availability of effective and robust pair potentials forms the basis of all atomistic simulations. It is important that these potentials are able to reproduce both the system under investigation and their experimentally determined properties. Moreover, these potentials must be transferrable to other systems with similar interactions as found in the original system from which they were derived, only then can they be employed to make accurate and valid predictions. To date, there are no potential sets available that were derived to fit the systems under examination, namely FeSb_2O_4 and $\text{Ca}_5\text{Ir}_3\text{O}_{12}$. Hence all the pairwise potential values were either derived from scratch or by modifying the existing ones to accurately reproduce the crystal structure of the systems mentioned above. The rest of the chapter will discuss the fitting methodology developed to suit both FeSb_2O_4 and $\text{Ca}_5\text{Ir}_3\text{O}_{12}$.

3.2 Basic Fitting Methodology

All static lattice calculations performed in this study were performed using the GULP code.⁸⁸ The short-range Buckingham potential parameters A , ρ and C and the shell model parameters Y and k as described in *Chapter 2* were derived empirically. The empirical fitting procedure is an iterative process that simply involves the adjustment of the above-mentioned parameters until a good agreement between the experimental and calculated properties has been reached. The quality of the fit to experimental data was determined by using a least square method, which minimizes the difference between experimental and calculated properties.

$$F = \sum w \left(\frac{f_{cal} - f_{exp}}{f_{exp}} \right)^2 \quad (3.1)$$

The properties that were used in this study were the lattice constants, the bond lengths, lattice energies, the number of cycles required for achieving geometry optimisation. In the above equation F is the sum of squares, the f_{calc} and f_{exp} are the calculated and observed/experimental properties

respectively. Each property was assigned a weighting factor w , which allows the fit to be weighted towards the property of choice. As the only experimental data available related to the crystal structure hence all the three lattice constants were assigned the same weight. ($w=1$). In order to obtain an unbiased contribution of values belonging to different categories, the least square differences were normalised. This methodology is similar to the one used by Read *et al.*⁹⁰ The parameters for both compounds under study, FeSb₂O₄, Ca₅Ir₃O₁₂ and their aliovalent substitution species were fitted to their basic oxide and the pure phases. Efforts were made to make sure that the sum of the deviations from the experimental lattice parameter was less than 1% for each system.

3.3 FeSb₂O₄ Potentials

The compound FeSb₂O₄ consists of iron bonded to six oxygen ions in an octahedra and antimony bonded to three oxygen ions with a pair of lone pair of electrons. In order to accurately reproduce the crystal structure, the short-range cation-anion (Fe²⁺-O²⁻, Sb³⁺-O²⁻) and anion-anion (O²⁻-O²⁻) interactions were described using a Buckingham Potential form (as outlined in *Chapter 2*) and the core-shell model was used to account for the polarisation of the ions. There a number of robust and transferrable Fe²⁺-O²⁻ and O²⁻-O²⁻ potentials fitted to a range of crystal structures. However, to the best of my knowledge a robust Sb³⁺-O²⁻ has not been reported so far.

3.3.1 Modelling the Lone Pair of Electrons

As outlined in *Chapter 1*, each Sb³⁺ ion has a lone pair of electrons pointing into the one-dimensional channels that exist along the *z-axis*. These lone pairs act as the fourth ligand and exert a strong electrostatic repulsive force, which is responsible for stabilising these one-dimensional channels. Hence, it is crucial to accurately model the effect of the antimony electron lone pair. However, the challenge was to come up with a suitable methodology that could achieve this and be robust enough to allow chemical manipulation with the structure for studying its defect properties. The

literature on modelling compounds with lone pairs of electrons was scarce and the studies by Islam *et al.*^{13–15} and Lin *et al.*^{100,101} were the only two examples of cases where atomistic modelling was used to model the crystal structure of compounds having lone pairs. Both the studies firstly used the shell-model to account for the polarization resulting from the presence of the lone pairs and secondly, described the cation-cation interaction in addition to the cation-anion and anion-anion interactions, to model the repulsion between the lone pair of electrons present on the cations involved.

The study by Islam *et al.*¹³ successfully modelled the crystal structures of Aurivillius phases that contain compounds with Bi³⁺ ions that also have the added difficulty of the strong electrostatic repulsion due to the lone pair of electrons. In order to accurately model the effect of the force exerted by the lone pairs of electrons, the Bi³⁺-Bi³⁺ short-range interaction was derived along with other cation-anion and anion-anion interactions. Similarly, the study by Lin *et al.*^{100,101} attempted to study the both intrinsic and extrinsic (effect of different impurity cations) behaviour in lead tungstate using the Pb²⁺-Pb²⁺ short-range interaction in addition to rest of the pair potentials to model the lead tungstate crystal. The short-range parameters and the calculated crystal structures of Bi₂WO₆, αPbO and PbWO₄ are summarized in *table 3.1* and *3.2* respectively.

Table 3.1 Summary of the previously published potentials set for compounds with lone pair of electrons

<i>Short Range Parameters</i>			<i>Shell Model</i>			
<i>Interaction</i>	<i>A(eV)</i>	<i>ρ (Å)</i>	<i>C (eV/Å⁶)</i>	<i>Y(e)</i>	<i>k (eV/Å²)</i>	<i>Ref.</i>
<i>Bi₂WO₆</i> ¹³⁻¹⁵						
<i>Bi³⁺...Bi³⁺</i>	24 244.50	0.3284	0.00	-5.51	359.55	13
<i>Bi³⁺...O²⁻</i>	49 529.35	0.2223	0.00	-5.51	359.55	13
<i>W⁶⁺...O²⁻</i>	767.43	0.4386	0.00	5.89	7.69	13
<i>αPbO</i> ¹³						
<i>Pb²⁺...Pb²⁺</i>	24.98	0.3284	0.00	-4.00	172.7	13
<i>Pb²⁺...O²⁻</i>	72276.42	0.2223	0.00	-4.00	172.7	13
<i>O²⁻...O²⁻</i>	9547.96	0.2192	32.0	-2.04	6.3	13
<i>PbWO₄</i> ^{100,101}						
<i>Pb²⁺...Pb²⁺</i>	18912.1140	0.313781	2.60	-0.09	21006.539	100
<i>Pb²⁺...O²⁻</i>	8086.8038	0.264866	3.5636	-0.09	21006.539	100

The listed potentials were employed to reproduce the crystal structures to verify the use of an additional cation-cation interaction. The difference between the observed and calculated crystal structures of Bi_2WO_6 and PbWO_4 indicated that the potentials were able to reproduce these complex structures well within the percentage difference limit of 3%. However, the difference between the actual and predicted values for αPbO turned out to be larger than the values reported in the study. Attempts were made to vary the short-range cut-off between 6 Å to 25 Å, but no set of predicted values came close to the reported or experimental ones. $\text{Pb}^{2+}\text{-O}^{2-}$ and $\text{Pb}^{2+}\text{- Pb}^{2+}$ potentials derived in the later part of this study to fit a similar compound, Pb_3O_4 were also unsuccessful in reproducing the αPbO crystal structure within the overall difference of 0.3Å or 3%.

Table 3.2 Summary of the quality between the experimental and predicted structures of compounds with lone pair of electrons

Parameter	Experimental	Calculated		%Difference	
$\text{Bi}_2\text{WO}_6^{102}$		<i>Islam et al.</i> ¹⁵	<i>Present study</i>	<i>Islam et al.</i> ¹⁵	<i>Present study</i>
a	5.4373	5.4113	5.4113	-0.48	-0.48
b	16.4302	16.7710	16.7710	2.07	2.07
c	5.4584	5.5340	5.5340	1.39	1.39
α, β, γ	90°	90°	90°	0	0
$\alpha\text{ PbO}^{103}$		<i>Islam et al.</i>	<i>Present study</i>	<i>Islam et al.</i>	<i>Present study</i>
a	3.975	3.9748	3.9475	-0.01	-0.69
c	5.023	5.0227	5.3552	-0.01	6.61
α, β, γ	90°	90°	90°	0	0
PbWO_4^{104}		<i>Lin et al.</i> ¹⁰⁰	<i>Present study</i>	<i>Lin et al.</i> ¹⁰⁰	<i>Present study</i>
a	5.441	5.456	5.456	0.27	0.27
c	12.024	12.020	12.020	-0.03	-0.03
α, β, γ	90°	90°	90°	0	0

The grid search method for empirical derivation of the potentials for this structure resulted in very few solution sets with an overall difference of 9% between the initial and final values. This could be a result of the complexity of the crystal structure and the lack of availability of properties (mechanical and dielectric constants) other than the crystal structure to fit the potentials to.

3.3.2 Sb₂O₃ potentials

This methodology was employed to fit the Sb-O and Sb-Sb potentials of binary phase Sb₂O₃ (Valentinite¹⁰⁵). Initially, two models were used to test this methodology.

- i. In the first model, the crystal structure was described using the cation-anion (Sb³⁺-O²⁻) and anion-anion (O²⁻-O²⁻) potentials, without using the cation-cation potential (Sb³⁺-Sb³⁺). The unit cell in this model failed to optimise and achieve a thermodynamically stable structure.
- ii. In the second model the crystal structure was described using the Sb³⁺-Sb³⁺ potential in addition to the Sb³⁺-O²⁻ and O²⁻-O²⁻ potentials. The crystal structure did optimise but the discrepancy between the calculated and experimental values was almost 19%.

From the above two models, it was evident that the use of an additional cation-cation potential enables the crystal structure to achieve a geometry optimised state, however, there was a need to refine the potentials to get a better agreement between the experimental and predicted crystal structure. Owing to the lack of any Sb³⁺-O²⁻ and Sb³⁺-Sb³⁺ potentials, the potential values of Bi³⁺-O²⁻, Bi³⁺-Bi³⁺ and O²⁻-O²⁻ from Islam *et al.*¹³ were chosen to be a reasonable starting point used to describe the short-range interaction of antimony and oxygen ions in the two models as a sensible starting point.

An attempt was made to vary the core-shell parameters and the spring constant but due to the lack of any dielectric constant values to fit the parameters to and due to the inability of the potentials to work with the different core-shell and spring constant parameters these values were directly transferred from the Islam *et al.* study¹³. The short-range cut off was set to 12 Å. The pairwise

potentials were fit systematically and iteratively, starting from Sb³⁺-O²⁻ as the total discrepancy between the calculated and experimental structure was the least for this interaction as compared with Sb-Sb and O-O. The crystal structure is orthorhombic hence a root mean square value of the percentage difference for the three lattice constants, a , b , and c was used to determine the over-all deviation $\Delta\delta$ associated with each set of A and ρ values. The largest value acceptable value of $\Delta\delta$ was considered to be +/-3% as compared with the experimental data.

$$\Delta\delta = \sqrt{\delta a^2 + \delta b^2 + \delta c^2} \quad (3.2)$$

The initial combined least-squares sum and error or difference surfaces resulting from the coarse refinement of the Sb-O interaction didn't have any solution set that was between the 0 to 3% error or difference range. Hence, the solution sets with the least square sum range between 0 and 1 the smallest difference (equivalent to ~7.5%) were used in further refinement of the Sb-Sb and O-O potentials. This process was repeated until the over-all difference and the least-squares sum were minimised and a good agreement between the predicted and experimental crystal structure was achieved. The final least square sum surface as a function of the potential parameters A and ρ are given in *figure 3.1*.

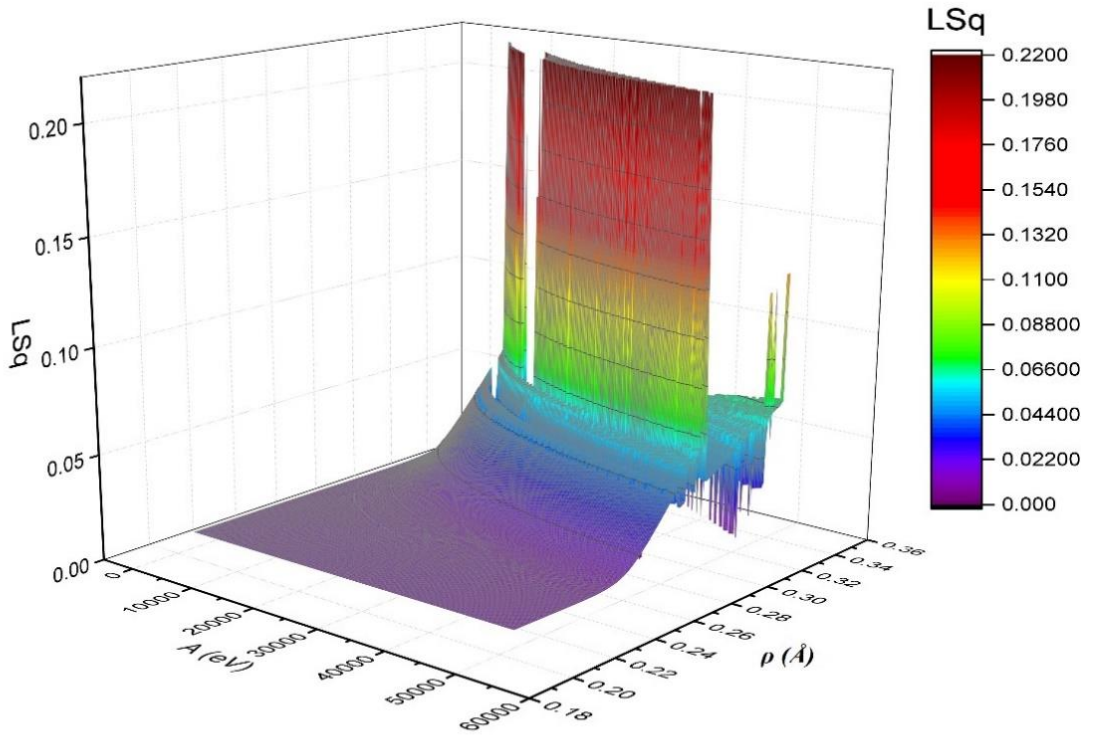


Figure 3.1 Least Square Sum surface constructed from the potential parameter set for Sb-Sb interaction

The solution sets situated along the purple area of the graph had the best agreement with the experimental data. These sets were further tested by performing point defect calculations to check the accuracy of the model and the robustness of the potential set. Due to the lack of availability of any experimental data on mechanical and dielectric properties, the robustness and the accuracy of the potential values were tested by their ability to achieve a geometry optimised state when point defects namely vacancies and interstitials were introduced in the system. The solution sets that were able to successfully allow the introduction of O and Sb vacancies were selected and they were then used to reproduce the cubic phase of Sb_2O_3 . The final potential values, the resulting crystal structure, the mechanical properties and the position and energy of the oxygen and antimony vacancies are summarised in *table 3.3, 3.4 and 3.5*.

Table 3.3 Summary of the Short-Range Potential Parameters Fitted for the orthorhombic phase of Sb₂O₃

Short Range Parameters				Shell Model		
Interaction	A(eV)	ρ (\AA)	C (eV/\AA^6)	Y(e)	k (eV/\AA^2)	Ref.
Sb³⁺...Sb³⁺	35014	0.2990	0.00	-5.51	359.55	<i>Fitted</i>
Sb³⁺...O²⁻	27300.29	0.241961	0.00	-5.51	359.55	<i>Fitted</i>
O²⁻...O²⁻	9701.33	0.21799	32.5	-2.04	6.3	<i>Fitted</i>

Table 3.4 Summary of the quality of fit between the experimental and calculated structure of the orthorhombic and cubic phase of Sb₂O₃

Lattice Constant	Experimental (\AA)	Calculated (\AA)	% Difference
Sb₂O₃- orthorhombic phase;¹⁰⁶ Lattice energy = -132.94 (eV)			
a	4.9290	4.9430	0.30
b	12.4850	12.3680	-0.93
c	5.4300	5.4440	0.27
Sb₂O₃- cubic phase;¹⁰⁷ Lattice energy = -132.84 (eV)			
a	11.1519	11.4733	2.88

Table 3.5 Summary of the calculated Mechanical properties

<i>a) Mechanical Properties</i>	
<i>Elastic Constants (GPa)</i>	<i>Calculated</i>
C_{11}	63.4411
C_{12}	70.1922
C_{13}	98.6829
C_{33}	3.5731
C_{44}	117.8885
C_{66}	132.6207
<i>Bulk Modulus (GPa)</i>	
<i>Reuss</i>	75.6679
<i>Voigt</i>	91.4640
<i>Hill</i>	83.5660
<i>b) Defect Energies for Sb and O</i>	
<i>Species</i>	<i>Defect Energy (eV)</i>
Sb^{3+}	42.38
$O^{2-} (1)$	8.64
$O^{2-} (2)$	13.68

These values were then transferred to simulate the FeSb_2O_4 ⁹ crystal structure; all the published Fe-O potentials were tested with the Sb and O potentials derived from Sb_2O_3 . Potential parameters by Catlow *et al.*,¹⁰⁸ resulted in the least percentage difference on the lattice constants and the crystal structure and hence was employed as a sensible starting point for the Fe-O interaction. The short-range potential cut-off was set as 12 Å. The starting potential values, the core and shell parameters, the spring constants have been summarised in *table 3.6*

Table 3.6 a) Starting Potential Parameters for FeSb_2O_4 ; b) Initial Structural Parameters for FeSb_2O_4

<i>a) Starting Short Range Potential Parameters</i>						
<i>Interaction</i>	<i>Short Range Parameters</i>			<i>Shell Model</i>		
	<i>A(eV)</i>	<i>ρ (Å)</i>	<i>C (eV/Å⁶)</i>	<i>Y(e)</i>	<i>k (eV/Å²)</i>	<i>Ref.</i>
$\text{Fe}^{2+}\cdots\text{Fe}^{2+}$	1207.6	0.3084	0.00	2.997	62.9	108
$\text{Sb}^{3+}\cdots\text{Sb}^{3+}$	35014	0.2990	0.00	-5.51	359.55	<i>Fitted</i>
$\text{Sb}^{3+}\cdots\text{O}^{2-}$	27300.29	0.241961	0.00	-5.51	359.55	<i>Fitted</i>
$\text{O}^{2-}\cdots\text{O}^{2-}$	9701.33	0.21799	32.5	-2.04	6.3	<i>Fitted</i>

<i>b) Initial Crystal Structure⁹</i>			
<i>Lattice Constant</i>	<i>Experimental (Å)</i>	<i>Calculated (Å)</i>	<i>% Difference</i>
a, b	8.6175	8.3619	-2.97
c	5.9207	6.1536	3.93
$\alpha \beta \gamma$	90°	90°	0

It was evident that the potential parameters were able to successfully reproduce a geometry optimised crystal structure with a small difference between the experimental and predicted values. This discrepancy was attributed to the different coordination environments of antimony, iron and oxygen ions in Sb₂O₃, FeO and FeSb₂O₄. This suggested that the potential values needed further refinement to fit the crystal structure of FeSb₂O₄.

Schafarzikite is a new and novel compound and thus there is a scarcity of physical data other than the crystal structure to fit the potentials to. As outlined in Chapter 1, this study was the first instance where FeSb₂O₄ was modelled and studied using atomistic techniques. The fitted potentials would be employed to study the possibility and the effect of oxygen and fluorine insertion into the one-dimensional channel having lone pair of electrons. Hence, all potentials derived during this study were tested through their ability to reproduce the pure lattice accurately and work well with the crystal structure that had oxygen vacancies and interstitials.

3.3.2 Anion-Anion potentials

Finding a robust set of potential values that could reproduce the crystal structure with a 3% or less difference between the expected and the predicted structure and allow the introduction of point defects and impurities was challenging. An attempt made using the Buckingham four range potential form for O-O derived by Read *et al.*⁹⁰ failed to achieve a geometry optimised structure and resulted in unnaturally large core-shell separation - 1.02 Å approximately.

The range of values varied until this point were between 10 to 40,000, 0.2 to 0.4 and 1 to 50 for A , ρ and C parameters respectively. This range was selected by a careful survey of all the published values of O-O potential. Most solution sets that were able to reproduce the crystal structure accurately (within the 3% error or difference limit) failed to optimise when vacancies of oxygen, iron and antimony were created. These crystal structures had good agreement with the experimental values of lattice constants a and b , but the difference along lattice constant c was between 1.5 to 3.5%. The upper

limit of the range of the grid search for the potential parameter C was then increased from 50 to 100. It was observed that the new solution sets resulted in a smaller percentage difference, less than 1.5%, between the experimental and predicted value of the lattice constant c and were able to achieve geometry-optimised structure even with introduction points defects like vacancies and interstitials in the system. However, all these systems resulted in a large negative value (equal to -75 eV approximately) for the creation of oxygen, iron and antimony vacancies.

The upper limit was further increased to 350 while keeping the grid search range for A and ρ same as mentioned earlier. *Figure 3.3* and *3.4* shows the percentage difference surface of lattice constants a and c as a function of the potential parameters A , ρ and C . The solution sets along the yellow area in the percentage difference surfaces resulted in a difference close to zero and were chosen for further testing. The selected sets were tested with a defected system with antimony, oxygen and iron vacancies. The energy for creating vacancies in the system now ranged between 0.2eV to 2eV, 1eV to 3eV and 12eV to 25 eV for oxygen, iron and antimony, respectively. The solution set with the highest defect energy value for each species, the lowest percentage difference along lattice constant c and the best agreement between the actual and predicted structure was then selected for refinement of Sb-O, Sb-Sb and Fe-O potentials.

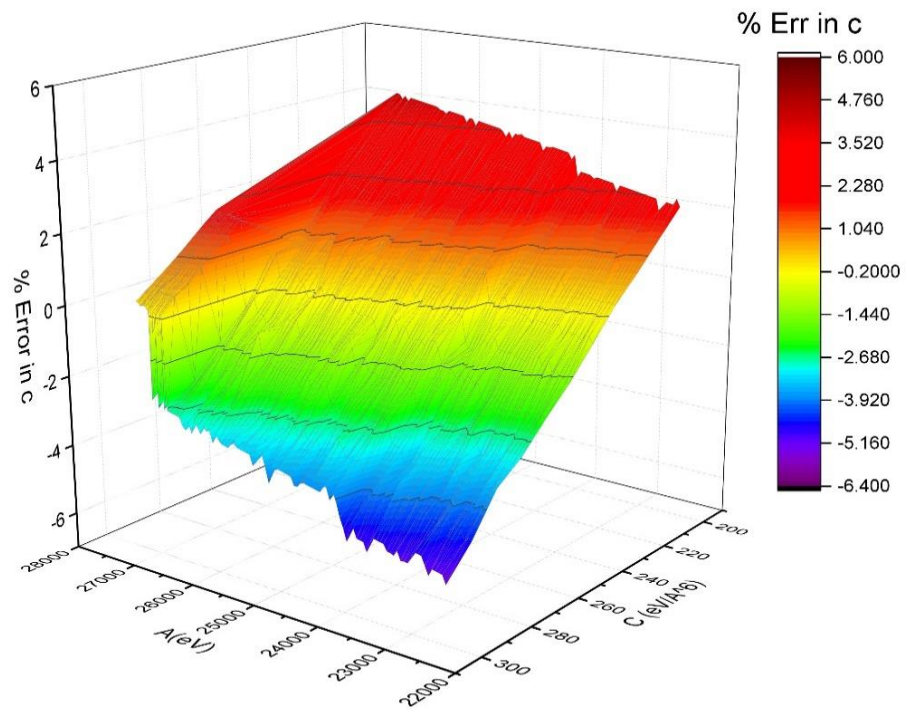


Figure 3.3 Percentage difference surface in c as a function of potential parameter A and C

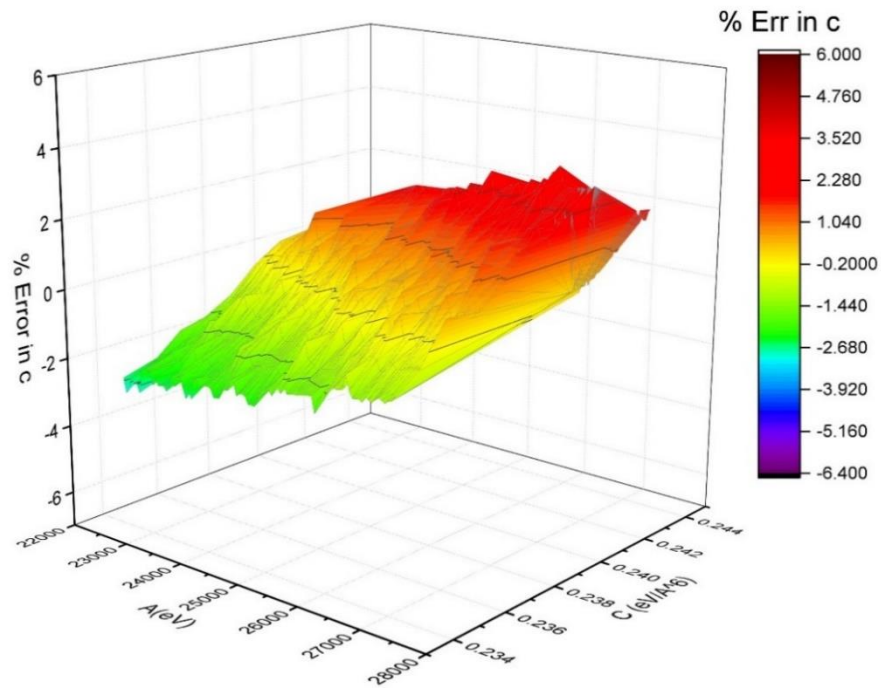


Figure 3.4 An illustration of the Percentage difference surface (along c axis) plotted as a function of potential parameters: A and ϕ

3.3.3 Cation-Anion, Cation-Cation potentials

The Sb-Sb and Sb-O potentials were adjusted simultaneously. The initial coarse refinement resulted in many solution sets where the difference between predicted and experimental crystal structure was less than 3%. Out of these solution sets, the ones, which resulted in, smaller than 0.2% difference between the predicted and experimental value of lattice constant c , were selected for the further refinement to increase the accuracy of the predicted results. The selected solution sets were used to reproduce system with vacancies and those that resulted in positive defect energy values for creating an oxygen vacancy that were close to or more than 3 eV were selected for the refinement of Fe-O potentials.

The aim was to refine the potential parameters until the final defect energy value for creating an oxygen vacancy was between 7eV to 14eV. The same procedure was repeated for fitting the Fe-O potential. The potential parameters that resulted in a difference smaller than 0.1% between the actual and predicted crystal structure and lattice constant c were selected for fine refinement and testing. *Figure 3.5* gives the root mean square (RMS) or a combined error or difference surface for the Fe-O refinement plotted as a function of potential parameters A and ρ .

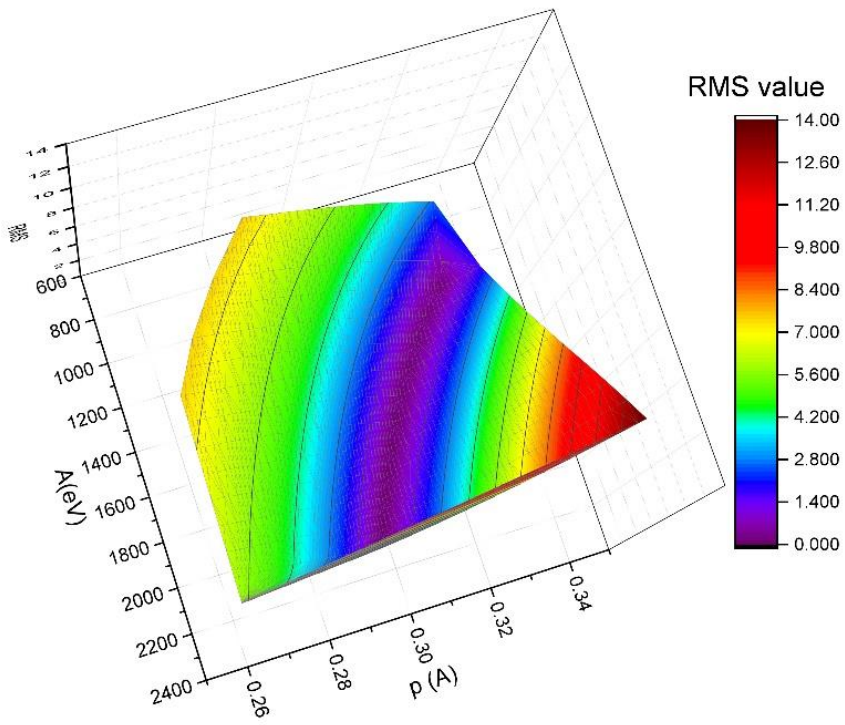


Figure 3.5 RMS value surface for the final refinement of Fe-O potential

The solution set selected at the end of the fitting procedure resulted in an overall difference of 0.16 % and the difference between the actual and predicted value of lattice constant c was 0.15%. The potential parameter set and the resulting lattice parameters, the inter-ionic separation and the fractional coordinates are summarised *in table 3.7, 3.8 and 3.9.*

Table 3.7 Summary of the final short-range potential parameters for FeSb₂O₄

<i>Final Short-Range Potential Parameters</i>						
<i>Short Range Parameters</i>				<i>Shell Model</i>		
<i>Interaction</i>	<i>A(eV)</i>	<i>ρ (Å)</i>	<i>C (eV/Å⁶)</i>	<i>Y(e)</i>	<i>k (eV/Å²)</i>	<i>Ref.</i>
Fe²⁺...Fe²⁺	1230	0.325	0.00	2.997	62.9	<i>Fitted</i>
Sb³⁺...Sb³⁺	18100	0.3330	0.00	-5.51	359.55	<i>Fitted</i>
Sb³⁺...O²⁻	9100	0.2787	0.00	-5.51	359.55	<i>Fitted</i>
O²⁻...O²⁻	27299	0.24387	300	-2.04	6.3	<i>Fitted</i>

Table 3.8 Summary of the goodness of fit on the fitted potentials for FeSb₂O₄

<i>Lattice Constant; Lattice energy = -171.24 (eV)</i>				
	<i>Experimental (Å)⁹</i>	<i>Calculated (Å)</i>	<i>Difference (Å)</i>	<i>% Difference</i>
a, b	8.6175	8.6202	0.002	0.03
C	5.9207	5.9293	0.008	0.15
α β γ	90°	90°	0	0
<i>Inter-ionic separation</i>				
Fe-O1	2.186	2.165	0.021	0.96
Fe-O2	2.104	2.318	-0.214	-10.10
Sb-O1	1.998	2.035	-0.037	-1.85
Sb-O2	1.932	2.100	-0.168	8.69

Table 3.9 Summary of all the fractional coordinates of Schafarzikite- FeSb_2O_4

<i>Species</i>		<i>Experimental</i>	<i>Calculated</i>	<i>%Difference</i>
<i>Fe</i>				
	<i>x</i>	0.0	0.0	0
	<i>y</i>	0.5	0.5	0
	<i>z</i>	0.25	0.25	0
<i>Sb</i>				
	<i>x</i>	0.1772	0.1656	6.50
	<i>y</i>	0.1648	0.1604	2.60
	<i>z</i>	0.00	0.00	0
<i>O1</i>				
	<i>x</i>	0.6794	0.6784	0.15
	<i>y</i>	0.1794	0.1784	0.55
	<i>z</i>	0.25	0.25	0
<i>O2</i>				
	<i>x</i>	0.0999	0.0947	5.12
	<i>y</i>	0.6419	0.6821	6.29
	<i>z</i>	0.00	0.00	0

3.3.4 Potential Validation

The structural data summarised in *table 3.8* suggests that the predicted values are in good agreement with the initial crystal structure. The largest discrepancy between the initial and final structure is along the *c-axis*, the direction along which the lone pairs are situated. The final fractional coordinates listed in *table 3.9* also confirms the same as the largest observed difference between the initial and final structure is along with Sb ions, resulting from the displacement of Sb core and shell by 0.02 Å. The Sb shell here represents the lone pairs of electrons and the core-shell displacement represents the Cation-lone pair distance. The interionic distances summarised in *table 3.8* however, suggests an elongation of the Sb-O₂ and Fe-O₂ bonds which results in the distortion of the FeO₆ octahedra as observed in *figure 3.6 (a)*. However, due to the lack of availability of other physical properties to fit to and the overall good agreement between the simulated and observed crystal structure, this solution set selected for further testing.

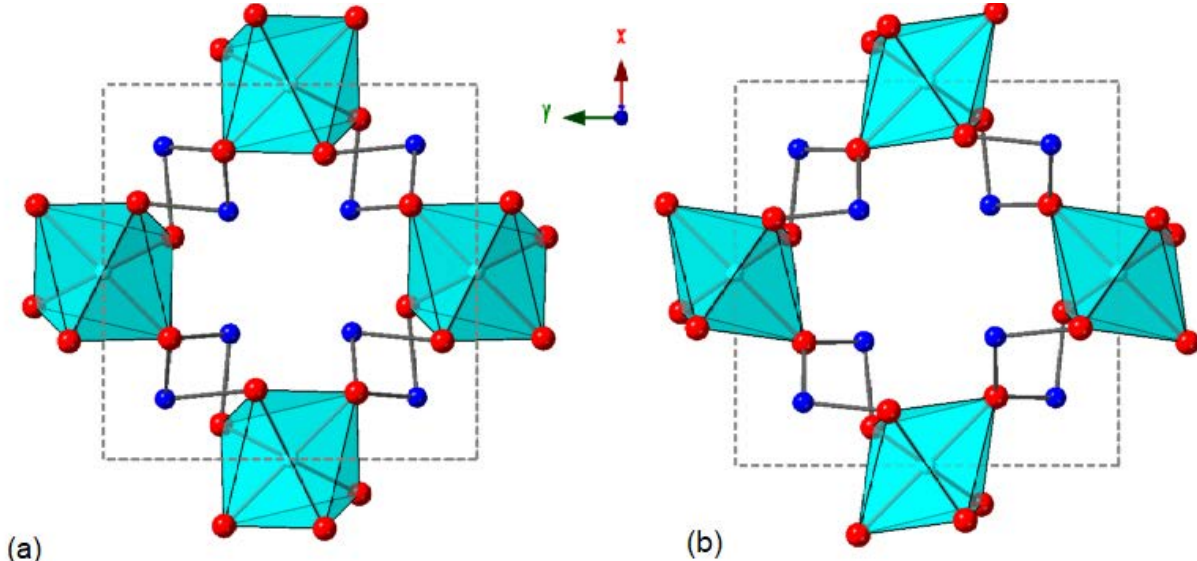


Figure 3.6 An illustration of the predicted and experimentally determined unit cell of FeSb₂O₄ along xy-plane (a) Predicted Crystal structure (b) Experimental Crystal Structure; The blue coloured spheres represent the Fe ions, the indigo coloured spheres the Sb ions and red spheres the O ions.

As these potentials were to be used to study the defect behaviour and oxygen and fluorine insertion in Schafarzikite hence the robustness of the final set of potentials were tested by introducing oxygen, iron and antimony vacancies and oxygen interstitials in the system. The defect energy values for creating oxygen, iron and antimony vacancies and oxygen interstitial looked sensible. The detailed defect chemistry will be discussed in detail in Chapter 4. *Table 3.10* summarises the predicted mechanical properties.

Table 3.10 Summary of the predicted values of elastic constants and defect energy values

<i>Mechanical Properties</i>	
<i>Elastic Constants (GPa)</i>	<i>Calculated</i>
C_{11}	221.2262
C_{12}	129.1240
C_{13}	91.4077
C_{33}	145.9658
C_{44}	1931.0723
C_{66}	118.5600
<i>Bulk Modulus (GPa)</i>	
<i>Reuss</i>	124.4001
<i>Voigt</i>	134.5659
<i>Hill</i>	129.4830

These final set of potentials were then tested for transferability by employing them to reproduce the crystal structure of a few compounds belonging to the Schafarzikite family. The list of the compounds and their resulting crystal structures are given in *table 3.11*. The derived values of Sb-O, Sb-Sb and O-O potentials were transferred to all the four compounds listed in *table 3.11*. Published potentials were employed to describe the Mg^{2+} -O²⁻, Co^{2+} -O²⁻, Pb^{4+} -O²⁻ and average discrepancy of 3% with the experimental structures.^{109–111}

Table 3.11 Summary of the goodness of fit across other phases belonging to the Schafarzikite family

Compounds	Lattice Parameter		
	Experimental	Calculated	%Difference
$MnSb_2O_4$ ¹¹²	<i>a</i> 8.695	8.516	-2.06
	<i>c</i> 6.010	5.929	-1.34
$MgSb_2O_4$ ¹¹³	<i>a</i> 8.476	8.617	1.65
	<i>c</i> 5.938	5.920	-0.33
$CoSb_2O_4$ ¹¹⁴	<i>a</i> 8.481	8.422	-0.70
	<i>c</i> 5.921	5.928	0.12
Pb_3O_4 ¹⁸	<i>a</i> 8.811	8.810	0.01
	<i>c</i> 6.563	6.563	0.00

Other potentials namely, Pb²⁺-Pb²⁺, Pb²⁺-O²⁻, Sb-F and F-F were also derived to standard structures^{18,107} using the empirical fitting procedure which has been discussed in this chapter. These potentials were employed to study the effect of lead substitution on to the antimony site and the fluorine insertion in FeSb₂O₄ the potential values are summarized in *table 3.12*.

Table 3.11 Summary of other pair potentials derived in this study

Short Range Parameters				Shell Model		
Interaction	A(eV)	ρ (\AA)	C (eV/\AA^6)	Y(e)	k (eV/\AA^2)	Ref.
Pb²⁺...O²⁻	110	0.2799	0.00	-4.00	172.7	<i>Fitted</i>
Pb²⁺...Pb²⁺	5314	0.3121	0.00	-4.00	172.7	<i>Fitted</i>
Sb³⁺...F	1200	0.33	0.0	-1.378	24.36	<i>Fitted</i>
F...F	2100	0.27	20.0	-1.378	24.36	<i>Fitted</i>

3.4 Ca₅Ir₃O₁₂ Potentials

Ca₅Ir₃O₁₂ has also not been studied using atomistic simulation techniques prior to the current study and hence there were no potentials fitted to specifically to the compound. The short-range interactions needed to model a thermodynamically stable crystal structure are Ca²⁺-O²⁻ and O²⁻-O²⁻ and Ir^{4.67+}-O²⁻. There were a number of well-known and well utilised Ca-O and O-O potentials in the literature to choose from but there were no potential parameters derived for the Ir ions. Hence, a new Ir-O pair potential was derived to fit Ca₅Ir₃O₁₂ and a similar compound NaIrO₃.

The purpose of deriving the Ir-O potential parameters was the study of the possibility and the mechanism of Na substitution onto the Ca site accompanied by the oxidation of Ir^{4.65+} to Ir⁵⁺ to compensate for the charge imbalance in Ca₅Ir₃O₁₂. Hence, the refinement process was started by first fitting the Na-O, Na-Na and Ir-O potentials to a similar compound with both Na and Ir⁵⁺ ions: NaIrO₃. These potentials were then tested and transferred to model Ca₅Ir₃O₁₂.

The potentials values derived by Binks *et al.*¹¹⁶ were chosen as the starting point for the refinement of Na-Na, Na-O interaction; the O-O potential was fixed to the values derived by Busker *et al.*¹¹¹. The Ru⁵⁺-O²⁻ potential derived by Bush et al.¹¹⁷ was used as the starting value for Ir⁵⁺-O²⁻ interaction. The Shell Model was employed to describe the iridium and oxygen ions, whereas the rigid ion model was used for the sodium ions. The cut-off value was set to 10Å. The starting pair potential values and the resulting crystal structure for NaIrO₃ is given in *table 3.12*.

Table 3.12 Summary of a) the starting potential values for NaIrO₃ b) initially calculated crystal structure values

<i>a) Starting Short Range Potential Parameters</i>					
<i>Short Range Parameters</i>				<i>Shell Model</i>	
<i>Interaction</i>	<i>A(eV)</i>	<i>ρ (Å)</i>	<i>C (eV/Å⁶)</i>	<i>Y(e)</i>	<i>k (eV/Å²)</i>
Na⁺…Na⁺	1677.830	0.2934	0.00	1.00	-
Na⁺…O²⁻	1271.504	0.3000	0.00	1.00	-
Ir⁵⁺…O²⁻	17048.850	0.2219	0.00	0.343	446.3
O²⁻…O²⁻	9547.960	0.2192	32.0	-2.04	6.3
<i>b) Initial Crystal Structure</i>					
<i>Lattice Constant</i>	<i>Experimental (Å)¹¹⁸</i>		<i>Calculated (Å)</i>	<i>% Difference</i>	
a	3.03968		2.9961	-1.43	
b	10.3576		11.0635	6.82	
c	7.1766		7.1865	0.14	
α β γ	90°		90°	0	

The 7% RMS difference between the actual and predicted crystal structure suggested that there was a need for potential refinement to achieve better agreement between the two values. All the potential values were derived using the same grid search method that was used for FeSb₂O₄ potential derivation. As the structure is orthorhombic, the total difference associated with each solution set was calculated using the root mean square method given by *equation 3.2*. Due to the lack of availability of any reported dielectric and mechanical properties, the robustness and accuracy of the potentials were tested by their ability to achieve a geometry-optimised state with vacancies and interstitials in the system. The potentials were derived systematically and iteratively starting from Na-O as the interaction resulted in a considerable decrease in the total difference from 7% to 1.4%. The same procedure was repeated for Ir-O and Na-Na interaction. The final set of potentials resulted in a good agreement with the experimental structure with an average difference of 0.6%. The final solution set and the initial (experimental) and final values (predicted) of the crystal structure are given in *table 3.13*.

Table 3.13 List of the final set of pair potentials for NaIrO₃

<i>a) Final Short-Range Potential Parameters</i>						
<i>Short Range Parameters</i>				<i>Shell Model</i>		
<i>Interaction</i>	<i>A(eV)</i>	<i>ρ (Å)</i>	<i>C (eV/Å⁶)</i>	<i>Y(e)</i>	<i>k (eV/Å²)</i>	<i>Ref.</i>
Na⁺…Na⁺	10209	0.2539	0.00	1.00	Rigid ion	Fitted
Na⁺…O²⁻	387.0	0.328409	0.00	1.00	Rigid ion	Fitted
Ir⁵⁺…O²⁻	5649	0.2648	0.00	0.343	446.3	Fitted
O²⁻…O²⁻	9547.960	0.2192	32.0	-2.04	6.3	111
<i>b) Final Crystal Structure</i>						
<i>Lattice Constant</i>	<i>Experimental (Å)⁸³</i>		<i>Calculated (Å)</i>		<i>% Difference</i>	
a	3.0397		3.0523		0.42	
b	10.3576		10.3737		0.6	
c	7.1766		7.1425		-0.47	
α β γ	90°		90°		0	

These Ir-O and O-O potentials with a suitable Ca-O were then employed to reproduce the crystal structure of $\text{Ca}_5\text{Ir}_3\text{O}_{12}$. All reported Ca-O potentials were tested with the Ir-O and O-O, the potential set by Catlow *et al.*,¹¹⁷ resulted in the least difference between the experimental and predicted crystallographic data and hence was selected to describe the Ca-O interaction. Owing to the non-stoichiometric oxidation state of iridium in this compound, a rigid ion model was employed instead of a core and shell model. The final set of potentials summarised in *table 3.14a* resulted in an average difference of 0.6 with the observed crystal structure (summarised in *table 3.14b*).

Table 3.14 a) Summary of the final potential set for $\text{Ca}_5\text{Ir}_3\text{O}_{12}$ b) summary of the quality of fit and predicted crystal structure

<i>Short Range Parameters</i>				<i>Shell Model</i>		
<i>Interaction</i>	<i>A(eV)</i>	<i>p (Å)</i>	<i>C (eV/Å⁶)</i>	<i>Y(e)</i>	<i>k (eV/Å²)</i>	<i>Ref.</i>
$\text{Ca}^{2+}\cdots\text{O}^{2-}$	2272.741	0.2986	0.00	1.281	34.05	¹¹⁷
$\text{Ir}^{4.67+}\cdots\text{O}^{2-}$	5649	0.2648	0.00	4.67	<i>Rigid ion</i>	<i>Fitted</i>
$\text{O}^{2-}\cdots\text{O}^{2-}$	9547.960	0.2192	32.0	-2.04	6.3	¹¹⁷

<i>Crystal Structure</i>			
<i>Lattice Constant</i>	<i>Experimental (Å)⁸³</i>	<i>Calculated (Å)</i>	<i>% Difference</i>
<i>a</i>	9.4123	9.4697	0.61
<i>c</i>	3.1926	3.1466	-1.44
$\alpha \beta \gamma$	$90^\circ, 90^\circ, 120^\circ$	$90^\circ, 90^\circ, 120^\circ$	0

Here it can be seen that the quality of fit is not as good as seen in the earlier sections, but it is still within the overall permissible difference of 3% and hence it was used to perform defect calculations discussed in detail in Chapter 4.

3.5 Summary

This chapter has discussed the fitting methodology employed to derive pairwise potentials for two novel compounds, namely, FeSb_2O_4 and $\text{Ca}_5\text{IrO}_{12}$. A grid search method was employed to derive these values by systematically varying the potential parameters A, ρ and C till a good agreement with the crystallographic data was achieved. The quality of the fit resulting from each solution set was determined using the least square method with equal weight assigned to each lattice constant. The key aspects and findings of this chapter were:

- The use of an additional repulsive Cation-Cation potential to model crystal structures that contain ions with lone or pair of electrons. Islam *et al.*¹³ employed this methodology, to accurately model compounds with Bi^{3+} and Pb^{2+} lone pair of electrons.
- This methodology was then tested and successfully used to derive sufficiently good quality potentials for Sb_2O_3 . Owing to the lack of availability of mechanical properties and di-electric properties, the robustness of the methodology and the derived potential set was checked by their ability to work well with vacancies in the system.
- The derived Sb-Sb, Sb-O and O-O potentials from Sb_2O_3 and a suitable Fe-O interaction were employed to reproduce the crystal structure of FeSb_2O_4 . The potentials were then refined to improve the agreement with the crystallographic data. It was observed that when the short-range potential parameter c for O-O interaction was set to a value higher than 250, then resulting potential sets were successfully able to result in a geometry-optimised structure even with point defects like oxygen vacancies. This was used as a criterion for testing the robustness of the pair potentials, as there were no other physical properties to fit the potentials to. The

difference between the observed and predicted unit cell parameters and bond lengths suggested that the final set of potentials were able to reproduce the complex crystal structure with a 0.010 Å of discrepancy with the observed structure.

- These potentials were also able to successfully model a range of other phases belonging to the Schafarzikite family with an average difference of -2.5%.
- The same procedure was employed to derive Ir-O potential to model $\text{Ca}_5\text{Ir}_3\text{O}_{12}$. The potential was derived to fit a similar compound: NaIrO_3 . There were two reasons for doing that, firstly these potentials will be used to substitute Na onto the Ca site and secondly the oxidation of *Ir* ion from +4.67 to +5 when the substitution takes place.
- Due to the lack of any reported mechanical and dielectric properties, these potentials were employed to perform defect calculations to check their robustness.

3.6 Future Work

- The fitting methodology described in this chapter is very simple yet time-consuming. Efficient searching and optimisation procedures like the Reverse Monte Carlo approach, genetic algorithm and glow-worm algorithm could be employed to produce better quality potentials.
- The potentials could be fit to other experimental data such as the elastic constants, bulk modulus and dielectric constant when the data becomes available. Modifications could be made to fit the potentials to multiple phases simultaneously.

Chapter 4: Defect Chemistry, Dopant Substitution and

Anion insertion in FeSb₂O₄

4.1 Introduction

The structure of Schafarzikite or FeSb_2O_4 (illustrated in *figure 4.1*) consists of rutile-like chains of edge-shared transition metal FeO_6 octahedra along [001]. These chains are linked together by a second larger cation, Sb^{3+} which is bonded to three oxygen ions in a trigonal pyramidal geometry with a pair unbonded electron, SbO_3e^- . These stereochemically active lone pair of electrons are directed into the one-dimensional channels present along the *c-axis* and run parallel to the chains of the FeO_6 octahedra. This material has recently attracted a considerable amount of attention owing to these one-dimensional structural characteristics and the display of a high degree of compositional flexibility due to the presence of two cation sites. As outlined in *Chapter 1*, the majority of the work undertaken is experimental and has concerned the magnetic and electrical properties^{9,38,40–42,119} and the chemical reactivity^{39,42} associated with the compound's unique structure.

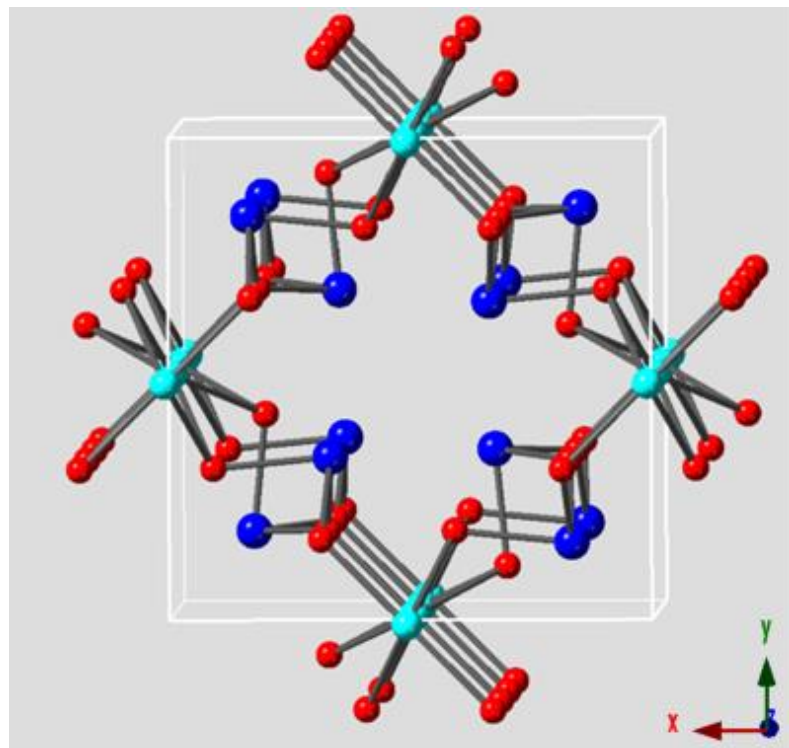


Figure 4.1 Predicted structure of FeSb_2O_4 viewed along [110]; the dark blue spheres represent Sb ions, red represents O ions and light blue spheres represent Fe ions

The one-dimensional channels with channel walls formed by cations is a unique feature of Schafarzikite. Most oxide materials with empty channels have channel walls made up of oxygen ions. These empty channels have been known to act as sites for cation insertion in oxide materials.⁴⁷ Anticipating a similar chemical activity with anion insertion in Schafarzikites, de Laune *et al.*⁴⁷ recently demonstrated the first-ever successful example of oxygen and fluorine insertion into these channels in FeSb₂O₄. Both the oxygen and fluorine excess phases were reported to occur at low temperatures, with different oxidation mechanism and bonding environments.

Materials with partially filled oxide ion sites have gained interest in research in energy materials as they provide an alternate conduction mechanism driven by interstitial ion migration as opposed to the vacancy driven mechanism. The rapid insertion reaction of oxygen observed at ~350°C in the channels suggests high oxygen ion mobility and conduction through interstitial oxygen ion migration.⁴⁷ This unique feature coupled with the range of isovalent and aliovalent cationic substitution that can occur at the sites M and X has opened avenues for further research on these materials.

Despite the recent advancement of research on these materials, there is still limited information regarding the defect behaviour and ion transport properties at the atomistic level. The structural information available for the oxygen and fluorine excess phases, are average values calculated using experimental techniques and lacks a detailed, in-depth understanding of the bonding environments, bond-lengths and the coordination of the O²⁻ ions and F⁻ interstitials. Owing to the similarity between the two ions, the possibility of an exchange between oxygen ions from the lattice with the fluorine ions in the channels is another phenomenon which is cannot be determined experimentally; whether the fluorine ions bond with Sb³⁺ ions in the channel or they substitute an oxygen ion in the FeO₆ octahedra instead. Thus, there is a need to investigate these reactions in detail using advanced computer simulation techniques.

To the best of our knowledge, this is the first investigation of the complex FeSb_2O_4 system using advanced atomistic modelling techniques. The aim of the current study is to address this lack of understanding of the energetics, the bonding mechanism and the coordination environment of these anions (O^{2-} and F^-) inserted in the one-dimensional channels of Schafarzikite. Defect chemistry and energetics of dopant substitution on the two cation sites, M and X, were also examined to predict the most favourable dopant species and the changes in the structural properties of the system as a function of the size and amount of the dopants. This study was performed in conjunction with the experimental studies and it will act as a means to further the knowledge about these new class of functional materials.

This chapter will first examine the intrinsic defect behaviour of the system using the pair potentials derived in chapter 3. Then the effect of dopant substitution will be examined and finally, the energetics and defect chemistry of the anion insertion will be investigated.

4.2 Intrinsic Defects

The previous chapter described the method for deriving pair potentials to model $FeSb_2O_4$ in pure and defected form. The final set of pair potentials employed in this chapter to perform all the defect calculations are summarised in table 4.1.

Table 4.1 Summary of the pair-wise potentials fitted for $FeSb_2O_4$

<i>Final Short-Range Potential Parameters</i>						
<i>Short Range Parameters</i>				<i>Shell Model</i>		
<i>Interaction</i>	<i>A(eV)</i>	<i>ρ (Å)</i>	<i>C (eV/Å⁶)</i>	<i>Y(e)</i>	<i>k (eV/Å²)</i>	<i>Ref.</i>
$Fe^{2+}\cdots Fe^{2+}$	1230	0.325	0.00	2.997	62.9	<i>Fitted</i>
$Sb^{3+}\cdots Sb^{3+}$	18100	0.3330	0.00	-5.51	359.55	<i>Fitted</i>
$Sb^{3+}\cdots O^{2-}$	9100	0.2787	0.00	-5.51	359.55	<i>Fitted</i>
$O^{2-}\cdots O^{2-}$	27299	0.24387	300	-2.04	6.3	<i>Fitted</i>

Most of the work in the previous chapter was concerned with pure systems; however, all systems have intrinsic above the absolute zero temperature. Hence, the defect calculations were initially performed on the energies of isolated point defects (vacancies and interstitials). The ions surrounding the defect in both cases were allowed to relax in the energy minimisation procedure. For vacancies, the defect energy corresponds to the energy required to remove a lattice ion from the crystal

to infinity; similarly, the energy required to introduce an ion from infinity into the lattice is the interstitial energy.

The procedure to model the point defects followed the two-region approach described in chapter 2. The radius of region I was selected to be 11 Å (corresponding to approximately 750 ions) and that of region II was 22 Å. The results are listed in table 4.2 and the energy of each non-equivalent vacancy site for O; O1-apical site and O2-equatorial site, is given.

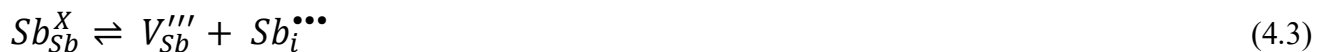
Table 4.2 Summary of the calculated energies of isolated point defects in FeSb₂O₄

Defect	Position	Calculated Defect Energy (eV) (per defect)
Fe vacancy (V_{Fe}'')	(0.0, 0.5, 0.25)	22.10
O1 vacancy ($V_{\text{O1}}^{\bullet\bullet}$)	(0.678, 0.178, 0.25)	17.80
O2 vacancy ($V_{\text{O2}}^{\bullet\bullet}$)	(0.093, 0.683, 0.00)	19.00
Sb vacancy (V_{Sb}''')	(0.159, 0.150, 0.00)	41.31
Sb interstitial ($\text{Sb}_i^{\bullet\bullet\bullet}$)	(0.725, 0.523, 0.903)	-32.36
O interstitial (O_i'')	(0.5, 0.5, 0.5)	-16.42
O interstitial (O_i'') (channel)	(0.517, 0.457, 0.854)	-20.49

Initial calculations suggest that the formation of vacancies is unfavourable owing to high positive defect energy values associated with each defect; the most favourable defect is the Sb³⁺ interstitial as it has the lowest defect energy. The individual vacancy energies suggest that it is more favourable to form oxygen vacancies in the apical region (O1) as compared to the equatorial region (O2). The iron interstitial failed to converge at the energy minimisation stage. This could be resulting from the interaction between the iron ions with the other lattice ions. Finding suitable interstitial sites for antimony and oxygen also needed some amount of probing to determine the lowest energy sites. The lowest energy interstitial sites for O²⁻ and Sb³⁺ ions are listed in *table 4.2*. Most of the interstitial sites were located across the length and breadth of the one-dimensional channels, it was observed that the interstitial oxygen ions could occupy a number of sites within the channel, the defect formation energy associated with all these sites was approximately -20 eV. This further suggests that the channels have favourable sites for oxygen insertion. This phenomenon will be discussed in detail in *section 4.4*.

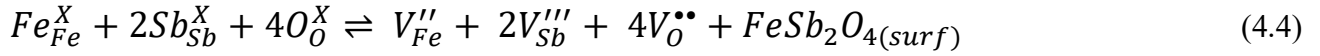
4.2.1 Schottky and Frenkel Defects

Point defects do not occur in isolation and often tend to combine to form defect clusters. The lowest energy isolated point defects were therefore combined to give formation energies for the Frenkel pairs and Schottky defects. The Frenkel defects can be represented by the following reactions using the Kröger-Vink notation¹²⁰.



Similarly, the Schottky defects can be represented by the *equation 4.4*, two other pseudo-Schottky defects that are possible are FeO and Sb₂O₃, represented by *equations 4.5* and *4.6*. The lattice

energies for FeO and Sb₂O₃ (-39.13 eV and -132.85 eV, respectively) were calculated from the pair potentials derived in this study using known structures of FeO and Sb₂O₃.^{121,122}



The values of Frenkel and Schottky defects were calculated by combining the energies of individual point defects and the lattice energies using *equation 4.1 to 4.6*. *Table 4.3* summarises the defect energy values calculated using this method.

Table 4.3 Summary of Unbound Defect Clusters

Defect	Total Energy (eV)	Energy (per defect eV)
O1 Frenkel (O1FP)	1.38	0.69
O2 Frenkel (O2FP)	2.58	1.29
Sb Frenkel (SbFP)	8.95	4.48
Schottky Trio (SchT)	4.68	0.67
Sb₂O₃ Schottky (Sb₂O₃-Sch)	9.48	1.35
FeO Schottky (FeO-Sch)	1.97	0.98

The initial Schottky and Frenkel defect calculations suggest that the formation of oxygen Frenkel pairs and FeO Schottky are more favourable energetically and antimony Frenkel pairs are the most unfavourable as it has the highest formation energy. Oxygen Frenkel and the Schottky trio have a similar per defect. However, the formation energy of Schottky trio is almost 4 times that of oxygen Frenkel pairs.

The defect energies are calculated by summing up individual point defect energy, assuming infinite dilution and does not specify the defect positions with relation to each other. Thus, to further investigate the defect behaviour, bound defects clusters were simulated, wherein more than one type of defect was added to the system simultaneously. Then the binding energy was calculated by calculating the difference between the defect energy values of bound defects and unbound defects at infinite dilution. The defect formation energies of the bound defects and the corresponding binding energies are summarised in *table 4.4*.

Table 4.4 Summary of Bound Defect Clusters

Defect Type	Vacancy	Interstitial	Defect Energy (eV)	Binding energy (eV)
O1FP	0.679, 0.179, 0.25	0.5 0.5 0.5	-2.95	-1.57
O2FP	0.093, 0.683, 0.00	0.5, 0.5, 0.5	1.85	0.73
Defect Type	Vacancy (Fe)	Vacancy (O)	Defect Energy (eV)	Binding energy (eV)
FeO Sch	0.0, 0.5, 0.25	0.595, 0.816, 0.0	39.04	37.12

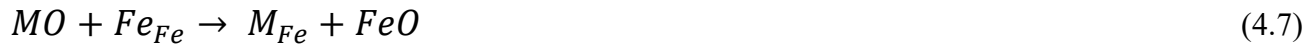
From *table 4.4*, it is evident that O1 Frenkel pairs are energetically the most favourable type of defect and *FeO* Schottky like defects are least favourable. Though the defect energy values unbound defects from *table 4.3* suggest that *Sb₂O₃* Schottky defects and Sb Frenkel are energetically favourable, however, due to the high number of defects in the Schottky, the system becomes unstable and fails to converge. The same phenomenon is also observed for the Schottky trio. For Sb Frenkel pairs, the antimony ion migrates back to its vacancy site during the recombination process.

To conclude, when isolated defect energy values were combined to calculate the formation energy for Frenkel and Schottky cluster in unbound condition, the oxygen Frenkel pairs and FeO Schottky have lowest formation energy and hence could be expected to be preferred mode of the intrinsic defects. To investigate this further, these defect clusters were simulated in bound conditions by simulating a combination of vacancies and interstitials within the same configuration. On examining the defect energies for bound defects, it became evident that for any given temperature, oxygen Frenkel pairs will be the most common type of defects found in the system.

4.3 Dopant Substitution

Following on from the initial intrinsic defect calculations, the energetics of extrinsic defect were calculated. As outlined in *Chapter 1*, Schafarzikite displays a high degree of compositional flexibility. Isovalent substitutions by a variety of transition metals at site M and aliovalent substitution by Pb²⁺ at site X have been reported so far. These substitutions resulted in changes in the magnetic and electric properties of Schafarzikite. The link between the structural composition and magnetic interplay has been studied extensively and is now well understood. However, the energetics of these substitutions and the resulting structural changes need to be examined in depth to determine energetically favourable dopant cations for this system. The dopants/substitution cations were introduced as impurities in the system.

For site M, all substitutions are isovalent in nature and hence no charge compensation mechanism was needed. The solution energy for these substitutions was calculated by using *equation 4.7* and *4.8*.



$$E_{sol} = -E_{latt}(MO) + E_{sub}M_{Fe} + E_{latt}(FeO) \quad (4.8)$$

Here MO is the oxide of the dopant ion M, where M is Mg, Mn, Co and Ni^{53,55,123}. The lattice energies for MO were calculated by using published pair potentials for M-O interaction and the fitted potential for O-O interaction. The lattice energy for FeO was same as that used in Schottky defect calculation. The substitution and solution energy calculated by this approach is summarised in *table 4.5* and *figure 4.2* plots the solution energy as a function of the ionic radius.

Table 4.5 Summary of Isovalent Substitutions on Fe Site

Dopant	Charge	Ionic Radius (\AA) ⁴⁶	Substitution Energy (eV)	Solution Energy (eV)
Mg	+2	0.72	-4.69	-0.42
Mn	+2	0.83	-1.18	0.2
Co	+2	0.75	-3.30	0.5
Ni	+2	0.69	-3.78	0.9

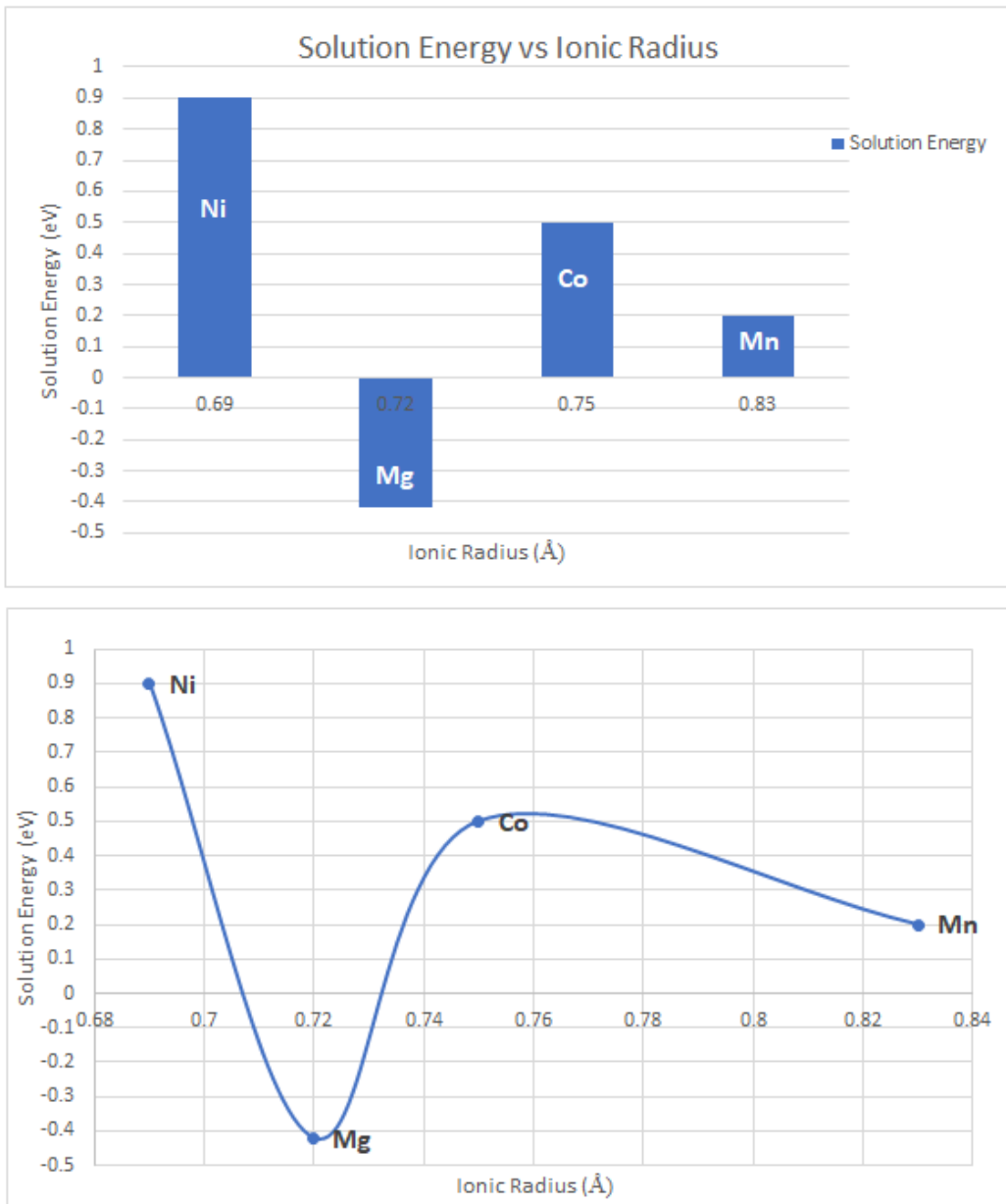
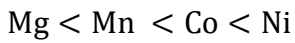


Figure 4.2 An illustration of a graph of solution energy plotted as a function of ionic radius of M^{2+} ions

The solution energies of all the transition metal ion substitutions are relatively large as compared to Mg. It can be observed that Mg is the most favourable dopant as it has the lowest solution energy. For the transition metal ions, the solution energy decreases as the ionic radius increases. The ions can be ranked according to their solution energies in ascending order.



The above finding is in accordance with the experimental data as the most commonly used dopant on the Fe site is Mg.¹²³ Moreover, an Mg variant of Schafarzikite, MgSb₂O₄, with similar structural properties exists as a solid solution. The other most commonly used dopants are Mn and Co⁴¹. These three dopants have been employed to investigate the oxygen and fluorine excess phases, which are discussed in the next section.

A similar approach was employed to calculate the solution energy for aliovalent and isovalent substitution on site X. The two reported dopants on the Sb site are Pb²⁺ and Bi³⁺^{9,39}. The Bi³⁺ substitution at Sb³⁺ failed to converge and resulted in very high substitution energy. This has also been demonstrated experimentally as there have not been any reports of a phase with complete substitution of Bi³⁺ at Sb³⁺ site and that could be the reason for the structure's failure to converge at the geometry optimisation stage.

The substitution of divalent Pb²⁺ ions onto Sb³⁺ site results in an overall increase in the negative charge of the crystal. Hence, to compensate for this charge imbalance two schemes were adopted. In *scheme 1*, an oxygen vacancy was created to achieve the charge neutrality. The solution energy for this substitution reaction was calculated through *equations 4.9 and 4.10*. The lowest defect energy value for the creation of an oxygen vacancy calculated in the previous section was used in *equation 4.9*. The lattice energy for PbO and Sb₂O₃ was calculated using the Pb-O, Sb-O, Sb-Sb and O-O potentials derived in *Chapter 3* for known structures^{106,124}.

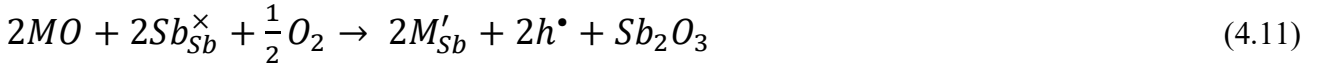
- For M=Pb²⁺; *Scheme 1: formation of Oxygen Vacancies*



$$E_{sol} = -E_{latt}(MO) + E_{sub}M_{Sb} + \frac{1}{2}V_O^{..} + \frac{1}{2}E_{latt}(Sb_2O_3) \quad (4.10)$$

In *scheme 2*, the increase in the negative charge was compensated by the oxidation of Fe^{2+} to Fe^{3+} through the creation of a positively charged hole. The solution energy for this substitution mechanism was calculated by using *equations 4.11-4.13*.

- For $M=\text{Pb}^{2+}$; *Scheme 2: formation of electron interstitial and oxidation of Fe^{2+} to Fe^{3+}*



$$2E_{sol} = -2E_{latt}(MO) - \frac{1}{2}E_{latt}O_2 + 2E_{sub}(M_{Sb}) + E_{latt}(Sb_2O_3) + 2h^{\bullet} \quad (4.12)$$

The mechanism used to simulate the creation of a positively charged hole was a combined process. First, the energy for removing an Fe^{2+} ion from its lattice to infinity was calculated and then the energy for introducing the subsequent Fe^{3+} ion into the vacant position from infinity was calculated. In GULP, this was achieved was using the impurity keyword. As the routines encoded in GULP do not take into account the ionisation energies involved in the process of hole formation. Thus, the total hole formation energy was calculated by summing up the total defect energy for introducing Fe^{3+} impurity and the 3rd ionisation energy for Fe^{125} . In this calculation, it was assumed that the ionisation energy within the crystal lattice was equal to the gas phase reaction.

$$V''_{Fe} + Fe_i^{\bullet\bullet} = -37.704 \text{ eV} \quad (4.13)$$

$$3rd \text{ Ionisation Energy (I.E) of } Fe = +30.652 \text{ eV} \quad (4.14)$$

$$\text{Total Hole formation Energy} = 3^{rd} \text{ I.E of } Fe + V''_{Fe} + Fe_i^{\bullet\bullet} = -7.054 \quad (4.15)$$

$$\frac{1}{2}O_2 \rightarrow E_{DE}(O) + E.A(O^-) + E.A(O^{2-}) = \frac{1}{2}(5.15 - 1.47 + 5.16) = 12.43 \quad (4.16)$$

Similarly, the dissociation energy of an oxygen molecule given in *equation 4.11* and *4.12* was calculated by adding the energy taken to break the O_2 molecule and the first and second Electron

affinity of oxygen. This calculation is summarised in *equation 4.16*. The solution energies calculated using both *scheme 1* and *2* are summarised in the *table 4.6*.

Table 4.6 Solution energies for Pb^{2+} substitution on Sb^{3+} site

Dopant	Charge	Substitution Energy (eV)	Solution Energy (eV)
Pb^{2+} Scheme 1	+2	23.13	-1.85
Pb^{2+} Scheme 2	+2	23.13	-20.9

The energy for substituting an Sb^{3+} ion in the crystal lattice with Pb^{2+} ion is high for both the scheme. However, on combining the substitution energy with the energy of the respective charge compensation mechanism adopted in each scheme, the solution energy calculated for both the schemes was low. As summarised in the *table 4.6*, it is clear that scheme 2 is more favourable than scheme 1, as it has the lowest solution energy. This has been observed experimentally as well; the substitution of Pb^{2+} at Sb^{3+} was charge compensated by the oxidation of some Fe^{2+} to Fe^{3+} ^{9,47}. This is one of the charge compensation mechanisms responsible for the incorporation of excess anions in the structure. The next section will examine the anion excess phases and the relevant charge compensation mechanisms responsible involved.

4.4 Oxygen insertion

As outlined in Chapter 1, and in the introduction of this chapter, the one-dimensional channels with the channel walls formed by cations- Sb^{3+} , is a unique feature of Schafarzikite, which facilitates the insertion of anions within these channels. The study by De Laune *et al*^{44,47} presented the first example of a successful attempt of insertion of oxygen ions within the structural channels by heating

selected phases of Schafarzikite oxygen-rich atmosphere in at 600 to 750 °C. Among these phases, the system with the highest content of Fe²⁺ions (FeSb_{1.25}Pb_{0.75}O_{4+y}) had the highest amount of oxygen intake (approximately 2%) at 350 °C. Initially, it was expected that the oxidation of 2Fe²⁺ to 2Fe³⁺ was the only charge mechanism responsible for the insertion of an extra O²⁻ ion entering the channels. However, the TGA (Thermogravimetric analysis) data of the oxidised products reported twice, FeSb_{1.25}Pb_{0.75}O_{4.29}, as much oxygen uptake as expected from the complete oxidation of Fe²⁺. On further investigation, Mossbauer spectra revealed an additional cation Sb³⁺ was being oxidised to Sb⁵⁺ to balance the charge associated with the extra oxygen content. Thus, it was concluded that both Fe²⁺ and Sb³⁺ simultaneously oxidise to Fe³⁺ and Sb⁵⁺ to facilitate the oxygen insertion in the channels.

To determine the structural distribution of ions around the O²⁻ interstitials, the local environment of the oxygen interstitials- the O₃ site was examined in more detail. Based on the average atomic positions obtained by NPD data, the average Sb/Pb – O and Fe-O bond-lengths and the distance between the two oxygen interstitials (O₃-O₃), the formation of a defect cluster was proposed. This defect cluster was suggested to comprise of two O²⁻ interstitials, two 4-coordinate Sb³⁺ ions and one, 5-coordinate Sb⁵⁺ ion. The reported average Sb/Pb-O and Fe-O bond lengths are summarised in *table 4.7*

Table 4.7 Reported Bond distances for Oxygen Excess Phase- FeSb_{1.25}Pb_{0.75}O_{4.29}⁴⁷

Bonds	Bond-Lengths(Å)
Fe-O1	2.023 [$\times 2$]
Fe-O2	2.029 [$\times 4$]
Sb/Pb-O1	2.108
Sb/Pb-O2	2.095
Sb/Pb-O3	2.30
Sb⁵⁺-O3	1.91
O3-O3	1.54

It is worth noting that the bond-distances summarised in *table 4.7*, corresponds to an average value of all the bonds and the proposed configuration of the defect cluster is also an average estimate of the spatial arrangement of all the ions around the oxygen interstitials. Hence, computer simulation tools were used to provide in-depth knowledge of the structure of the defect cluster formed by the oxygen interstitials in the one-dimensional channels.

4.4.1 Initialising the defect cluster computationally

Owing to the high concentration of defects associated with the oxygen insertion reaction, the supercell method was employed to model the oxygen excess phase with the proposed defect cluster. To reduce the complexity of achieving a random distribution of Pb²⁺ ions and Sb³⁺ ions at site X, all the defect calculations were performed on a 2×2×2 supercell of FeSb₂O₄. The proposed defect cluster by de Laune *et al*⁴⁷ was used as a reference for constructing a system with the oxygen interstitials. Two O²⁻ were placed in the channels (O3 sites) in between three Sb³⁺ ions. One of the three Sb³⁺ was changed to Sb⁵⁺ ion and two of the nearest Fe²⁺ ions were changed to Fe³⁺ ions. The pair potentials

used for Sb⁵⁺- O²⁻ and Fe³⁺ - O²⁻ interaction were chosen from the set of derived parameters.^{117 126}; the values are summarised in *table 4.8*. The rest of the pairwise potentials were the same that were derived in this study (given in *table 4.1*)

Table 4.9 Short Range potentials

Short Range Parameters				Shell Model		
Interaction	A(eV)	ρ (\AA)	C (eV/ \AA^6)	Y(e)	k (eV/ \AA^2)	Ref.
Sb⁵⁺...O²⁺	18752.220	0.2219	0.00	2.895	101.2	¹¹⁷
Fe³⁺...O²⁻	3219.335	0.2641	0.00	3.00	N/A	¹²⁶

4.4.2 Results and analysis

The final energy of the oxygen excess $FeSb_2O_4$ is predicted (-178.23 eV) to be less than the energy of the pure system (-171.24 eV). Thus, signifying that insertion reaction is energetically favourable and the predicted crystal configuration refers to a stable, low energy configuration. The initial fractional positions of the oxygen interstitial, Sb⁵⁺ ion, the two 4-coordinate Sb³⁺ ions close to the oxygen interstitial and Fe³⁺ ions are summarised in *table 4.12*. *Figure 4.3* gives the starting unrelaxed structure of the defect cluster before geometry optimisation.

As seen in *figure 4.3*, the O²⁻ (O3) interstitials were placed in between two Sb³⁺ (ions labelled as 1, 2) and one Sb⁵⁺ (ion labelled as 4). The average bond distance between O3 and Sb1, Sb2 was kept as 2.063 \AA and between O3 and Sb4 was kept as 2.033 \AA . The system was allowed to achieve a geometry-optimised state without any symmetry constraints and the core and shells were allowed to relax independently. The predicted values of lattice parameters, the atomic position of oxygen interstitials and the position of the Sb³⁺ and Sb⁵⁺ ions around the oxygen ions are summarised in *table*

4.11. The initial and final atomic positions of Sb ions and O interstitials are summarized in *table 4.12*.

The final values of the predicted Sb³⁺/Sb⁵⁺-O₃ bond lengths are summarised in *table 4.13*

Table 4.11 Summary of the initial and final lattice parameters of the oxygen excess phase.

Lattice parameters	Initial value (Å)	Final value (Å)	Difference (Å)	% Difference
a	8.62	8.62	0.00	0.00
b	8.62	8.14	-0.48	-5.6
c	5.93	6.32	0.39	6.57
α	90 °	90.64°	0.64°	0.71
β	90 °	90.12°	0.12°	0.13
γ	90 °	90.36°	0.36°	0.40

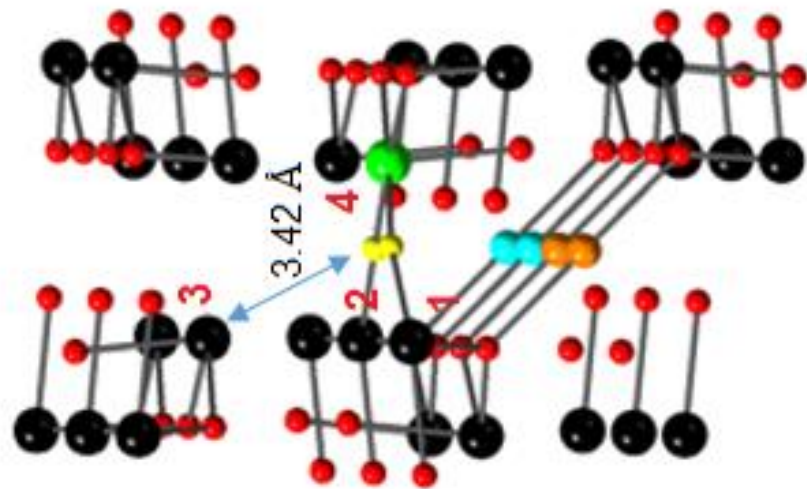


Figure 4.3 (a) Illustration of the $2 \times 2 \times 2$ supercell. The yellow spheres represent the oxygen interstitial; (b) A zoomed-in view of the ions around the O₃ ions; The green sphere represents Sb⁵⁺ ions, black sphere Sb³⁺ ions, orange sphere- Fe³⁺ ions, blue sphere-Fe²⁺ ions and red sphere – O₁ and O₂. The ions labelled 1 to 4 are the cations around O₃.

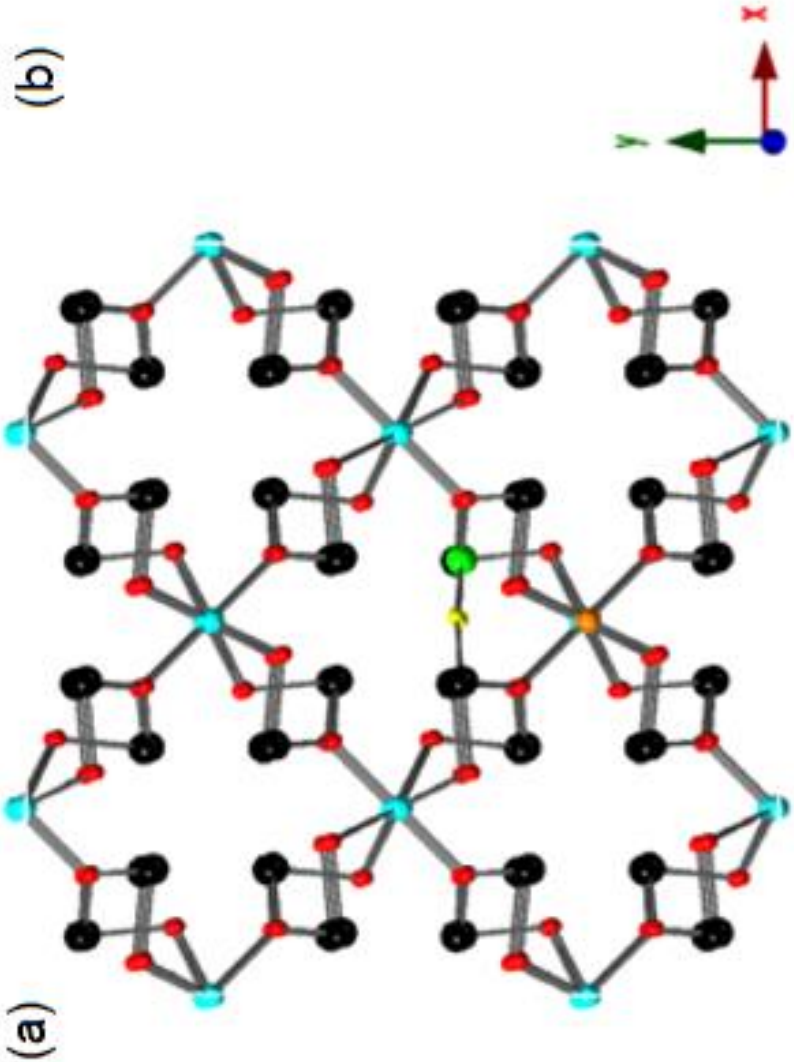


Table 4.12 Summary of the initial and final position the defect cluster ions

<i>Species</i>		<i>Initial Position(Å)</i>	<i>Final Position(Å)</i>	<i>Difference(Å)</i>
O_{int1}(O3)	<i>x</i>	8.637	8.914	0.276
	<i>y</i>	7.206	7.403	0.197
	<i>z</i>	7.364	7.800	0.436
O_{int2}(O3)	<i>x</i>	8.689	8.914	0.225
	<i>y</i>	7.361	7.436	0.074
	<i>z</i>	10.435	10.127	-0.308
Sb⁵⁺ (Sb4)	<i>x</i>	9.999	10.087	0.087
	<i>y</i>	7.189	6.703	-0.485
	<i>z</i>	8.894	9.482	0.588
Sb³⁺ (Sb1)	<i>x</i>	7.189	7.345	0.156
	<i>y</i>	7.223	6.427	-0.796
	<i>z</i>	11.859	12.453	0.594
Sb³⁺ (Sb2)	<i>x</i>	7.189	7.483	0.294
	<i>y</i>	7.224	6.557	-0.666
	<i>z</i>	5.929	6.498	0.569
Sb³⁺ (Sb3)	<i>x</i>	7.223	7.483	0.259
	<i>y</i>	10.051	8.803	-1.248
	<i>z</i>	8.894	9.507	0.613

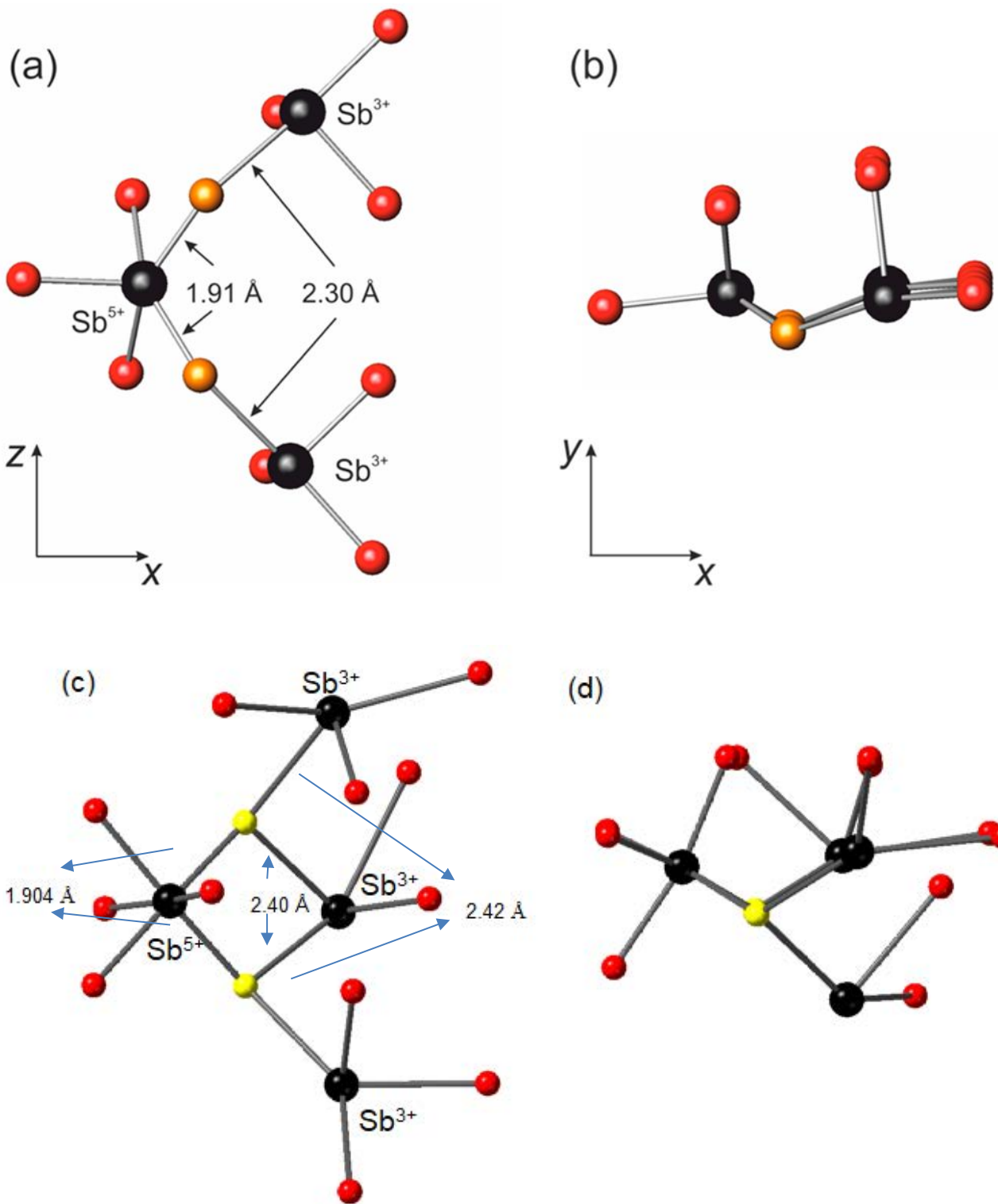


Figure 4.4 (a) & (b) The representation of the proposed defect cluster with O₃ interstitials viewed along [101] and [110] respectively. (c) & (d) representation of the predicted defect cluster with O₃ interstitials viewed along [101] and [110] respectively. The black spheres are the Sb ions, the yellow spheres are the O₃ interstitials. The corresponding bond distance is given in the structure

Table 4.13 Summary of the predicted individual Sb-O bond distances compared with the reported values

Bonds	Bond Distances (\AA)		Difference (\AA)
	Calculated	Experimental	
Sb³⁺			
Sb1-O1	1.979	2.108	-0.129
Sb1-O2 [×2]	2.349, 2.505	2.095	0.255, 0.41
Sb1-O3	2.50	2.30	0.20
Sb2-O1	2.065	2.108	-0.043
Sb2-O2 [×2]	2.298, 2.465	2.095	0.203, 0.37
Sb2-O3	2.36	2.30	0.06
Sb3-O1	2.490	2.108	0.382
Sb3-O2	2.346	2.095	0.251
Sb3-O3 [×2]	2.380, 2.412	2.30	0.08, 0.112
Sb⁵⁺			
Sb4-O1 [×2]	1.907, 1.908	1.91	-0.04, -0.03
Sb4-O2 [×2]	1.891, 1.932	1.91	-0.019, 0.021
Sb4-O3 [×2]	1.903, 1.905	1.91	-0.08, -0.06

4.4.1 Discussion

The predicted lattice parameters summarised in *table 4.11* suggest that the structure has transformed from a tetragonal to an orthorhombic system. This could be a result of geometry optimising the system without any symmetry constraints. The lattice parameter b has contracted as a result of the replacement of the large Fe^{2+} ions by smaller Fe^{3+} ions and hence a decrease in the size of the octahedral sites. The lattice parameter c on the other has expanded due to the increased interchain Fe-Fe repulsion (Fe-Fe distance increased to 3.154 Å from 2.965 Å) along [001]. The oxygen interstitials (O_3), their neighbouring Sb^{3+} ions and Sb^{5+} ions have moved from their original initial positions to form a defect cluster. From *table 4.12*, it can be observed that the difference between the initial and final atomic positions of the ion species forming the defect cluster is significant. Among all the ion species, the largest observed difference is for a 4-coordinate Sb^{3+} ($\text{Sb}3$) ion, which has moved approximately 1.4 Å (RMS value in *-y direction*) from its initial position.

This finding is illustrated in *figure 4.4*, where, in addition to the two 4-coordinate Sb^{3+} ions and one 5-coordinate Sb^{5+} ion as proposed experimentally⁴⁷, the predicted defect cluster comprises of an additional 4-coordinate Sb^{3+} ($\text{Sb}3$) ion bonded to both the oxygen interstitial ions. This additional Sb^{3+} cation was approximately 3.42 Å far from the O^{2-} interstitials as seen in *figure 4.3*. This separation falls within the short-range potential cut-off of 12 Å. Thus during geometry optimisation, this additional ion would have experienced a combination of attractive long and short-range forces resulting in this large shift. In addition to the $\text{Sb}3$ ion, the average difference between the initial and final positions of the two O^{2-} interstitials is approximately 0.4 Å (RMS value in *+y direction*). This combined shift results in an average separation of 2.40 Å between the additional Sb^{3+} ion and the two O^{2-} interstitials ions.

From *figure 4.4 and table 4.13*, it can also be seen that this additional cation results in slight elongation of Sb1-O3 and Sb2-O3 bonds (2.50 Å and 2.36 Å, respectively). The difference between the calculated bond-distance between Sb3 and O3 (2.40 Å) and the reported Sb-O3 bond distance (2.30 Å) is equivalent to approximately 0.1 Å. All the three Sb³⁺ ions assume a trigonal-bipyramidal spatial orientation with the lone pair of electrons oriented along with the equatorial position.

The final interesting development in the predicted structure is the change in coordination of the Sb⁵⁺ ion, from 5 to 6 assuming an octahedral geometry, which is the preferred coordination for Sb⁵⁺. The 6-coordinate Sb⁵⁺ octahedra consist of, two Sb4-O3 bonds, two Sb4-O1 bonds and two Sb4-O2 bonds. An additional O1 ion from the lattice has moved closer to the Sb⁵⁺ ion forming the additional Sb4-O1 bond. The average Sb4-O3 bond-distance calculated is 1.908 Å, which is 0.002 Å smaller than the reported value (1.91 Å and 0.07 Å smaller than the mean bond length (1.977 Å)¹²⁷ for 6-coordinate Sb⁵⁺.

As summarised in *table 4.13*, though some of the Sb³⁺-O distances are larger than the experimental values, they are within the maximum Sb³⁺-O bond length (mean value: 2.092 Å and maximum value: 2.596 Å)¹²⁷ reported for a 4-coordinate Sb³⁺ ion. The Sb-O1 bonds have contracted slightly while the Sb-O2 bonds have elongated slightly. The highest amount of discrepancy is observed with the Sb3-O1 and Sb3-O2 bonds; this could be the result of the being close proximity to the O3 ions and spatially in between two other Sb³⁺ ions (Sb1 and 2). It is worth noting, that the ions around the oxygen interstitials are in the immediate surrounding of the crystal defects and tend to undergo distortions and hence the bond-distances differ slightly from the experimental values and the reported Sb-O bond-distances.⁴⁷

Thus, it can be concluded that the predicted defect cluster consists of three 4-coordinate Sb³⁺ (Sb1, Sb2, Sb3), two O²⁻ interstitials (O3) and one 6-coordinate Sb⁵⁺ (Sb4).

4.5 Fluorine Insertion

Owing to the success with oxygen insertion in a few selected phases of FeSb_2O_4 , De Laune *et al.*,⁵¹ extended the above-discussed study to examine the effects related to the fluorine insertion. Phases $\text{Mg}_{0.50}\text{Fe}_{0.50}\text{Sb}_2\text{O}_4$ and $\text{Co}_{0.50}\text{Fe}_{0.50}\text{Sb}_2\text{O}_4$ were seen to undergo topotactic fluorine insertion into the channels when heated at low temperature ($\sim 230^\circ\text{C}$) in 10% F_2 in nitrogen. This was followed by the oxidation of Fe^{2+} to Fe^{3+} as the main charge compensation mechanism to accommodate the extra fluorine ions. The structure of these phases was determined using Neutron Powder Diffraction (NPD), Mossbauer spectroscopy and Solid-State NMR techniques. The fluorine interstitials were located in the channels at sites which were closely related to oxygen interstitial sites found in the oxygen excess phases. Based on the average bond-distance values and the atomic positions determined by the above-mentioned techniques, it was observed that the fluorine ions entered the channels, and each formed a bridging bond with two Sb^{3+} ions located in the channel walls. It was also observed that these Sb-F bonds had slightly different lengths. An increase in the Sb-O bond length was also observed, owing to the increase in the coordination number of some Sb^{3+} ions, which were bonded to the interstitial fluorine. However, a detailed comparison of the Sb-O and Sb-F bond distances around the fluorine ions was not possible and the values obtained were average values of all the Sb-O bonds in the system.

Hence, computer simulation techniques were employed to model the insertion of fluorine ions in FeSb_2O_4 and obtain individual Sb-O and Sb-F bond distances. Computer simulation tools were also used to determine the possibility of the exchange of lattice oxygen by the interstitial fluorine ions as it is difficult to differentiate between O and F ions by XRD or NPD techniques.

4.5.1 Initialising the fluorine excess phase $\text{FeSb}_2\text{O}_4\text{F}_x$ computationally

Owing to the lack of availability of a means to ensure a random distribution of Mg/Fe ions, pure FeSb_2O_4 was used as the starting material for the insertion of excess fluorine in the channels. To obtain an in-depth knowledge of the localised environment around the excess fluorine ions, the

supercell method was used. A $2\times 2\times 2$ supercell of FeSb₂O₄ was constructed to model the excess fluorine in the system. Two fluorine ions placed in the channels in the same position as the oxygen interstitials. (*Table 4.12*) The average distance between the F⁻ ions and the adjacent Sb³⁺ ions were kept at 2.024 Å. Charge neutrality was maintained by oxidising/ replacing two Fe²⁺ ions near the F⁻ ions by Fe³⁺ ions. The system was then geometry optimised under no symmetry conditions to allow the ions to relax independently and to obtain an accurate structure of the F⁻ excess phase, especially around the fluorine interstitials. The pairwise potentials used describe the F-F and Sb-F interaction (outlined in Chapter 3) were derived to fit the structure of SbF₃¹¹⁵. These potentials were then employed to model the fluorine excess phase FeSb₂O₄F_x. This method was used to validate the potentials derived. The Fe³⁺-O potential used in modelling the oxygen excess phase was also used to model the fluorine excess phase. The Sb-F and F-F potentials are summarised in *table 4.14*. The starting structure, the initial bond lengths of Mg_{0.5}Fe_{0.5}Sb₂O₄ are summarised in *figure 4.5* and *table 4.15*, respectively.

Table 4.14 Derived Short-range potentials for F interaction

Short Range Parameters				Shell Model		
Interaction	A(eV)	ρ (Å)	C (eV/Å⁶)	Y(e)	k (eV/Å²)	Ref.
Sb³⁺···F	1200	0.33	0.0	-1.378	24.36	<i>Fitted</i>
F···F	2100	0.27	20	-1.378	N/A	<i>Fitted</i>

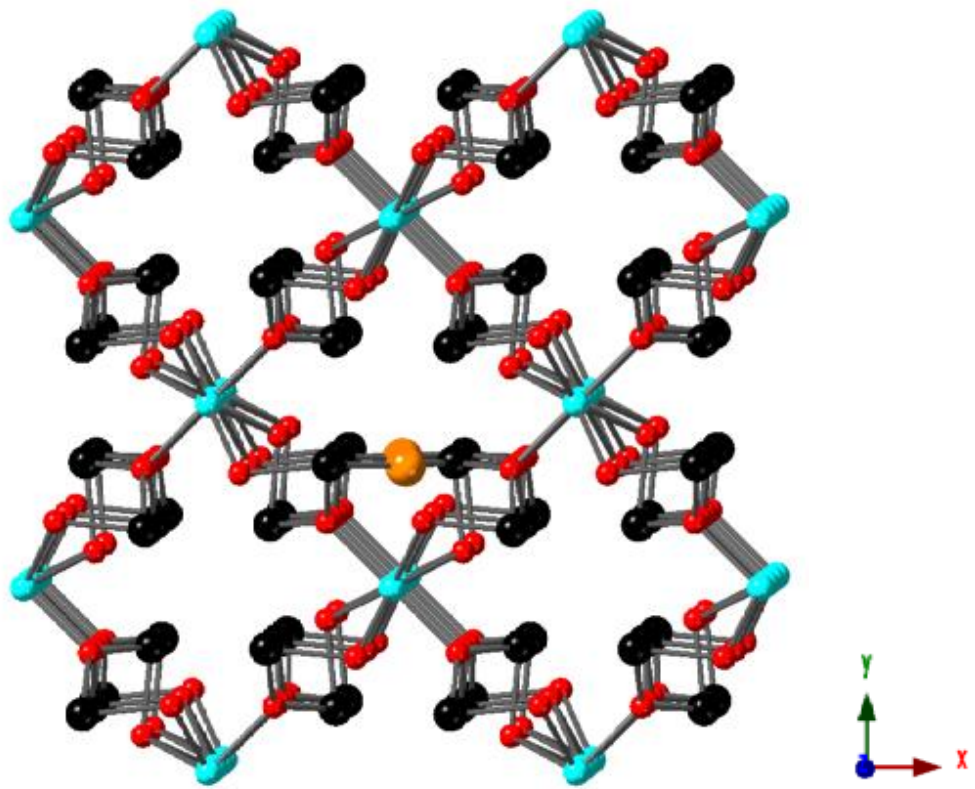


Figure 4.5 An illustration of the unrelaxed structure of the $2 \times 2 \times 2$ supercell with F interstitials (orange sphere)

view along [110]

Table 4.15 Summary of the initial lattice parameters and Bond distances in the FeSb₂O₄ supercell converted to unit cell parameters.

<i>Lattice parameters</i>	<i>2×2×2 Supercell (Å)</i>	<i>Unit Cell (Å)</i>
<i>a</i>	17.240	8.620
<i>c</i>	11.859	5.929
<i>α β γ</i>	90 °	90 °
Fe-O1	2.165	2.165
Fe-O2	2.318	2.318
Sb-O1	2.035	2.035
Sb-O2	2.10	2.10

4.5.2 Results and Analysis

The F excess phase was successful in achieving a geometry-optimised structure. The lattice energy associated with this system (-174.01 eV) was slightly higher than the O-excess phase (-178.23 eV). It was observed that as compared with the oxygen excess phase, the ions around the anion F⁻ have undergone lesser distortion. This was attributed to the reduced negative charge on F⁻ as compared to O²⁻, which resulted in reduced repulsion between the anions in channels. The predicted lattice parameters, initial and final position of the F⁻ ions and the Sb³⁺ions around them are summarised in *table 4.16. and 4.17*, respectively.

Table 4.16 Predicted lattice parameters compared with initial lattice parameters

Lattice parameters	Initial value (Å)	Final value (Å)	Difference (Å)	% Difference
a	8.620	8.730	0.11	1.27
b	8.620	8.283	-0.34	-3.94
c	5.929	6.100	0.17	2.89
α	90 °	89.72	-0.27	-0.31
β	90 °	85.07	-4.92	-5.57
γ	90 °	90.05	0.05	0.06

Table 4.17 Predicted ions positions around F interstitial compared with initial values.

<i>Species</i>		<i>Initial Position(Å)</i>	<i>Final Position(Å)</i>	<i>Difference(Å)</i>
<i>F_{int1}</i>	<i>x</i>	8.637	8.608	-0.030
	<i>y</i>	7.206	8.432	1.225
	<i>z</i>	7.364	7.552	0.187
<i>F_{int2}</i>	<i>x</i>	8.689	8.835	0.146
	<i>y</i>	7.361	8.465	1.103
	<i>z</i>	10.435	10.480	0.044
<i>Sb₁³⁺(F_{int1})</i>	<i>x</i>	7.189	7.455	0.266
	<i>y</i>	7.223	7.106	-0.117
	<i>z</i>	5.929	6.039	0.110
<i>Sb₂³⁺(F_{int1})</i>	<i>x</i>	7.223	7.316	0.092
	<i>y</i>	10.034	9.575	-0.459
	<i>z</i>	8.894	8.979	0.085
<i>Sb₁³⁺(F_{int2})</i>	<i>x</i>	10.010	10.266	0.257
	<i>y</i>	7.196	7.355	0.160
	<i>z</i>	8.894	8.918	0.024
<i>Sb₂³⁺(F_{int2})</i>	<i>x</i>	10.033	10.196	0.162
	<i>y</i>	9.999	9.939	-0.060
	<i>z</i>	11.858	11.992	0.134

The predicted system has transformed from tetragonal to orthorhombic. This could be attributed to the optimising the system without symmetry constraints. The increase in lattice constant c is a result of the increased interchain Fe-Fe repulsion due to the Fe^{3+} ions in the chain. However, the reason behind the increased lattice constant a is still a bit unclear. Lattice constant b has contracted as a result of the presence of smaller Fe^{3+} cations in the FeO_6 octahedra. The differences in the atomic positions of the Sb^{3+} ions are also significantly large. This was further investigated by visualising the system with the fluorine interstitials. The predicted structure with the fluorine interstitials is given in figure 4.6

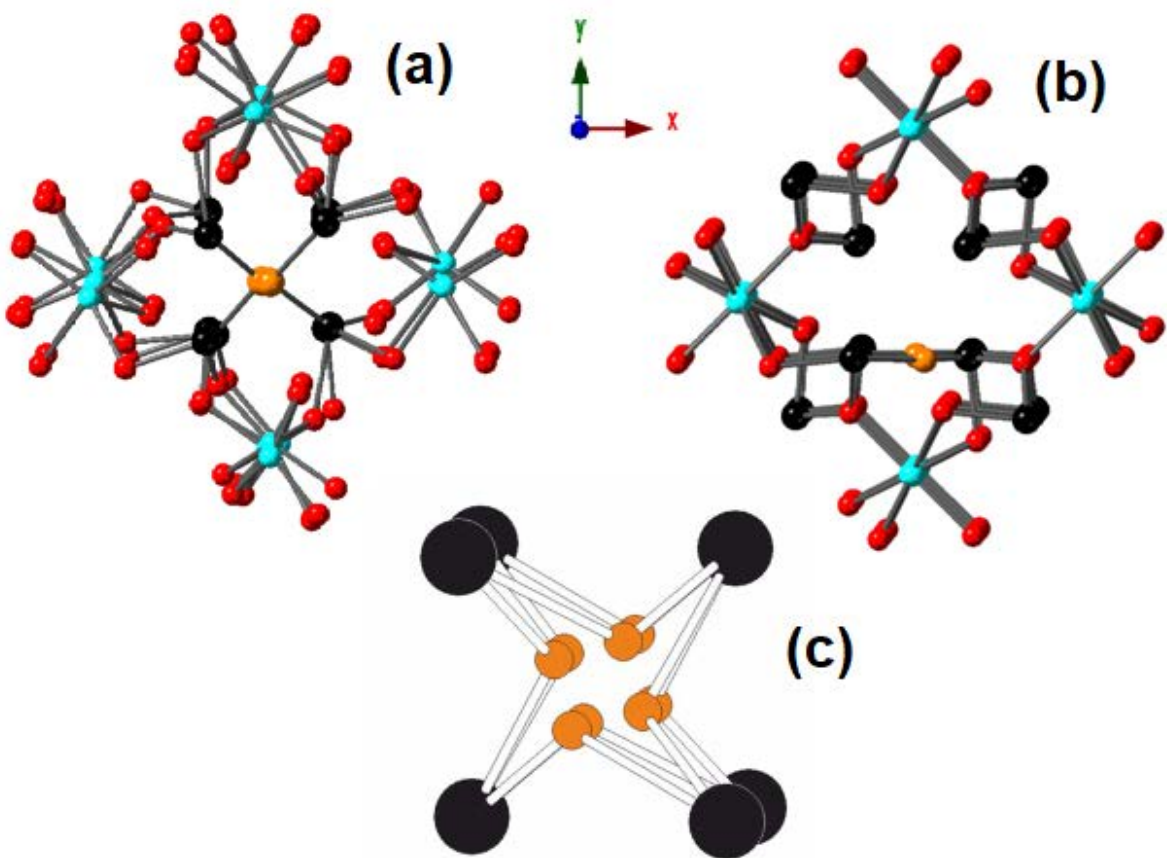


Figure 4.6 (a) and (b) An illustration of the spatial arrangement of ions around the F^- interstitial after geometry optimisation and before optimisation, respectively. Viewed along [110]; (c) proposed $\text{Sb}-\text{F}$ arrangement⁵¹

From the *figure4.6 (a)* it became clear that the fluorine interstitials had moved towards the centre of the channel, bonding with a different set of Sb^{3+} ions along xy -plane. This was also demonstrated experimentally, as seen in *figure4.6c*; the predicted F^- interstitials were found to be closer to the oxygen interstitial sites, as was observed experimentally. However, the bonding preferences of fluorine interstitials were different from those of oxygen. Ions around one of the fluorine interstitials were isolated to study the localised structure around the fluorine ions and the bonding preference of $\text{Sb}-\text{F}$. This structure was then compared with the experimentally proposed structure.

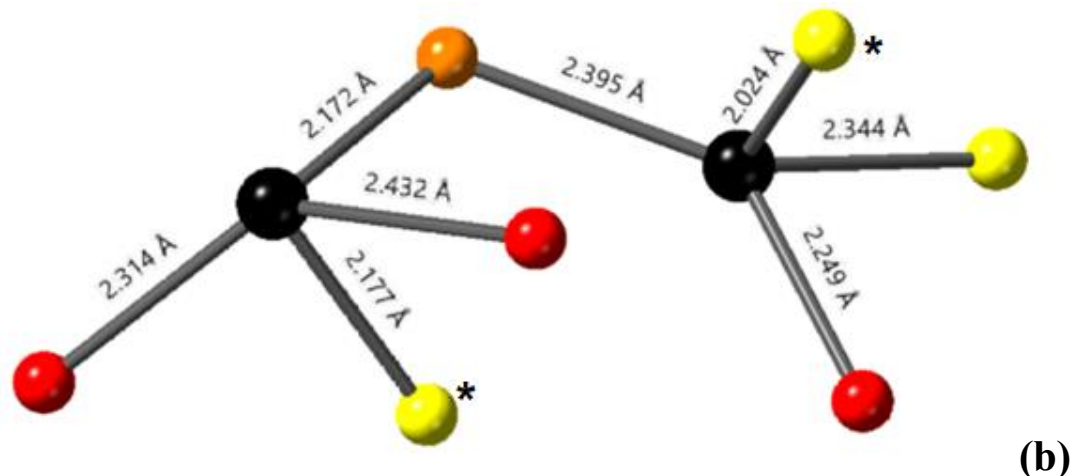
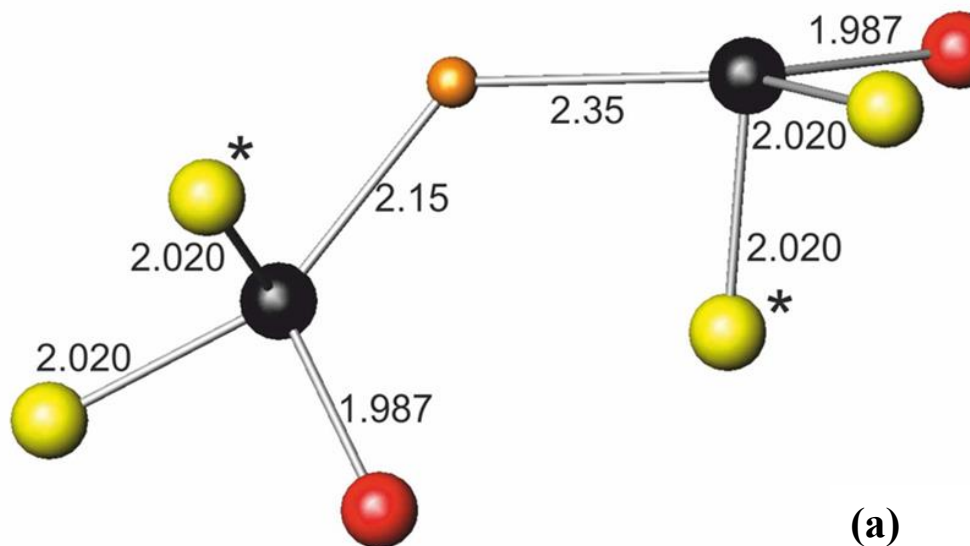


Figure 4.7 (a) Representation of the proposed structure around F^- (orange sphere) interstitial⁵¹; **(b)** representation of the predicted structure of the spatial arrangement of Sb^{3+} (black spheres) and O^{2-} (yellow spheres- apical Oxygen, red spheres- equatorial O) around the F^- interstitial. , Both the structures are viewed roughly along [111]. The average Sb- bond distances are labelled in (a), individual bond distances are labelled (b). Electron lone pairs are opposite the oxygen ions that are marked with a*.

4.5.3 Discussion

From *figure 4.7 (b)*, it can be observed that the predicted localised structure with fluorine interstitials is very similar to the proposed structure. As expected, the predicted bond-distances are different from the experimentally observed ones. Both Sb^{3+} ions bonded to the fluorine interstitials are 4-coordinate. The ions are arranged in such a way the lone pair of electrons are directed into the channel. In *figure 4.7 (b)*, the electron lone pairs are situated opposite to the oxygen ions marked with a^* . The $\text{Sb}-\text{F}$ bond distance was experimentally determined to be same for both the Sb^{3+} ions bonded to the interstitial F^- ions. However, as illustrated in *figure 4.7b*, the calculated bond distances between the fluorine ion and antimony ions are different for each $\text{Sb}-\text{F}$ bond. The other difference between the computationally predicted and experimentally proposed structure is that one of the Sb^{3+} ions is bonded to two O₂ (equatorial) instead of two O₁ (apical). This could be due to the perturbations around the fluorine interstitials. The detailed comparison between proposed and predicted bond-distances is summarised in *table 4.18*.

As summarised in *table 4.18*, some of the predicted $\text{Sb}-\text{O}$ bond-distances are substantially larger than the proposed values. This could a result of the distortion arising from the repulsion between the lone pairs and the two fluorine interstitials. Moreover, the bond with the largest discrepancy Sb2-O₂ (0.41 Å) is within the limit of maximum recorded bond distance (2.596 Å) for a 4 coordinate Sb^{4+} bonded to oxygen ions.¹²⁷ It is also worth noting that the proposed bond-distances are average values calculated for all the ions in the system and the predicted values are individual values for each ion around the fluorine interstitials.

Several attempts were also made to replace O₁ and O₂ (apical and equatorial oxygen) by fluorine in the lattice, each attempt failed to converge and very high lattice energies. This indicates that the inserted fluorine ions occupy various positions in the channel and no F/O exchange occurs.

Thus, it can be concluded that the fluorine interstitials inserted in Schafarzikite occupy sites

towards the centre the one-dimensional channels. They form bridge-like bonds between two antimony ions, such that the lone pairs point into the channel.

Table 4.18 Summary of the predicted Sb-O and Sb-F bond distances

Bonds	<i>Bond Distances (Å)</i>		<i>Difference (Å)</i>
	<i>Calculated</i>	<i>Experimental</i>	
<i>Sb1-O1 [×2]</i>	2.024, 2.344	1.987	0.04, 0.36
<i>Sb1-O2</i>	2.249	2.020	0.23
<i>Sb1-F</i>	2.395	2.35	0.05
<i>Sb2-O1</i>	2.177	1.987	0.19
<i>Sb2-O2 [×2]</i>	2.314, 2.432	2.020	0.24, 0.41
<i>Sb2-F</i>	2.172	2.15	0.02
<i>F-F</i>	2.954	N/A	N/A

4.6 Summary

This chapter demonstrates that the defect behaviour, both intrinsic and extrinsic and the effect of anion insertion in Schafarzikite/FeSb₂O₄ can be investigated by the application of advanced computer simulation techniques. The key features of this chapter are summarised below.

- The pairwise potentials derived in Chapter 3, were employed to study the defect behaviour within FeSb₂O₄. The formation energies of simple point defects including vacancies, interstitial, Schottky and Frenkel defects were calculated. It was observed that oxygen Frenkel pairs were the most favourable type of defects, owing to low defect formation energy and binding energy.
- The effect of aliovalent and isovalent doping on sites M and X (Fe and Sb, respectively) were also investigated and it was concluded Mg²⁺ cation is most energetically favourable dopant on Fe site. The substitution of Pb²⁺ on Sb³⁺site was through the oxidation of Fe²⁺ to Fe³⁺ions was found to be energetically favourable over the formation of oxygen vacancies to charge compensate.
- The effect and the mechanism for anion insertion in the one-dimensional channels of FeSb₂O₄ were studied in detail. This study was used as a means to gain a deeper understanding of the coordination environment and the spatial orientation of the ions around the oxygen and fluorine interstitials. For oxygen excess phases, it was found that the extra oxygen intake was charge compensated by the simultaneous oxidation of Fe²⁺ to Fe³⁺ ions and Sb³⁺ to Sb⁵⁺ ions. It was also found that the stability of the oxygen interstitials in the channels was enhanced by the formation of a defect cluster. This defect cluster was predicted to comprise of three 4-coordinate Sb³⁺ ions, two O²⁻ interstitials and one 6-coordinated Sb⁵⁺.
- The effect fluorine insertion was investigated in a similar manner and it was observed that extra fluorine intake was charge compensated by the oxidation of Fe²⁺ to Fe³⁺. The fluorine ions were observed to move towards the centre of the channel forming bridge-like bonds with two 4-

coordinate Sb^{3+} ions. It was also observed that the O/F exchange was not favourable and the fluorine interstitials occupy sites within the channel.

- The detailed bond lengths and the predicted atomic positions of both the oxygen and fluorine interstitials and neighbouring antimony ions were also presented.
- Energetically, it was observed that the oxygen insertion reaction (-178.23 eV) was more favourable than the fluorine insertion reaction (-174.01 eV).

4.7 Future Work

Future work that could be undertaken within this chapter includes the study of the possibility of ion migration within the channel and in-between the one-dimensional channels. The effect of dopant substitution on the Sb site by a non-toxic cation such as Sn and the related charge compensation mechanisms and its effect on the structure and conductivity could be investigated. The derived potentials were used to perform preliminary equilibration calculation on pure FeSb_2O_4 at 298 K and the resulting structure was able to converge over time. Thus, molecular dynamics could also be used to carry out these calculations and the corresponding Radial Distribution functions (RDF) and Mean square displacement (MSD) could be investigated.

Molecular Dynamics could also be used to calculate the diffusion coefficient of the excess oxygen and fluorine in Schafarzikite/ FeSb_2O_4 . The effect of temperature on the diffusion coefficient could also be calculated. The system could be doped by Pb^{2+} at Sb site, followed by the oxidation of Fe^{2+} to Fe^{3+} ; and the effect of this substitution on the diffusion coefficient could be studied.

Chapter 5: Defect Chemistry and Sodium

Substitution on $\text{Ca}_5\text{Ir}_3\text{O}_{12}$

5.1 Introduction

IrO_2 is best known for its use as one of the most active OER catalysts. It is a $5d$ transition metal oxide, which has rutile like structure, consisting of corner shared IrO_6 octahedra, cross-linked together. It has been well researched and continues to draw attention due to its unrivalled application as an OER catalyst, high stability and its unique magnetic and electric properties.^{12,73,74,82,84} Due to these features, ternary oxides of Iridium have also been an ongoing area of research.

$\text{Ca}_5\text{Ir}_3\text{O}_{12}$ is once such ternary oxide; it adopts a hexagonal geometry and has one-dimensional chains edge shared IrO_6 , similar to those found in IrO_2 . It has a second cation site other than the Ir cation site, occupied by Ca^{2+} ions, which allows the oxidation state of iridium ions to be controlled through substitutions on the calcium site. This unique structural property makes possible, the study of the effect of iridium's oxidation state on the electrocatalytic properties. Reports of dopant substitutions in similar compounds have demonstrated a change in the oxidation state of Iridium ions; e.g., the substitution of a lanthanide and sodium cation for an alkaline earth metal cation in $\text{Ln}_{1-x}\text{Na}_{1+x}\text{IrO}_4$ (where, $\text{Ln} = \text{Gd} - \text{Er}, \text{Y}; x = 0.04\text{e}0.25$), results in an increase in the oxidation state iridium ions from +4.08 to +4.50¹²⁸. However, to the best of our knowledge, studies to investigate the effect of dopant substitutions on the Ca site in $\text{Ca}_5\text{Ir}_3\text{O}_{12}$, have not been reported.

A few attempts have been made to insert the Na ion on the Ca site in the system. The resulting single phase materials have been observed to have different unit cell sizes as compared with the parent phase.⁸³ As Ca occupies two distinct seven coordinate and nine coordinate sites in the lattice, hence it is difficult to determine the Ca site, to which the inserted Na goes. *Figure 5.1* illustrates the crystallographic representation of $\text{Ca}_5\text{Ir}_3\text{O}_{12}$, highlighting the two calcium sites by blue and green coloured spheres.

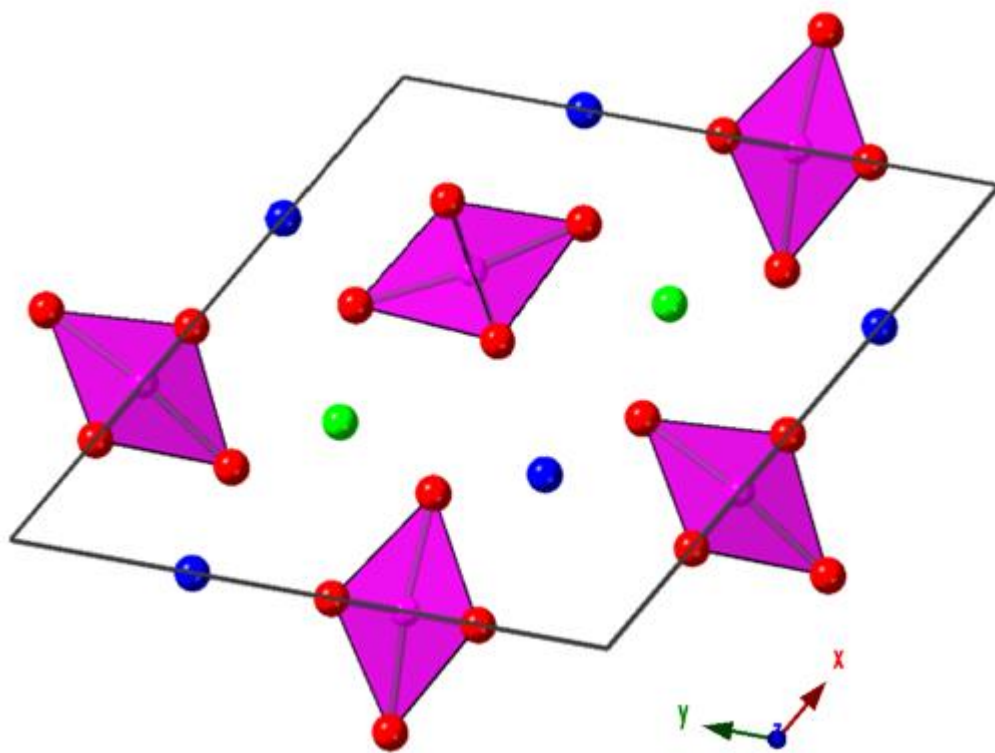


Figure 5.1 An illustration of the predicted unit cell of $\text{Ca}_5\text{Ir}_3\text{O}_{12}$, viewed along [110]; IrO_6 is represented by pink octahedral, $\text{Ca}1$ site is represented by green spheres, $\text{Ca}2$ site is represented by blue spheres and O ions are represented by red spheres.

Hence, in this study, atomistic simulation techniques were used to study the energetics of the substitution of Na ions onto Ca site and to determine the most favourable site for Na ions. The effect of Na substitution on the lattice was also studied and the possibility of a sodium excess phase was also investigated. The techniques were also employed to study the defect chemistry of this compound and to determine the common type of intrinsic defects that would be found in the system. This study is a preliminary to provide data for further investigation of the link between the oxidation state of iridium ions and the system's conduction and electrocatalytic properties.

This chapter will first discuss the defect chemistry of the system by studying the simple point defect, as well as complex defect clusters. Then the energetics of Na substitution will be investigated

to determine the preferable site Ca site. Finally, the energetics and structural changes associated with the amount of sodium inserted will be investigated.

5.2 Intrinsic Defects

The pairwise potentials derived to fit $\text{Ca}_5\text{Ir}_3\text{O}_{12}$ (listed in *table 5.1*), were used to perform a series of defect calculation. Isolated point defects were the first kind of intrinsic defects to be simulated. The results of the initial calculations of isolated vacancies and interstitials are summarised in *table 5.2*.

Equation 5.1 Summary of the short-range parameters derived for $\text{Ca}_5\text{Ir}_3\text{O}_{12}$

<i>Short Range Parameters</i>				<i>Shell Model</i>		
<i>Interaction</i>	<i>A(eV)</i>	<i>ρ (\AA)</i>	<i>C (eV/\AA^6)</i>	<i>Y(e)</i>	<i>k (eV/\AA^2)</i>	<i>Ref.</i>
$\text{Ca}^+ \cdots \text{O}^{2-}$	2272.74	0.2986	0.0	1.281	34.05	109
$\text{Na}^+ \cdots \text{Na}^+$	10209	0.2539	0.00	1.00	<i>Rigid ion</i>	<i>Fitted</i>
$\text{Na}^+ \cdots \text{O}^{2-}$	387.0	0.328409	0.00	1.00	<i>Rigid ion</i>	<i>Fitted</i>
$\text{Ir}^{5+} \cdots \text{O}^{2-}$	5649	0.2648	0.00	0.343	446.3	<i>Fitted</i>
$\text{O}^{2-} \cdots \text{O}^{2-}$	9547.960	0.2192	32.0	-2.04	6.3	129

Table 5.2 Summary of the Isolated Point defects and their energies

Defect	Position	Defect Energy (eV)
Ca1 vacancy $V_{\text{Ca}1}''$	$0.3333, 0.6667, 0.5$	24.31
Ca2 vacancy $V_{\text{Ca}2}''$	$0.69701, 0.0, 0.5$	24.52
Ir vacancy $V_{\text{Ir}}^{4.67'}$	$0.33898, 0.0, 0.0$	128.33
O1 vacancy $V_{\text{O}1}^{\bullet\bullet}$	$0.2163, 0.0, 0.5$	24.34
O2 vacancy $V_{\text{O}2}^{\bullet\bullet}$	$0.4591, 0.0, 0.5$	24.33
O3 vacancy $V_{\text{O}3}^{\bullet\bullet}$	$0.4411, 0.22805, 0.0$	24.17
Ca interstitial $\text{Ca}_i^{\bullet\bullet}$	$0.132, 0.219, 0.711$	-19.19
Ir interstitial $\text{Ir}_i^{4.67\bullet}$	$0.0, 0.0, 0.0$	-102.38
O interstitial O_i''	$0.130, 0.132, -0.026$	-11.86

Initial calculations suggest that Iridium vacancies are energetically unfavourable defect as it has the highest defect formation energy. Energetically most favourable defects are iridium interstitials as they have the lowest defect formation energy. However, isolated point defects do not occur independently and tend to combine to form Frenkel or Schottky type clusters. The lowest energy point

defects were then combined to calculate the energies of formation of Frenkel and Schottky-type defects. A Frenkel defect represents an ion, which has migrated from its initial lattice position to an empty site in the crystal. Similarly, the Schottky defects arise when oppositely charged ions form vacancies in stoichiometric units and maintain the charge-neutrality of the crystal. In the case of $Ca_5Ir_3O_{12}$, apart from the trio, the formation of another Schottky-like defect, CaO could also be possible. The formation energies of both the Frenkel and Schottky defects can be represented by the following (*equations 5.1-5.6*), using the Kröger-Vink notation.¹²⁰ The defect energies calculated by this method is summarised in *table 5.3*

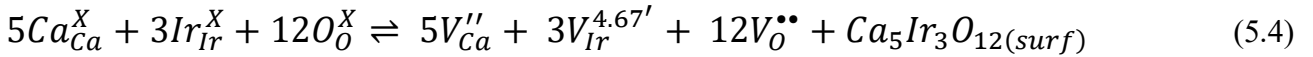


Table 5.3 Summary of Unbound Defect Clusters

Defect	Cluster Formation energy (eV)	Energy per defect (eV)
CaFP	5.12	2.56
IrFP	25.95	12.98
OFP	12.31	6.16
Schottky-Trio	133.15	6.66
Cao- Schottky	10.71	5.36

The defect energy values from *table 5.3*, suggest that calcium Frenkel pairs are the most favourable type of defect clusters, followed by the Cao Schottky and oxygen Frenkel pairs. The Iridium Frenkel pairs are the least favourable type of defect cluster as the formation energy associated with them is very high. These defect energies are calculated assuming infinite dilution (unbound defects) and do not take into account, the relative atomic positions and distances between the defects in a cluster. Thus, bound defect clusters were simulated next. Different configurations of bound Frenkel Pairs clusters were created by placing the Ca, Ir and O ions at various interstitial sites, keeping the vacancy sites constant. For CaO Schottky-like defects, group of Ca and O vacancies were created at different lattice positions. The binding energy associated with these clusters was also calculated by taking the difference between the defect energy of unbound and bound defects. The results for these bound defect clusters are summarised in *Table 5.4.* and *5.5.*

Table 5.4 Energies of Bound Defect Clusters-Frenkel Pairs

Defect	Vacancy Position	Interstitial Position	Formation Energy (eV per defect)	Binding Energy (eV per defect)
<i>CaFP1</i>	<i>0.3333, 0.6667, 0.5</i>	<i>0.0, 0.0, 0.0</i>	<i>1.56</i>	<i>1.00</i>
<i>CaFP2</i>	<i>0.3333, 0.6667, 0.5</i>	<i>0.132 0.219 0.711</i>	<i>1.55</i>	<i>1.01</i>
<i>OFP1</i>	<i>0.4411, 0.22805, 0.0</i>	<i>0.130, 0.132, -0.026</i>	<i>-0.57</i>	<i>5.59</i>
<i>OFP2</i>	<i>0.4411, 0.22805, 0.0</i>	<i>0.0, 0.0, 0.0</i>	<i>5.26</i>	<i>0.9</i>

On examining the defect energies in *table 5.4*, it can be observed that the oxygen Frenkel pairs are the most favourable type of bound defects as they have the lowest defect formation energy. Simulation of iridium Frenkel pairs resulted in the ion migrating back to their vacancy position and recombining.

Table 5.5 Energies of Bound Defect Clusters- Schottky Defects

Defect	<i>Ca Vacancy Position</i>	<i>O Vacancy Position</i>	<i>Formation Energy (eV per defect)</i>	<i>Binding Energy (eV per defect)</i>
<i>CaO Sch1</i>	<i>0.333, 0.667, 0.5</i>	<i>0.2223, 0.0, 0.5</i>	<i>4.56</i>	<i>0.79</i>
<i>CaO Sch 2</i>	<i>0.6986, 0.0, 0.5</i>	<i>0.4567, 0.0, 0.5</i>	<i>4.48</i>	<i>0.88</i>

On examining, the defect energies in summarised in *Table 5.4* and *5.5* it can be concluded that the oxygen Frenkel pairs are energetically the most favourable defects followed by the calcium Frenkel pairs. Owing to the large concentration of defects and the very high defect formation energy associated with the Schottky trio, this cluster was not simulated as a bound defect cluster. Thus it can be concluded that at any given temperature, the equilibrium defect concentration will primarily consist of oxygen Frenkel pairs.

5.3 Sodium Substitution

As outlined in section 5.1, few attempts were made to synthesize a single phase material with some Na inserted on the Ca sites. The unit cell sizes obtained for this new material, $\text{Ca}_4\text{NaIr}_3\text{O}_{12}$, were different from that of the parent phase, signifying that sodium had successfully been incorporated in the system. Since Ca^{2+} occupies two distinct sites in $\text{Ca}_5\text{Ir}_3\text{O}_{12}$, experimentally it was difficult to determine which of the two sites was preferred by Na^+ ions. Thus, computer simulation techniques were employed to determine the energetically favourable site for Na ions. The structural changes, presence of a Na/Ca ordering and the energetics of inserting excess sodium in $\text{Ca}_{5-x}\text{Na}_x\text{Ir}_3\text{O}_{12}$ was also investigated.

5.3.1 Simulating sodium insertion in $\text{Ca}_5\text{Ir}_3\text{O}_{12}$ to form $\text{Ca}_4\text{NaIr}_3\text{O}_{12}$

To determine the preferred Ca site for Na dopant in $\text{Ca}_4\text{NaIr}_3\text{O}_{12}$, the energetics for substituting sodium at both sites were calculated using the first the mean field approach and then the Mott-Littleton approach for modelling crystal defects. By symmetry, there are two sites for Ca1 ion (site1) and three sites for Ca2 ion (site2). To determine if sodium ions have a preferred calcium site, or whether they are distributed at both sites, the lattice energy of $\text{Ca}_{1+x}\text{Na}_{1-x}\text{Ca}_{2y}\text{Na}_{1-y}\text{Ir}_3\text{O}_{12}$ (where $2x+3y=4$) was calculated by varying x between 0.5 and 1.0. Here, x=1.0 refers to both site1 being occupied by Ca1 ions and x=0.5, refers to Na ion occupying one of the two Ca1 sites). Similarly, y was varied between 0.667 and 1.0; here y=1.0 refers to all three site2 being occupied by Ca2 and y=0.7, refers to Na ion

occupying one of the three Ca2 sites. *Table 5.6* summarises the lattice energies of Na ion on each calcium site.

Table 5.6 Summary of the Lattice energy and Sodium Content at Ca1 site and Ca2 site

Na at Site1 and Site	Na/Ca amount	Lattice Energy (eV)
Na at Ca1	<i>Na1=0.5, Ca1=0.5</i>	-699.16
	<i>Na2=0.0, Ca2=1.0</i>	
Na at Ca2	<i>Na2=1/3, Ca2=2/3</i>	-698.91
	<i>Na1=0.0, Ca1=1</i>	

From *table 5.6*, it could be observed that the energy difference between the two Ca sites is not significant. Relying solely on the lattice energy of the two arrangement of Na and Ca ions, it can be observed that the Ca1 site is energetically preferred by inserted Na ions. *Figure 5.2*, illustrates the change in lattice energy of $\text{Ca}_4\text{NaIr}_3\text{O}_{12}$ as a function of the amount of Na ions at both Ca sites.

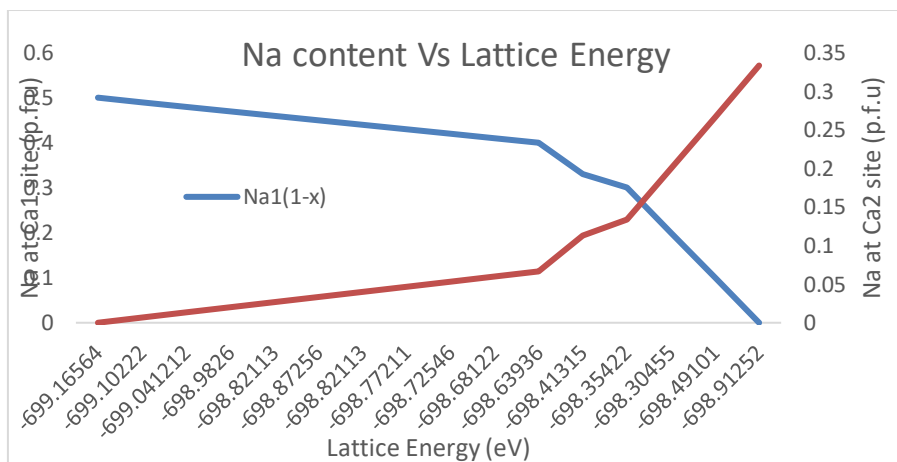


Figure 5.2 Lattice energy of $\text{Ca}_4\text{NaIr}_3\text{O}_{12}$ plotted as a function of Na content at Ca1 and Ca2 site

From examining *figure 5.2*, it can be observed, that the mean energy of Na at Ca1 site is -0.1 eV less than that of Ca2 site. The mean field approach works by the creation of pseudo ions which have a percentage character of both Na and Ca ions for this particular system. Hence, this method alone cannot be used to determine the thermodynamically preferred site for Na ions. Additionally, owing to the small energy difference between the two configurations, the Mott-Little approach for calculating the substitutional and solution energy for the substitution of Na ions onto Ca sites was employed to determine the preferred Ca site for Na.

The substitution of Na onto Ca sites results in the oxidation of iridium from +4.67 to +5. The charge neutrality for this reaction is maintained by the creation of a hole. The mechanism and the solution energy for this reaction can be calculated by using equation 5.7 and 5.8.



$$E_{sol} = -E_{latt}(Na_2O) + \frac{1}{2}E_{sub}(Na_{Ca}) + h + E_{latt}(CaO) \quad (5.8)$$

$$\text{For Na at Ca1} = -(-27.091) + 1/2(15.464) - 37.76 + h = -2.937$$

$$\text{For Na at Ca2} = -(-27.091) + 1/2(6.790) - 37.76 + h = -7.274$$

Since the mechanism for a Na ion onto a Ca site is same for both the calcium sites, hence, the energy associated with the creation of a hole was kept constant in both cases. Moreover, owing to the absence of crystallographic data on any Ir^{4.67} or Ir⁵ oxides, it was not possible to calculate the energy associated with a hole in this instance.

The lattice energy of Na₂O was calculated by using the pairwise potentials derived in this study to reproduce a known structure.¹³⁰ The lattice energy for CaO, was the same as used for Schottky defect calculation. The solution energy for sodium insertion at both the sites Ca1 and Ca2 is summarised in *table 5.7*.

Table 5.7 Substitution of Na on Ca site, solution and substitution energies

Dopant Site	Substitution Energy (eV)	Solution Energy (eV)
Ca1 (0.3333, 0.6667, 0.5)	15.46	-2.94
Ca2 (0.69701, 0.0, 0.5)	6.79	-7.27

There is a significant energy difference between the substitutional and the solution energy for substituting Na ions onto the two Ca sites. From *Table 5.7*, it can be observed that the Ca2 site is energetically more favourable than Ca1 site, as it has lower substitution and solution energy. However, this result is different from that obtained through the mean field approach (summarised in *table 5.6*), which indicated that Ca2 site was more favourable than the Ca1 site. The solution and substitution energies represent the energy required to substitute an actual Ca ion with a Na ion onto the two Ca sites as opposed to the energy of introducing a pseudo ion which had a mixed character of both Na and Ca ions. Therefore, it can be concluded that the Na ion goes to Ca2 site in $\text{Ca}_5\text{Ir}_3\text{O}_{12}$ to form $\text{Ca}_4\text{Na}\text{Ir}_3\text{O}_{12}$. The predicted crystal structure is summarised in *table 5.8*.

The predicted values are slightly different from the experimental values. The lattice parameter c is almost 2% smaller than the overserved value and lattice parameter a and b are approximately 0.4% larger than the predicted. However, the absolute difference between the two structures is -0.08 Å approximately and the RMS percentage error is 2.30 %. Both these values indicate an acceptable fit. It is worth noting, that the experimental values of $\text{Ca}_4\text{Na}\text{Ir}_3\text{O}_{12}$ summarised *table 5.8* are not yet published. For further information regarding the structure, please contact Prof. Colin greaves.⁸³

Table 5.8 Predicted lattice parameters and Ca/Na content at each site for $\text{Ca}_4\text{NaIr}_3\text{O}_{12}$

Lattice Parameters	Experimental Value (\AA)	Predicted Value (\AA)	% Difference
a	9.4620	9.5019	0.42
c	3.1791	3.1071	-2.26
α β γ	90° 90° 120 °	90° 90° 120 °	0
Species	Experimental	Calculated	%Difference
Ca1/Na (1.0/0.0)			
x	0.3333	0.3333	0
y	0.6667	0.6667	0
z	0.5	0.5	0
Ca2/Na (2/3/1/3)			
x	0.7124	0.6867	-3.60
y	0.0	0.0	0
z	0.5	0.5	0
Ir			
x	0.3312	0.3344	0.96
y	0.0	0.0	0
z	0.0	0.0	0
O1			
x	0.201	0.216	7.46
y	0.0	0.0	0
z	0.5	0.5	0
O2			
x	0.462	0.457	-1.08
y	0.0	0.0	0
z	0.5	0.5	0
O3			
x	0.446	0.444	-0.44
y	0.242	0.226	-6.61
z	0.00	0.00	0

5.3.2 Simulating the Na excess phase: $\text{Ca}_3\text{Na}_2\text{Ir}_3\text{O}_{12}$

Following from examining the energetically favourable calcium site for inserted Na ions, attempts were made to simulate a sodium excess phase $\text{Ca}_3\text{Na}_2\text{Ir}_3\text{O}_{12}$, by replacing two calcium ions by two sodium ions. A similar technique (as used in the previous section) was used to determine if there was a favourable site for Na ions or whether they were distributed among the two calcium sites.

It was assumed there is no distribution of Na ions across both the Ca sites. Therefore, both the Na ions could either be at Ca1 site and they could go to Ca2 site. Considering these two cases as the upper limit of the amount of Na each Ca site can have, a series of lattice configurations based on this expression: $\text{Ca}_1x\text{Na}_{1-x}\text{Ca}_2y\text{Na}_{1-y}\text{Ir}_3\text{O}_{12}$ (where $2x+3y=3$), were simulated by varying the amount of Na ions at each site. If all Na goes to Ca2 site, then based on the above expression, the Na/Ca amount on each site will be, $\text{Ca1}=1.0$, $\text{Na}=0.0$; $\text{Ca2}=0.333$ and $\text{Na}=0.667$. Consecutively, if both the Na ions go to Ca1 site, then using the above expression, the Na/Ca amount on each site will be, $\text{Ca1}=0.0$, $\text{Na}=1.0$; $\text{Ca2}=1.0$ and $\text{Na}=0.0$. These two cases represent the upper and lower limit of the amount of Na ions at each calcium site. All the other configurations will lie in between these limits. The lattice energies of each configuration plotted as a function of the amount of sodium on calcium site is illustrated in *Figure 5.3.*

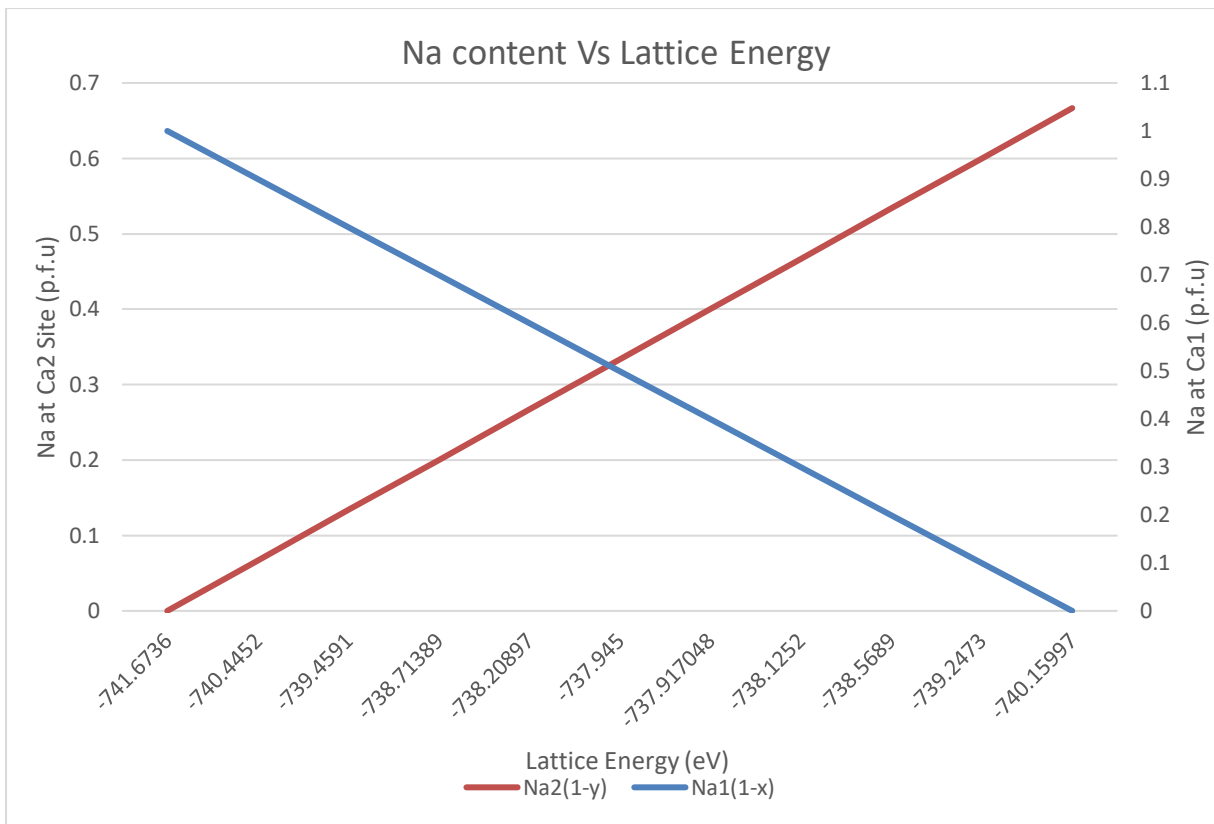


Figure 5.3 Lattice Energy of $\text{Ca}_3\text{Na}_2\text{Ir}_3\text{O}_{12}$ plotted as a function of Na content on Ca1 and Ca2 site

From *figure 5.3*, it can be observed that both Na ions replacing the calcium ions at Ca1 and both the Na ions replacing two calcium ions at Ca2 site correspond to the lowest energy configurations. However, the energy difference between both these cases is only -1.51 eV and hence it is difficult to determine the energetically favourable configuration based on this solely on this data. To overcome this difficulty, the matter was further investigated by employing the supercell approach, wherein a series of different Na/Ca configurations for the $\text{Ca}_3\text{Na}_2\text{Ir}_3\text{O}_{12}$ system were simulated.

A $1 \times 1 \times 1$ supercell of $\text{Ca}_5\text{Ir}_3\text{O}_{12}$ was constructed and Na ions were placed at different Ca sites. Firstly, all the Na ions were placed at Ca1 site and then all the Na ions were placed at Ca2 site. A series of combinations of Na ions distributed across both the Ca sites were also simulated. This approach employed the simulation of actual Na and Ca ions as opposed to the construction of pseudo ions used in the mean field approach. Therefore, this method can be considered a more realistic solution for determining the site preference of Na ions. The results of each simulation are summarised in *table 5.9*.

Figure 5.9 Summary of the Na/Ca distribution and their corresponding energies and the combined percentage error

<i>Na/Ca Arrangement</i>	<i>Na Position</i>	<i>Lattice Energy</i>	<i>Combined Percentage Error</i>
<i>Na1 (1.00), Ca1(0.00)</i>	($\frac{1}{3}$, $\frac{2}{3}$, $\frac{1}{2}$)	-741.67	2.49
	($\frac{2}{3}$, $\frac{1}{3}$, $\frac{1}{2}$)		
<i>Na1 (0.00), Ca1(1.00)</i>	(0.695, 0.00, 0.5)	-742.20	2.62 ³
	(0.00, 0.695, 0.5)		
<i>Na1 (0.50), Ca1(0.50)</i>	($\frac{2}{3}$, $\frac{1}{3}$, $\frac{1}{2}$)	-742.02	4.42 ⁴
	(0.695, 0.00, 0.5)		

From *table 5.9* and *figure 5.3* it can be observed that the Ca2 site is more energetically favourable for the substitution of Na ions. The combined percentage error associated with the observed unit cell also indicates a good agreement with the experimental parameters. The changes in the unit cell parameters as a function of the Na ion content on both the Ca sites were also plotted. This data was then compared with the experimentally determined lattice parameter values. *Figure 5.4*, illustrates the effect that the amount of Na ions at Ca1 site have on lattice parameters *a* and *c*. The plot shows the error on lattice parameters *a* and *c* as a function of the Na ions as they move from Ca2 site to Ca1 site.

³ Three different arrangements of Na2/Ca2 were simulated. Two out of the three also resulted in an orthorhombic unit cell

⁴ The observed unit cell parameters are orthorhombic

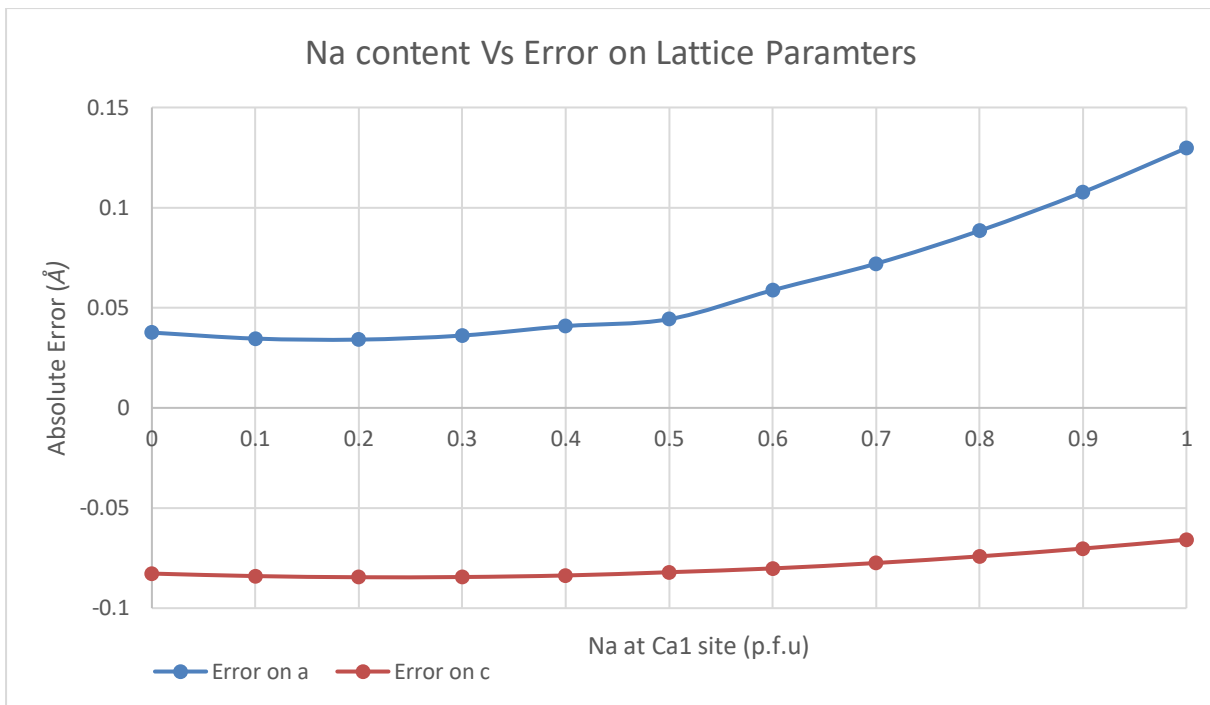


Figure 5.4 Difference between the calculated and observed lattice parameters plotted as a function of Na content on Ca1 site

From the initial calculations using the mean field and supercell method along with the trend observed in *figure 5.4*, it is clear Ca2 site is energetically more favourable for the substitution of the both the Na ions and the discrepancy between the initial and observed structure also increases as the Na ions move from Ca2 site to Ca1 site. Owing to the lack of availability of any other physical properties to compare the calculated structures with, it can be concluded that Ca2 site is the energetically favourable site for the Na ions. The calculated parameters compared with the experimental data is summarised in *table 5.10*.

Table 5.9 Summary of the predicted lattice parameters and atomic positions in $\text{Ca}_3\text{Na}_2\text{Ir}_3\text{O}_{12}$

Lattice Parameters	<i>Experimental Value (Å)</i>	<i>Predicted Value (Å)</i>	<i>% Difference</i>
<i>a</i>	9.4700	9.5787	1.14
<i>c</i>	3.15963	3.0856	-2.34
$\alpha \ \beta \ \gamma$	90° 90° 120 °	90° 90° 120 °	0
Species	<i>Experimental</i>	<i>Calculated</i>	<i>%Difference</i>
Ca1, Na (1.00, 0.00)			
<i>x</i>	0.3333	0.3333	0
<i>y</i>	0.6667	0.6667	0
<i>z</i>	0.5	0.5	0
Ca2, Na (1/3, 2/3)			
<i>x</i>	0.7077	0.6957	-1.69
<i>y</i>	0.0	0.0	0
<i>z</i>	0.5	0.5	0
Ir			
<i>x</i>	0.3303	0.3333	0.90
<i>y</i>	0.0	0.0	0
<i>z</i>	0.0	0.0	0
O1			
<i>x</i>	0.1890	0.2205	1
<i>y</i>	0.0	0.0	0
<i>z</i>	0.5	0.5	0
O2			
<i>x</i>	0.4530	0.4597	1.48
<i>y</i>	0.0	0.0	0
<i>z</i>	0.5	0.5	0
O3			
<i>x</i>	0.4500	0.4600	2.17
<i>y</i>	0.2330	0.2201	-5.53
<i>z</i>	0.00	0.00	0.00

The predicted crystal structure has good agreement with the experimental values. Some of the fractional coordinates have a large discrepancy but the overall difference between the predicted and observed crystal structure is small (0.090\AA). The crystal structure of $\text{Ca}_3\text{Na}_2\text{Ir}_3\text{O}_{12}$ was experimentally determined by Prof. Colin Greaves and these values have not been published yet.⁸³

5.4 Summary

This chapter has illustrated the use of simulation techniques to determine the defect chemistry and predict the energetics of the sodium insertion reaction in the $\text{Ca}_5\text{Ir}_3\text{O}_{12}$. The main features of this chapter are summarised below.

- Intrinsic defect calculations were first performed on the isolated vacancy and interstitial point defects and then on Schottky and Frenkel clusters. For unbound defects, the calculations predict that calcium Frenkel pair has the lowest formation energy of 2.56 eV and is thus, energetically most favourable. For bound defects, the cluster calculations show that the formation energy of the calcium Frenkel, one of the oxygen Frenkel and the CaO Schottky defects had reduced by approximately 1 eV. However, the formation energy of one of the oxygen Frenkel had dropped to -0.57 eV, predicting that at any given temperature, the equilibrium concentration of defects will consist of a large amount of oxygen Frenkel pairs in addition to calcium Frenkel pairs.
- The energetics of Na substitution reaction in $\text{Ca}_5\text{Ir}_3\text{O}_{12}$ to form $\text{Ca}_3\text{Na}_2\text{Ir}_3\text{O}_{12}$ and $\text{Ca}_4\text{Na}\text{Ir}_3\text{O}_{12}$, predict that the $\text{Ca}2$ site is energetically more favourable. This conclusion was drawn based on the low lattice energy values obtained from the mean field approach, the substitutional and solution energy and the supercell approach.
- The simulations using the mean field approach suggest that the lattice parameters a and b increase from 9.469 \AA to 9.578 \AA as the amount of sodium in the system increases from 0 in $\text{Ca}_5\text{Ir}_3\text{O}_{12}$ to 2 in $\text{Ca}_3\text{Na}_2\text{Ir}_3\text{O}_{12}$, while the lattice parameter c decreases from 3.147 \AA to 3.085 \AA .

Å. The increase in lattice parameters a and b is attributed to the increased inter-ionic repulsion between the iridium ions as they get oxidised from +4.67 to +5.33 as the amount of sodium in the system increases from 0 to 2. The lattice parameter c decreases because of the size of the IrO_6 octahedra along the c -axis decreases.

5.5 Future Work

Further work that could be undertaken within this chapter would include investigating the dopant substitution chemistry in $\text{Ca}_5\text{Ir}_3\text{O}_{12}$. Isovalent substitution of Ca^{2+} with Sr^{2+} , aliovalent substitutions with Bi^{3+} and La^{3+} and aliovalent substitution of $\text{Ir}^{4.67+}$ with Ru^{4+} and Ru^{5+} could be studied. These calculations could be used to predict the most favourable dopant for both Ca and Ir sites and the effect of carriers like holes and electrons in case of Na^+ , Bi^{3+} and La^{3+} doping could be studied in detail.

Molecular Dynamics could also be used to investigate the transformation of the crystal structure with Na ions in $\text{Ca}_5\text{Ir}_3\text{O}_{12}$ at different temperatures.

Chapter 6: Conclusion

6.1 General Remarks

In broad terms, the research presented in this thesis has demonstrated how atomistic simulation techniques can be used to study the structural and defect properties of FeSb_2O_4 and $\text{Ca}_5\text{Ir}_3\text{O}_{12}$. As outlined initially in Chapter 1 and later in Chapter 4 and 5, these complex oxide materials have unique structures consisting of chains of linked octahedra, similar to those found in rutile materials. Besides, the presence two distinct cation sites, a feature which is absent in rutile materials, provides a route to control the electronic state of the cations within the chains of linked octahedra. These structural properties make them relevant to the search for new catalyst and electrocatalyst materials. To conclude, the key features of the work undertaken, and the key findings of this study are summarised below.

6.2 Derivation of interatomic potentials

Within this work, the empirical fitting method was used to derive novel pair potentials for FeSb_2O_4 and $\text{Ca}_5\text{Ir}_3\text{O}_{12}$. The potential parameters were varied until a good agreement between the available experimental data and predicted data was achieved. The available experimental data included the lattice parameters, the atomic positions and the inter-ionic bond distances. Due to a lack of availability of other physical properties such as the elastic and dielectric constants, the derived potentials were validated by their ability to work with defected systems and their degree of transferability across several related phases. This process was carried out writing a novel python code.

For FeSb_2O_4 , the effect of the lone pair of electrons present on Sb^{3+} ions was described by using a core and shell model and by introducing an additional, repulsive $\text{Sb}^{3+}\text{-Sb}^{3+}$ pair potential. This methodology was first tested on a binary oxide of antimony, Sb_2O_3 . The method was successful in deriving a set of pair potentials for both these compounds. A good agreement was achieved between observed and predicted structural properties. These potentials were used in Chapter 4 to perform a series of defect calculations and anion insertion calculations in FeSb_2O_4 . The potentials for $\text{Ca}_5\text{Ir}_3\text{O}_{12}$ were also derived similarly. Potential parameters to describe the Ir-O interaction were first derived to

fit the NaIrO_3 structure. The final set of pair potentials were successful in achieving a good agreement with the observed structures of both NaIrO_3 and $\text{Ca}_5\text{Ir}_3\text{O}_{12}$. These potentials were used in Chapter 5 to investigate the defect chemistry and energetics of cation insertion in $\text{Ca}_5\text{Ir}_3\text{O}_{12}$.

The pair potential values derived for both the compounds and series of other compounds relevant to this study: Pb_3O_4 , SbF_3 , Sb_2O_3 and NaIrO_3 have proven to be substantial in modelling both materials in a series of pure and defected form simulations and hence be used for further work with confidence.

6.3 FeSb_2O_4

The potentials derived in Chapter 3 were employed to perform a series of intrinsic and extrinsic defect calculations on FeSb_2O_4 . The initial calculation was performed on isolated vacancies and interstitials. The energies of these isolated point defects were combined to calculate the formation energy of defect clusters like Frenkel and Schottky. These energies were then compared with the formation energies of bound defect clusters. Intrinsic defect calculations predict, that oxygen Frenkel pairs are energetically most favourable and would dominate the equilibrium defect concentration at any given temperature.

A series of dopant substitution calculations were also performed on both Fe (site M) and Sb (site X) cation sites. For site M, the calculations predict the Mg^{2+} is energetically the most favourable dopant. For transition metal dopants, it was observed that the solution energy and the substitution energy of the system increased with the increase in the atomic radius of the transition metal cations. (Mn , Co , Ni) For site X, Pb^{2+} was predicted to be the most favourable dopant. The energetically preferred reaction mechanism for the substitution of Sb^{3+} by Pb^{2+} was predicted to be through oxidation of Fe^{2+} to Fe^{3+} in the chains of octahedra. These results corroborate with the experimental findings.

In the end, the pair potentials were used to simulate the study the energetics and structural effect of anion insertion in the one-dimensional channels, which are an inherent feature of FeSb_2O_4 .

This was achieved by constructing a supercell and placing the anions in channels. For O²⁻ insertion in the channel, the simulations predict the formation of a defect cluster comprising of three 4-coordinate Sb³⁺ ions, two O²⁻ interstitial ions and one 6-coordinate Sb⁵⁺ion. The relevant charge compensation mechanism as predicted by the experimental data was found to energetically favourable. The predicted defect cluster gives a clear picture of the localised environment around the O²⁻ interstitials. A similar approach was used to simulate the insertion of F⁻ ions in the channel. It was observed that the bonding preferences of fluorine were different from that of oxygen ions. The calculations predict that the F⁻ interstitials move towards the centre of the channels and form bridge-like Sb-F bonds of unequal length with the nearest Sb³⁺ ions in the channel walls. Through these simulations, it was possible to obtain individual Sb-O and Sb-F bond distances and lattice parameters for the oxygen excess and fluorine excess phases.

6.4 Ca₅Ir₃O₁₂

In Chapter 5, the pair potentials derived in Chapter 3 were used to perform several intrinsic defect calculations. Initial calculations were performed on isolated point defects. The lowest defect energy of each ion's vacancy and interstitial were combined to calculate the formation energies of defect clusters. These energies were calculated for unbound defects and bound defect clusters. For unbound defects, it is predicted that calcium Frenkel pairs would be energetically most favourable and hence the preferred mode of intrinsic disorder. For bound defects, it was observed that the oxygen Frenkel pairs had the lowest defect formation energy and hence it was concluded that equilibrium defect concentration will consist of both oxygen and calcium Frenkel pairs.

For Na incorporation in Ca₅Ir₃O₁₂, the energetically favourable Ca site for inserted Na ions were determined by calculating the substitution and solution energy of this reaction, as well as the mean field. From the simulation methods, it is predicted that the energetically favourable site for Na ion is Ca2 site, and the Na/Ca amount at each calcium site is: for site Ca site 2, Ca=1/3, Na=2/3; for Ca site

1, Ca=1, Na=0. The predicted crystal structure of the sodium-inserted phase, $\text{Ca}_4\text{NaIr}_3\text{O}_{12}$, is in a fairly good agreement with the experimental structure. The energetics of the sodium excess phase $\text{Ca}_3\text{Na}_2\text{Ir}_3\text{O}_{12}$ was also investigated in a similar manner. The results obtained from the simulations predict that both inserted Na ions will migrate to Ca site2 as it is energetically favourable, and it also has less discrepancy as compared with the experimental data.

Reference

- 1 A. von Hippel, R. G. Breckenridge, F. G. Chesley and L. Tisza, *Ind. Eng. Chem.*, 1946, **38**, 1097–1109.
- 2 G. H. Jonker and J. H. Van Santen, *Physica*, 1950, **16**, 337–349.
- 3 M. K. Wu, J. R. Ashburn, C. J. Torng, P. H. Hor, R. L. Meng, L. Gao, Z. J. Huang, Y. Q. Wang and C. W. Chu, *Phys. Rev. Lett.*, 1987, **58**, 908–910.
- 4 B. L. Ellis, K. T. Lee and L. F. Nazar, *Chem. Mater.*, 2010, **22**, 691–714.
- 5 F. J. Morin, *Phys. Rev. Lett.*, 1959, **3**, 34–36.
- 6 K. Ramesh Babu, C. Bheema Lingam, S. Auluck, S. P. Tewari and G. Vaitheswaran, *J. Solid State Chem.*, 2011, **184**, 343–350.
- 7 G. T. Ang, G. H. Toh, M. Z. A. Bakar, A. Z. Abdullah and M. R. Othman, *Process Saf. Environ. Prot.*, 2011, **89**, 186–192.
- 8 R. Bayliss, F. J. Berry, A. Bowden, C. Greaves and M. F. Thomas, in *Journal of Physics: Conference Series*, 2010, p. 012049.
- 9 M. J. Whitaker, R. D. Bayliss, F. J. Berry and C. Greaves, *J. Mater. Chem.*, 2011, **21**, 14523–14529.
- 10 R. D. Bayliss, F. J. Berry, B. P. de Laune, C. Greaves, O. Helgason, J. F. Marco, M. F. Thomas, L. Vergara and M. J. Whitaker, *J. Physics-Condensed Matter*, 2012, **24**, 6001.
- 11 F. J. J. Dijksma, J. F. Vente, E. Frikkee and D. J. W. Ijhdo, *Mat. Res. Bull.*, 1993, **28**, 1145–1151.

- 12 M. Wakeshima, N. Taira, Y. Hinatsu and Y. Ishii, *Solid State Commun.*, 2003, **125**, 311–315.
- 13 C. Pirovano, M. S. Islam, R. N. Vannier, G. Nowogrocki and G. Mairesse, *Solid State Ionics*, 2001, **140**, 115–123.
- 14 A. Snedden, P. Lightfoot, T. Dinges and M. S. Islam, *J. Solid State Chem.*, 2004, **177**, 3660–3665.
- 15 M. S. Islam, S. Lazure, R. N. Vannier, G. Nowogrocki and G. Mairesse, *J. Mater. Chem.*, 1998, **8**, 655–660.
- 16 J. R. Gavarri, J. P. Vigouroux, G. Calvarin and A. W. Hewat, *J. Solid State Chem.*, 1981, **36**, 81–90.
- 17 J. A. Krenner, *Kristallogr.*, 1921, **56**, 198.
- 18 J.-R. Gavarri and D. Weigel, *J. Solid State Chem.*, 1975, **13**, 252–257.
- 19 S. Bahfenne, L. Rintoul and R. L. Frost, *Am. Mineral.*, 2011, **96**, 888–894.
- 20 S. Andersson and A. Åström, *Natl. Bur. Stand. Spec. Publ. 364, Solid State Chem. Proc. 5th Mater. Res. Symp.*, 1972.
- 21 M. Retuerto, A. Muñoz, M. J. Martinez-Lope, M. Garcia-Hernandez, G. André, K. Krezhov and J. A. Alonso, *J. Phys. Condens. Matter*, 2013, **25**, 216002.
- 22 A. C. Stowe, S. Nellutla, N. Dalal and U. Kortz, *Eur. J. Inorg. Chem.*, 2004, **2004**, 3792–3797.
- 23 C. Giroux-Maraine and G. Perez, *Rev. Chim. min'erales*, 1975, **12**, 427–432.
- 24 N. Kumada, Y. Yonesaki, T. Takei, N. Kinomura and S. Wada, *Mater. Res. Bull.*, 2009, **44**, 1298–1300.
- 25 H. Fjellvag and A. Kjekshus, *Acta Chem. Scand. Ser. a-Physical Inorg. Chem.*, 1985, **39**, 389–

- 395.
- 26 R. Fischer and F. Pertlik, *Tschermaks Mineral. und Petrogr. Mitteilungen*, 1975, **22**, 236–241.
- 27 P. Norby, M. Roelsgaard, M. Sondergaard and B. B. Iversen, *Cryst. Growth Des.*, 2016, **16**, 834–841.
- 28 H. T. Witteveen, *Solid State Commun.*, 1971, **9**, 1313–1315.
- 29 J. R. Gavarri and A. W. Hewat, *J. Solid State Chem.*, 1983, **49**, 14–19.
- 30 F. Pertlik, *Tschermaks Mineral. und Petrogr. Mitteilungen*, 1975, **22**, 211–217.
- 31 Atanasova M. T., Strydom A. M., Schutte C. J. H. and Prinsloo L. C., *J. Mater. Sci.*, 2014, **46**, 3497–3510.
- 32 E. Gutierrez Puebla, E. Gutierrez Rios, A. Monge and I. Rasines, *Acta Crystallogr. Sect. B*, 1982, **38**, 2020–2022.
- 33 N. Bettahar, P. Conflant, F. Abraham and D. Thomas, *J. Solid State Chem.*, 1987, **67**, 85–90.
- 34 M. K. Fayek and J. Leciejewicz, *Zeitschrift Fur Anorg. Und Allg. Chemie*, 1965, **336**, 104–109.
- 35 A. Teichert and H. Müller-Buschbaum, *Zeitschrift Fur Anorg. Und Allg. Chemie*, 1991, **598**, 319–325.
- 36 Ghose S and Sen Gupta P. K, *Am. Mineral.*, 1987, **78**, 629–632.
- 37 A. M. Abakumov, M. G. Rozova, E. V Antipov, J. Hadermann, G. Van Tendeloo, M. V Lobanov, M. Greenblatt, M. Croft, E. V Tsiper, A. Llobet, K. A. Lokshin and Y. S. Zhao, *Chem. Mater.*, 2005, **17**, 1123–1134.
- 38 B. P. de Laune and C. Greaves, *J. Solid State Chem.*, 2012, **187**, 225–230.

- 39 B. P. de Laune, F. J. Berry, J. F. Marco, S. L. Horswell and C. Greaves, *J. Mater. Chem. C*, 2016, **4**, 5320–5325.
- 40 F. J. Berry, B. P. de Laune, C. Greaves, M. J. Whitaker, M. F. Thomas and J. F. Marco, *Hyperfine Interact.*, 2014, **226**, 545–552.
- 41 J. Cumby, B. P. de Laune and C. Greaves, *J. Mater. Chem. C*, 2016, **4**, 201–208.
- 42 F. J. Berry, B. P. De Laune, C. Greaves, H.-Y. Hah, · Charles, E. Johnson, J. A. Johnson, S. Kamali, J. F. Marco, M. F. Thomas and M. J. Whitaker, *Hyperfine Interact.*, 2018, **239**, 1–8.
- 43 B. Y. Brach, N. V Chezhina and Y. V Shapoval, *Inorg. Mater.*, 1989, **25**, 601.
- 44 B. P. De Laune, M. J. Whitaker, J. F. Marco, M. F. Thomas, F. J. Berry, M. R. Lees and C. Greaves, *J. Mater. Chem. C*, 2017, **5**, 4985–4995.
- 45 H. Abe, K. Yoshii and H. Kitazawa, *Phys. Status Solidi a-Applied Res.*, 2002, **189**, 429–432.
- 46 R. D. Shannon, *Acta Crystallogr. Sect. A*, 1976, **32**, 751–767.
- 47 B. P. de Laune, G. J. Rees, M. J. Whitaker, H.-Y. Hah, C. E. Johnson, J. A. Johnson, D. E. Brown, M. G. Tucker, T. C. Hansen, F. J. Berry, J. V Hanna, C. Greaves, D. E. Brown, M. G. Tucker, T. C. Hansen, F. J. Berry, J. V Hanna and C. Greaves, *Inorg. Chem.*, 2017, **56**, 594–607.
- 48 C. Greaves and M. Francesconi, *Curr. Opin. Solid State Mater. Sci.*, 1998, **3**, 132–136.
- 49 M. Pagliaro and R. Ciriminna, *J. Mater. Chem.*, 2005, **15**, 4981–4991.
- 50 B. Chevalier, A. Tressaud, B. Lepine, K. Amine, J. M. Dance, L. Lozano, E. Hickey and J. Etourneau, *Phys. C Supercond. its Appl.*, 1990, **167**, 97–101.
- 51 B. P. de Laune, G. J. Rees, J. F. Marco, H. Y. Hah, C. E. Johnson, J. A. Johnson, F. J. Berry, J.

- V Hanna and C. Greaves, *Inorg. Chem.*, 2017, **56**, 10078–10089.
- 52 K. Caslin, R. K. Kremer, F. S. Razavi, A. Schulz, A. Muñoz, F. Pertlik, J. Liu, M. H. Whangbo and J. M. Law, *Phys. Rev. B - Condens. Matter Mater. Phys.*, 2014, **89**, 1–11.
- 53 B. P. de Laune, PhD Thesis, University of Birmingham, 2013.
- 54 K. Caslin, R. K. Kremer, F. S. Razavi, M. Hanfland, K. Syassen, E. E. Gordon and M. H. Whangbo, *Phys. Rev. B*, 2016, **93**, 22301.
- 55 J. Cumby, PhD Thesis, University of Birmingham, 2014.
- 56 R. Grau-Crespo, C. R. A. Catlow and N. H. de Leeuw, *J. Catal.*, 2007, **248**, 77–88.
- 57 B. G. Dick and J. and A. W. Overhauser, *Phys. Rev.*, 1958, **112**, 90–103.
- 58 D. Lebellac, J. M. Kiat and P. Garnier, *J. Solid State Chem.*, 1995, **114**, 459–468.
- 59 S. Trasatti, *Electrochim. Acta*, 1984, **29**, 1503–1512.
- 60 K. Sardar, S. C. Ball, J. D. B. Sharman, D. Thompsett, J. M. Fisher, R. A. P. Smith, P. K. Biswas, M. R. Lees, R. J. Kashtiban, J. Sloan and R. I. Walton, *Chem. Mater.*, 2012, **24**, 4192–4200.
- 61 M. K. Horng, R. H., Wuu, D. S., Wu, L. H. & Lee, *Thin Solid Films*, 2000, **373**, 231–234.
- 62 R. S. Chen, Y. S. Huang, Y. M. Liang, D. S. Tsai, Y. Chi and J. J. Kai, *J. Mater. Chem.*, 2003, **13**, 2525–2529.
- 63 Y. Lee, J. Suntivich, K. J. May, E. E. Perry and Y. Shao-Horn, *J. Phys. Chem. Lett.*, 2012, **3**, 399–404.
- 64 J. Backhom, PhD Thesis, Uppsala University, 2008.
- 65 A. Kitaev, *Ann. Phys. (N. Y.)*, 2006, **321**, 2–111.

- 66 G. Jackeli and G. Khaliullin, *Phys. Rev. Lett.*, 2009, **102**, 17205.
- 67 J. Chaloupka, G. Jackeli and G. Khaliullin, *Phys. Rev. Lett.*, 2010, **105**, 27204.
- 68 Y. Machida, S. Nakatsuji, Y. Maeno, T. Tayama, T. Sakakibara and S. Onoda, *Phys. Rev. Lett.*, 2007, **98**, 57203.
- 69 K. Matsuhira, M. Wakeshima, R. Nakanishi, T. Yamada, A. Nakamura, W. Kawano, S. Takagi and Y. Hinatsu, *J. Phys. Soc. Japan*, 2007, **76**, 43706.
- 70 K. Tomiyasu, K. Matsuhira, K. Iwasa, M. Watahiki, S. Takagi, M. Wakeshima, Y. Hinatsu, M. Yokoyama, K. Ohoyama and K. Yamada, *J. Phys. Soc. Japan*, 2012, **81**, 34709.
- 71 F. Wang and T. Senthil, *Phys. Rev. Lett.*, 2011, **106**, 136402.
- 72 T. Han, Y. Wang, J. Yang, L. He, J. Xu, D. Liang, H. Han, M. Ge, C. Y. Xi, W. K. Zhu, C. Zhang and Y. Zhang, *Appl. Phys. Lett.*, 2016, **109**, 192409.
- 73 I. Franke, P. J. Baker, S. J. Blundell, T. Lancaster, W. Hayes, F. L. Pratt and G. Cao, *Phys. Rev. B - Condens. Matter Mater. Phys.*, 2011, **83**, 4–8.
- 74 M. M. Sala, K. Ohgushi, A. Al-Zein, Y. Hirata, G. Monaco and M. Krisch, *Phys. Rev. Lett.*, 2014, **112**, 176402.
- 75 W. Hu, H. Zhong, W. Liang and S. Chen, *ACS Appl. Mater. Interfaces*, 2014, **6**, 12729–12736.
- 76 T. Reier, Z. Pawolek, S. Cherevko, M. Bruns, T. Jones, D. Teschner, S. Selve, A. Bergmann, H. N. Nong, R. Schlägl, K. J. J. Mayrhofer and P. Strasser, *J. Am. Chem. Soc.*, 2015, **137**, 13031–13040.
- 77 W. Sun, Y. Song, X.-Q. Gong, L. Cao and J. Yang, *Chem. Sci.*, 2015, **6**, 4993–4999.
- 78 F. I. Mattos-Costa, P. de Lima-Neto, S. A. S. Machado and L. A. Avaca, *Electrochim. Acta*,

- 1998, **44**, 1515–1523.
- 79 A. Marshall, B. Børresen, G. Hagen, M. Tsyplkin and R. Tunold, *Electrochim. Acta*, 2006, **51**, 3161–3167.
- 80 W. Sun, Y. Song, X. Q. Gong, L. M. Cao and J. Yang, *ACS Appl. Mater. Interfaces*, 2016, **8**, 820–826.
- 81 K. Sardar, E. Petrucco, C. I. Hiley, J. D. B. Sharman, P. P. Wells, A. E. Russell, R. J. Kashtiban, J. Sloan and R. I. Walton, *Angew. Chemie - Int. Ed.*, 2014, **53**, 10960–10964.
- 82 G. Cao, V. Durairaj, S. Chikara, S. Parkin and P. Schlottmann, *Phys. Rev. B - Condens. Matter Mater. Phys.*, 2007, **75**, 1–9.
- 83 C. Greaves, *Personal Communication*, .
- 84 X. Chen and S. Wilson, *Phys. Rev. B*, 2016, **94**, 1.
- 85 H. F. Poulsen, S. F. Nielsen, E. M. Lauridsen, S. Schmidt, R. M. Suter, U. Lienert, T. Lorentzen and D. J. Jensen, 2001, 751–756.
- 86 H. C. Zur Loye, R. C. Layland, M. D. Smith and J. B. Claridge, *J. Cryst. Growth*, 2000, **211**, 452–457.
- 87 K. Matsuhira, K. Nakamura, Y. Yasukuni, Y. Yoshimoto, D. Hirai and Z. Hiroi, *J. Phys. Soc. Japan*, 2018, **87**, 1–5.
- 88 J. D. Gale, *J. Chem. Soc., Faraday Trans.*, 1997, **93**, 629–637.
- 89 J. H. Harding, *Reports Prog. Phys.*, 1990, **53**, 1403–1466.
- 90 M. S. D. Read and R. A. Jackson, *J. Nucl. Mater.*, 2010, **406**, 293–303.
- 91 P. Ewald, *Ann. Phys. Leipzig*, 1921, **64**, 253–287.

- 92 P. M. Morse, *Phys. Rev.*, 1929, **34**, 57–64.
- 93 L. Verlet, *Phys. Rev.*, 1967, **159**, 98–103.
- 94 R. A. Buckingham, *Proc. R. Soc. A Math. Phys. Eng. Sci.*, 1938, **168**, 264–283.
- 95 M. Born and J. Mayer, *Zeitschrift für Phys.*, 1932, **75**, 1–18.
- 96 P. Debye, *Math. Ann.*, 1909, **67**, 535.
- 97 W. H. Press, S. A. Teukolsky, W. T. Vetterling and B. P. Flannery, *Numerical recipes in Fortran: The art of scientific computing*, Cambridge University Press, 1986.
- 98 J. F. Nye, *Physical Properties of Crystals*, Oxford University Press, 1957.
- 99 A. B. Lidiard, *J. Chem. Soc. Faraday Trans. 2 Mol. Chem. Phys.*, 1989, **85**, 341–349.
- 100 Q. Lin, X. Feng and Z. Man, *Phys. Rev. B - Condens. Matter Mater. Phys.*, 2001, **63**, 1–6.
- 101 Q. Lin and X. Feng, *J. Phys. Condens. Matter*, 2003, **15**, 1963–1973.
- 102 M. S. Islam, S. Lauzure, R.-N. Vannier, G. Nowogrocki and G. Mairesse, *J. Mater Chem.*, 1998, **8**, 655.
- 103 H. E. Swanson and R. K. Fuyat, *Natl. Bur. Stand. Circ.*, 1953, **539**, 1–65.
- 104 J. M. Moreau, P. Galez, J. P. Peigneux and M. V Korzhik, *J. Alloys Compd.*, 1996, **238**, 46–48.
- 105 C. Svensson, *Acta Crystallogr. Sect. B*, 1974, **30**, 458–461.
- 106 M. J. Buerger and S. B. Hendricks, *Zeitschrift fur Krist.*, 1938, **98**, 1–30.
- 107 C. Svensson, *Acta Crystallogr. Sect. B*, 1975, **31**, 2016–2018.
- 108 G. V Lewis and C. R. A. Catlow, *J.Phys.C Solid State Phys.*, 1985, **18**, 1149–1161.

- 109 T. S. Bush, J. D. Gale, C. R. A. Catlow and P. D. Battle, *J. Mater Chem.*, 1994, **4**, 831–837.
- 110 G. V Lewis and C. R. A. Catlow, *J. Phys. C Solid State Phys.*, 1985, **18**, 1149–1161.
- 111 L. Minervini, R. W. Grimes and K. E. Sickafus, *J. Am. Ceram. Soc.*, 2000, **83**, 1873–1878.
- 112 M. Søndergaard, M. Roelsgaard, B. B. Iversen, P. Nørby and E. Eikeland, *Dalt. Trans.*, 2016, **45**, 18994–19001.
- 113 C. Giroux-Maraine and G. Perez, *Rev. Chim. Miner.*, 1975, **12**, 427–432.
- 114 B. P. de Laune and C. Greaves, *J. Solid State Chem.*, 2012, **187**, 225–230.
- 115 J. Molnár, M. Kolonits and M. Hargittai, *J. Mol. Struct.*, 1997, **413–414**, 441–446.
- 116 D. J. Binks, PhD Thesis, University of Surrey, 1994.
- 117 P. D. Battle, T. S. Bush and C. R. A. Catlow, *J. Am. Chem. Soc.*, 1995, **117**, 6292–6296.
- 118 L. Du, X. Sheng, H. Weng and X. Dai, *Europhys. Lett.*, 2012, **101**, 27003.
- 119 F. J. Berry, B. P. de Laune, C. Greaves, M. J. Whitaker, M. F. Thomas and J. F. Marco, *Hyperfine Interact.*, 2013, **226**, 545–552.
- 120 F. A. Kroger and H. J. Vink, *Solid State Phys.*, 1956, **3**, 307–435.
- 121 J. P. Allen, J. J. Carey, A. Walsh, D. O. Scanlon and G. W. Watson, *J. Phys. Chem. C*, 2013, **117**, 14759–14769.
- 122 R. W. G. Wyckoff and E. D. Crittenden, *Zeitschrift für Krist. - Cryst. Mater.*, 1976, **63**, 144–147.
- 123 M. J. Whitaker, PhD Thesis, University of Birmingham, 2012.
- 124 P. Garnier, J. Moreau and J. R. Gavarri, *Mater. Res. Bull.*, 1990, **25**, 979–986.

- 125 R. L. David, *Handbook of chemistry and Physics*, CRC Press, 74th edn., 1993.
- 126 S. M. Woodley, C. R. A. Catlow, P. Piszora, K. Stempin and E. Wolska, *J. Sol. State Chem.*, 2000, **153**, 1–10.
- 127 O. C. Gagné and F. C. Hawthorne, *Acta Crystallogr. Sect. B Struct. Sci. Cryst. Eng. Mater.*, 2018, **74**, 63–78.
- 128 S. J. Mugavero, M. D. Smith and H. C. zur Loye, *Solid State Sci.*, 2007, **9**, 555–563.
- 129 M. A. McCoy, R. W. Grimes and W. E. Lee, *Philos. Mag. A Phys. Condens. Matter, Struct. Defects Mech. Prop.*, 1997, **75**, 833–846.
- 130 E. Zintl, A. Harder and B. Dauth, *Zeitschrift fuer Elektrochemie und Angew. Phys. Chemie*, 1934, **40**, 588–593.